Transverse Plane Rotational Misalignment of Ankle Arthrodesis and Arthroplasty in Cadaveric Gait Simulation

Brian K. Cook

A thesis

submitted in partial fulfillment of the

requirements for the degree of

Master of Science in Mechanical Engineering

University of Washington

2016

Committee:

William R. Ledoux, Chair

Randall P. Ching

Katherine M. Steele

Program Authorized to Offer Degree:

Department of Mechanical Engineering

University of Washington

Abstract

Transverse Plane Rotational Misalignment of Ankle Arthrodesis and Arthroplasty in Cadaveric Gait Simulation

Brian K. Cook

Chair of the Supervisory Committee:
Affiliate Associate Professor William R. Ledoux
Departments of Mechanical Engineering and Orthopaedics & Sports Medicine

End-stage arthritis of the ankle is a debilitating disease that is commonly treated surgically with arthrodesis and arthroplasty of the ankle joint. Misalignment of the ankle joint occurs in both of these surgeries, and for both procedures, misalignment can negatively impact patient outcomes. The goal of this thesis was to examine misalignment of these procedures in cadaveric gait simulation. Using cadaveric specimens in orthopaedics and biomechanics allows for novel concepts or evaluations of procedures to be performed without the potential harm to a patient. A robotic gait simulator was used to simulate stance phase of gait on cadaveric foot specimens, to examine multiple alignments of ankle arthrodesis and arthroplasty. Ground reaction forces and tibia-to-ground kinematics were replicated by the simulator from patients postoperatively for each surgery.

Ankle arthrodesis was simulated using a custom two-plate fixture that allowed for the ankle to be fused in multiple transverse plane rotational alignments of the surgery. Misalignment of the ankle arthrodesis showed minimal significant changes to joint ranges of motion of the foot, but analysis of joint angles throughout stance phase showed an abnormal position of the naviculocuneiform and cuboid-fifth metatarsal joints due to internal rotational misalignments. No changes were seen in the plantar pressure distribution analysis due to misalignment.

Ankle arthroplasty was simulated using a custom surgical technique and fixture, designed to implant the Salto Talaris total ankle system into cadaveric specimens such that the neutral alignment replicated the in vivo surgery, but transverse plane rotational misalignments could be applied to the arthroplasty. Transverse plane rotational misalignment of the arthroplasty altered joint kinematics of not only the ankle joint, but distal foot joints as well. Plantar pressure distribution was not changed due to arthroplasty misalignment.

These studies quantified the effect of transverse plane rotational misalignment of each surgery on joint kinematics and plantar pressure distribution. The results suggest that arthroplasty misalignment may have a greater effect on foot function than arthrodesis misalignment, but comparisons between the studies are difficult due to the differences in loading conditions between the studies. Analyses of joint stresses would allow for more complete understanding of the biomechanical changes the foot undergoes due to surgical misalignment, and could further the clinical knowledge of joint loading after these procedures.

TABLE OF CONTENTS

LIST OF FIGURES

LIST OF TABLES

ACKNOWLEDGEMENTS

I would first like to thank my advisor William Ledoux, whose constant guidance and expertise allowed me to gain extensive knowledge about engineering, biomechanics, and orthopaedics throughout this thesis project. I would like to also acknowledge Matthew Kindig and Christina Stender for their invaluable assistance and advice throughout the project. Thank you also to my other committee members, Randy Ching and Kat Steele, for their contributions to the project. The collaborations with Dr. Bruce Sangeorzan, Dr. Matt Beuchel, Dr. Garrett Pangrazzi, and Dr. Cam Patthanacharoenphon were vital to the project, and allowed me to gain great insight into the clinical side of orthopaedics, for which I am very grateful. Thanks to Jane Shofer, who provided her expertise on statistical analyses throughout this project. Thank you to Eric Whittaker, whose guidance gave me an excellent foundation in biomechanics research, and whose previous work was instrumental in the success of RGS testing. Finally, thank you to the other graduate students, undergraduate research assistants, and staff at the VA Center for Limb Loss Prevention and Prosthetic Engineering, for their support throughout my entire project.

Further, I would like to thank my parents, and my sister Megan, for their continuous encouragement and support of my education over the years. And finally, thanks to my girlfriend, Nicole, for her incredible support throughout this project.

Thank you to the Department of Veterans Affairs, specifically VA Grant F7968, for funding this research.

Chapter 1. Introduction

Osteoarthritis (OA) is a disease that affects 27 million people in the United States (Lawrence et al. 2008). Ankle OA occurs in about 1% of world's population (Barg et al. 2013), but occurs less often than OA in the knee or hip (Cushnaghan and Dieppe 1991; Huch, Kuettner, and Dieppe 1997). Ankle OA is more often developed post-traumatically, compared to the primary development of OA in the hip and knee (Demetriades, Strauss, and Gallina 1998). Arthritis of the ankle is also more prevalent in veterans than non-veterans (Shibuya et al. 2011). End stage ankle arthritis (ESAA) is a debilitating disease, as patients are severely limited in their activities of daily living due to impaired mobility (Glazebrook 2010).

Common surgical procedures for ESAA include ankle arthrodesis (fusion) and total ankle arthroplasty (replacement) of the joint. While both of these surgeries have been successful at improving clinical outcome scores (Haddad et al. 2007) and patients are generally satisfied (Younger et al. 2015), post-operative challenges occur in both surgeries. Arthrodesis of the ankle joint can predispose patients to development of OA in distal foot joints, particularly the subtalar and talonavicular joints (Coester et al. 2001). Total ankle replacements also have a limited expected lifetime (Henricson, Nilsson, and Carlsson 2011; Haddad et al. 2007). Gait analysis shows increased range of motion in total ankle replacement patients compared to arthrodesis patients (Flavin et al. 2013; Piriou et al. 2008). But with either surgery, misalignment does occur and negatively impacts patient outcomes (Barg et al. 2011; Braito et al. 2015; Buck, Morrey, and Chao 1987; Cenni et al. 2012; Hintermann et al. 2009; Casillas and Allen 2004).

Use of cadaveric specimens in orthopaedics and biomechanics research allows for novel concepts or evaluations of procedures to be performed without potential harm to a patient. For

application to foot and ankle biomechanics specifically, cadaveric testing allows for invasive measurement techniques, that more accurately measure the small changes in foot joint motion compared to traditional motion capture analysis. A robotic gait simulator (RGS) (Aubin, Whittaker, and Ledoux 2012; Whittaker, Aubin, and Ledoux 2011) was developed at the VA Puget Sound Center for Limb Loss Prevention and Prosthetic Engineering by Dr. Patrick Aubin, to simulate the stance phase of gait with a cadaveric model. The RGS is used to examine foot and ankle function invasively, without potential harm to a patient. Further, this system allows for a variety of orthopaedic surgeries to be performed on cadaveric foot specimens, and repeatedly test them in a gait simulation, to evaluate the foot and ankle complex for each surgery or surgical condition.

The goal of this project was to use cadaveric gait simulation to quantify the effect of transverse plane rotational misalignment on ankle arthrodesis and arthroplasty surgeries. Measurements of foot joint kinematics and plantar pressure distribution will potentially give insight into the biomechanical reasons why patients have more negative outcome due to surgical misalignment. The surgical techniques and custom fixture systems developed as part of this thesis were used for similar studies examining anteroposterior translational misalignment and coronal plane rotational misalignment of both surgeries. These three directions of misalignment are the most commonly seen clinically, and have the greatest effect on the biomechanics of the foot. The six misalignment studies (three arthrodesis and three arthroplasty) will help surgeons understand how misalignment of ankle arthrodesis and arthroplasty changes foot function postoperatively. This understanding could be beneficial to inform both the initial surgery and revision of these procedures.

This thesis reports on two separate cadaveric studies, and details on how these surgeries were simulated and evaluated. Chapter 2 reports on a study of transverse plane misalignment of ankle arthrodesis with nine specimens tested in five different conditions. Chapter 3 reports on a study of the same misalignment on ankle arthroplasty with the Salto Talaris total ankle system (Integra LifeSciences, Plainsboro, NJ) with results of seven specimens tested in seven different conditions. Chapter 4 briefly compares the studies and examines future work to be done using dynamic loading of cadaveric specimens. Four appendices give more specific details on how these surgeries were implemented and how the specimens were tested. Appendix A outlines the surgical technique for the arthrodesis misalignment study. Appendix B outlines the changes made to the RGS testing protocol to successfully test specimens with ankle arthrodesis. Appendix C outlines the custom Matlab program written to more accurately and efficiently analyze plantar pressure data taken with the novel pliance (novel Electronics Inc., St. Paul, MN) pressure mat. Appendix D outlines the surgical protocol for the total ankle arthroplasty misalignment surgery.

Chapter 2. Transverse plane rotational misalignment of ankle arthrodesis minimally alters kinematics and plantar pressure in cadaveric gait simulation

Formatted for submission to the Journal of Bone and Joint Surgery.

2.1 Abstract

Background

Osteoarthritis of the ankle is a debilitating disease. For end stage ankle arthritis (ESAA), a common surgical treatment is arthrodesis of the tibiotalar joint. Ankle arthrodesis has been demonstrated to alter the kinematics of joints distal to the ankle, and long-term results show patients commonly develop osteoarthritis of these joints. Misalignment of ankle arthrodesis negatively impacts patient outcomes, and can require revision surgery. The goal of this study is to quantify the effect of transverse plane rotational misalignments on foot joint kinematics and plantar pressure distribution.

Methods

Ankle arthrodesis surgery was performed on cadaveric specimens using a custom fixture that allowed the ankle to be fused at multiple alignments in the transverse plane. Bone was removed from the tibia and talus, and the fixture was implanted using bone screws. Specimens were tested on the robotic gait simulator (RGS). The RGS uses a force plate mounted on a six-degree-of-freedom robot to contact the foot, while dynamically controlling the forces on nine extrinsic muscles of the foot to simulate walking. Gait lab data from postoperative ankle arthrodesis patients were used for the kinematic input and ground reaction forces targeted by the

RGS. Kinematics for ten foot joints, as well as the plantar pressure distribution, were measured during the trial, and compared between ankle arthrodesis misalignments.

Results

Simulation of arthrodesis gait was successful, as the RMS error for the ground reaction force was less than 5% bodyweight. Transverse plane misalignment of the ankle arthrodesis showed minimal significant changes to foot joint ranges of motion, but analysis of joint angles throughout stance phase showed an abnormal position of the naviculocuneiform and cuboid-fifth metatarsal joints due to internal rotational misalignments. No significant changes were seen in the plantar pressure analysis due to misalignment.

Conclusions

Misalignment of ankle arthrodesis showed minimal effects on joint range of motion and plantar pressure distribution. Due to the negative outcomes found with arthrodesis misalignment in patients, parameters not examined in this study such as joint stress or malunion of the fusion may more greatly impact functional outcomes.

2.2 Introduction

Symptomatic osteoarthritis (OA) affects 27 million people each year (Lawrence et al. 2008). Evidence of ankle OA has been observed in 6% of individuals in postmortem examination (Huch, Kuettner, and Dieppe 1997), but is treated in symptomatic patients nine times less commonly than knee OA (Thomas and Daniels 2003). Ankle OA is commonly posttraumatic, and can be debilitating for patients with end-stage symptoms. For these patients, surgical arthrodesis of the ankle is common. This procedure involves removal of the articular cartilage of

the tibiotalar joint, and fusion of the tibia, talus, and fibula using internal fixation (Holt et al. 1991).

Prior studies have examined the effect of ankle arthrodesis post-operatively in patients. Wu et. al (2000) observed an increase in midfoot motion in the sagittal and transverse planes between the forefoot and hindfoot in ankle arthrodesis patients compared to controls, and hypothesized that this motion contributed to the development of midfoot arthritis. In contract, comparisons between the effected and contralateral limb in ankle arthrodesis patients found a decrease in sagittal plane motion of the foot and ankle complex (Fuentes-Sanz et al. 2012). Similarly, a loaded static radiographic analysis of arthrodesis patients showed overall foot range of motion was significantly decreased, but hindfoot and midfoot motion was unchanged, when compared to the unaffected contralateral limb (van der Plaat et al. 2015). Gait analysis examining full lower limb kinematics with a multi-segment foot model showed a decrease in motion at the hip, hindfoot, and forefoot in arthrodesis patients post-operatively, compared to age-matched controls (Thomas, Daniels, and Parker 2006). Buck et al. (1987) examined alignment of ankle fusion in gait and observed decreased motion at the hindfoot and increased valgus stress at the knee in internal rotational alignment of the arthrodesis. This study determined the optimal position of ankle fusion to be plantigrade, slight valgus, and external rotation of the ankle joint. In a long-term follow-up study, ankle arthrodesis patients developed osteoarthritis of the ipsilateral foot joints significantly more than the unaffected contralateral limb (Coester et al. 2001). The most common ipsilateral joints for development of severe osteoarthritis were the subtalar and talonavicular joints, occurring in 91% and 65% of the patients, respectively.

Misalignment of ankle arthrodesis negatively impacts patient outcomes and can require surgical revision. In patients where a painful ankle arthrodesis was converted to total ankle

arthroplasty, rotational misalignment of up to ten degrees in at least one cardinal plane was observed in 28 of 30 patients (Hintermann et al. 2009). Transverse plane rotational misalignments have been identified clinically as a factor in malunion of ankle arthrodesis, and severe deformity misalignments (Figure 3.1) can require revision surgery (Casillas and Allen 2004).

Figure 2.1: An internal rotational misalignment of arthrodesis on the left ankle (Casillas and Allen 2004).

Previous studies have simulated ankle arthrodesis in a cadaveric model to determine the effect of the surgery on foot loading. In dynamic loading of cadaveric specimens, pressure measurements in Chopart's joint showed an increase of load in the talonavicular joint and decrease in load in the calcaneocuboid joint after ankle fusion. In plantar flexion and dorsiflexion motion, arthrodesis of the ankle joint caused increased frontal plane motion of the subtalar joint (Suckel et al. 2007). Axial loading of cadaveric specimens with ankle arthrodesis at various magnitudes on an unconstrained testing apparatus resulted in an increase in calcaneal inversion/eversion and tibial rotation, compared to an unfused condition (Hintermann and Nigg 1995). Specific to understanding arthrodesis misalignment, static axial loading showed an

increase peak pressure and decrease contact area in the subtalar joint when comparing coronal plane misalignment to neutrally aligned arthrodesis (Wayne et al. 1997).

The purpose of this study is to use cadaveric gait simulation to quantify the effect of internal and external rotational misalignment of ankle arthrodesis on foot bone kinematics and plantar pressure distribution. We hypothesized that internal rotational misalignment will increase range of motion of the lateral foot joints, increase peak pressure on the lateral side of the foot, and cause the center of pressure to deviate laterally. The opposite trend is expected for external rotational misalignments: an increased range of motion in medial foot joints, increased peak pressure on the medial side of the foot, and a medial deviation of the center of pressure.

2.3 Methods

Nine fresh-frozen cadaveric foot specimens were obtained for this Institutional Review Board approved study (donor age 61.3 ± 19.3 years, donor weight 88.7 ± 20.1 kg, 8 male, 1 female). Specimens were screened radiographically for major deformities by an orthopedic surgeon. Ankle arthrodesis surgery was simulated using a custom two-plate fixture and surgical technique that allowed for prescribed rotational misalignments in the transverse plane (Appendix A). Using the instrumentation from the Salto Talaris ankle arthroplasty (Integra LifeSciences, Plainsboro, NJ) with a custom designed cutting guide, an orthopedic surgeon removed bone from the tibia and talus in a box cut pattern corresponding to the exact height of the fixture. The fixture was implanted into the specimen using eight 3.5mm bone screws, directed obliquely into the tibia and talus (Figure 2.2). In order to achieve the desired misalignment, bone was removed from the articular facets of the medial and lateral malleoli. The fixture maintained neutral sagittal

and frontal plane alignment of the tibiotalar joint, but allowed for the transverse plane alignment of the tibiotalar joint to be altered and set at variable angles (Figure 2.3A). Five and ten degree misalignments of both internal (5IR, 10IR) and external (5ER, 10ER) rotational misalignments were evaluated for each specimen, along with neutral transverse plane alignment (N).

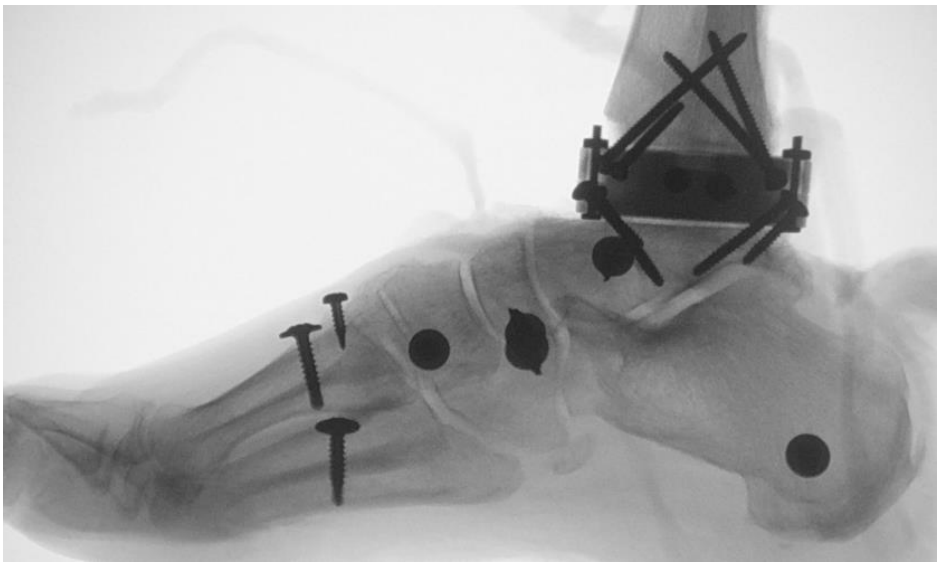

Figure 2.2: A lateral radiograph of the custom two-plate fixture and bone screws implanted in a specimen.

Prior to testing, the tibia and fibula were cut approximately 15 cm proximal to the lateral malleolus. The tendons were isolated for the following muscles: tibialis anterior, extensor hallucis longus, extensor digitorum longus, peroneus longus, peroneus brevis, flexor hallucis longus, flexor digitorum longus, tibialis posterior and triceps surae (Achilles tendon). All other soft tissue proximal to the tibiotalar joint was removed. A 12.7 mm diameter hole was bore into the tibial shaft, and a custom mounting fixture was used to pot the tibia in polymethylmethacrylate (LangDental Mfg. Co., Wheeling, IL) and rigidly connect the tibia to the mounting frame of the gait simulator. Screws were implanted in eight bones in the foot. Four-marker reflective motion capture marker clusters were rigidly connected to these screws.

Markers were also placed on the dorsal skin of the hallux and rigidly attached to the tibial mounting fixture (Figure 2.3B).

Figure 2.3: A) The fusion misalignment fixture implanted into a specimen showing an internal rotation misaligned position with the tendons dissected proximal to the ankle joint and B) an anterior view of a test specimen, with tendon clamps and strings, Vicon clusters in bone screws, and the tibia mount.

Specimens were tested on the RGS (Aubin, Whittaker, and Ledoux 2012), which consists of a force plate mounted on a six-degree-of-freedom rotopod robot (Mikrolar, Inc., Hampton, NH) (Figure 2.4, Appendix B). The force plate contacts the foot to simulate the ground contacting the foot during gait. Muscle forces are simulated by linear actuators connected to each of the isolated tendons and are dynamically prescribed during stance phase. Metal clamps were used to connect to the tibialis anterior and Achilles tendons, with a liquid nitrogen freeze clamp

used on the Achilles tendon. Each of the other isolated tendons were connected using a nylon string tied around a small nut and bolt through the tendon. Muscle forces are derived from electromyography data from the literature and scaled by average physiologic cross sectional area for each muscle (Aubin, Whittaker, and Ledoux 2012; Fukunaga et al. 1996; Wickiewicz et al. 1983; Zhou et al. 1995). Simulations were performed at 25% of each individual specimen donor's bodyweight and one-sixth *in vivo* speed, to prevent failure of the fusion fixture-bone interface. The input tibia kinematics and target ground reaction forces used to control the simulation were taken from the average of gait lab data from ten patients, all one-year postoperative from ankle arthrodesis surgery. The RGS changes the force on the tibialis anterior tendon and Achilles tendon during certain portions of stance and makes minor specific changes to the tibia-to-ground trajectory of the robot to match this *in vivo* vertical ground reaction force (Aubin, Whittaker, and Ledoux 2012). For each trial, three consecutive gait simulations were performed to precondition the specimen tissues before data was collected on the fourth simulation. Three trials were collected for each misalignment condition. The order of the arthrodesis misalignment conditions was randomized for each specimen, to minimize any bias in the data from degradation of tissue over the course of the simulations.

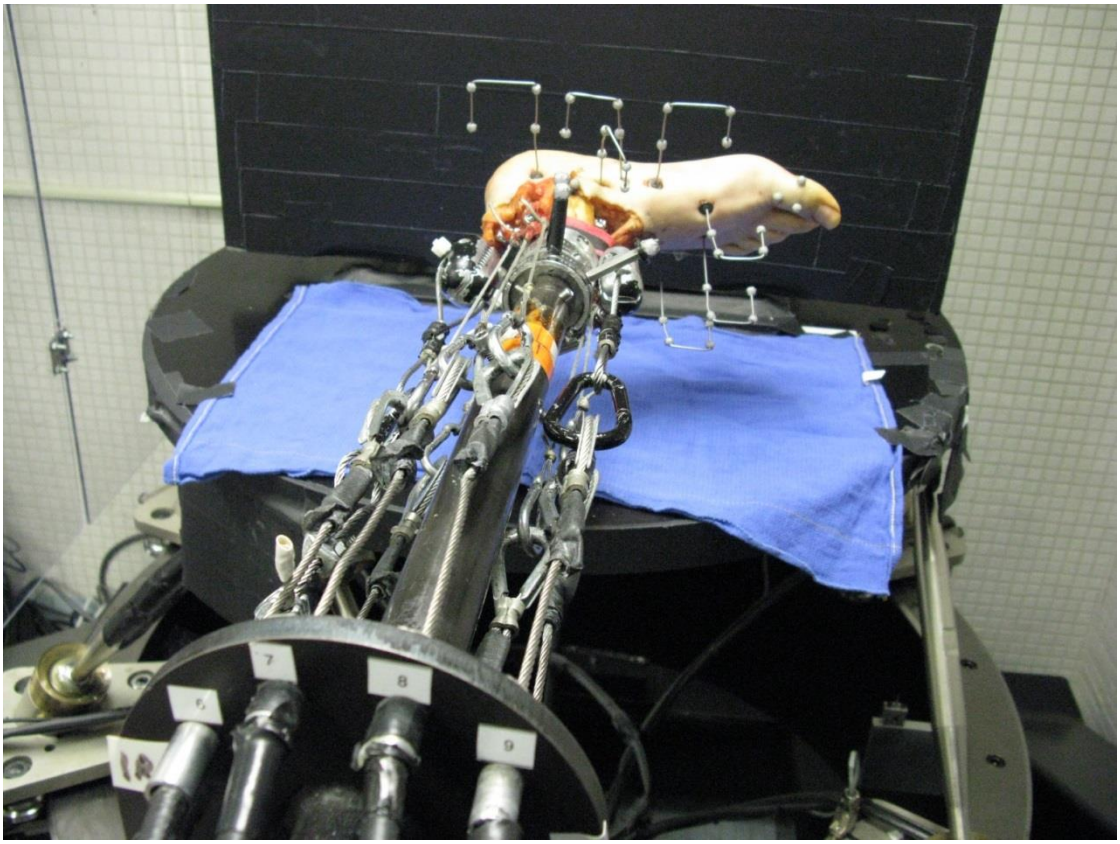

Figure 2.4: A specimen mounted on the robotic gait simulator.

Foot joint kinematics and plantar pressure data were collected for each simulation. An eight-camera optical motion capture system (Vicon Motion Systems, Denver, CO) was used to track the motion capture marker clusters. A custom ten-segment foot model was used to determine joint kinematics in ten foot joints (Whittaker, Aubin, and Ledoux 2011). Parameters of interest included the range of motion and the joint angle at each percent stance phase for the following ten joints: tibiotalar, talonavicular, talocalcaneal, naviculocuneiform, calcaneocuboid, cuneiform-first metatarsal, cuneiform-third metatarsal, cuboid-fifth metatarsal, first metatarsophalangeal, and the relationship between the talus and first metatarsal. A pliance pressure sensor (novel Electronics Inc., St. Paul, MN) was placed between the foot and the force plate on the RGS and measured plantar pressure during each simulation. In post-processing, a plot of the maximum pressure measured was registered to a radiograph (Figure 2.5) of the

specimen, and the pressure sensors were partitioned into ten regions of interest of the foot identified radiographically, including the heel, lateral midfoot, medial midfoot, first to fifth metatarsals, hallux, and lesser toes (Appendix C). The peak pressure over the entire stance phase was determined for each region for each trial. The center of pressure was determined relative to the axis from the posterior calcaneus through the second ray (De Cock et al. 2008) and was analyzed at each 1% of stance phase.

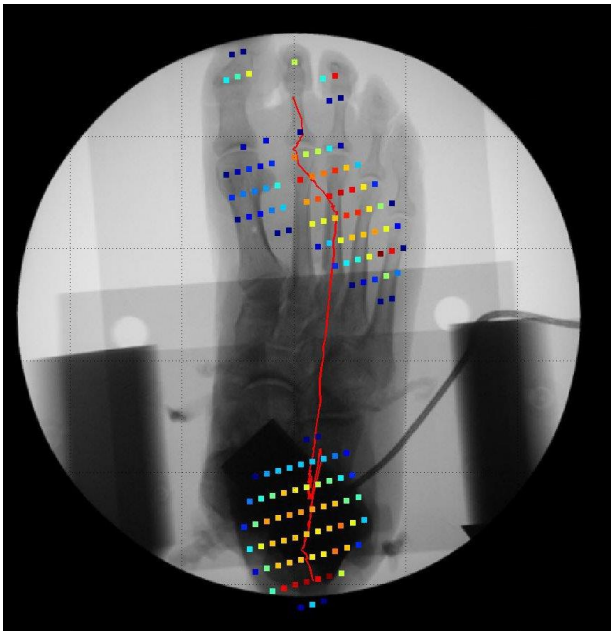

Figure 2.5: Plantar pressure data registered to a radiograph.

Linear mixed effects regression was used to determine if the (dependent) outcome variable differed by condition type (modeled as the independent fixed effect with four dummy variables). Specimen and specimen condition interaction were modeled as random effects. First, an omnibus test for association between outcome variable and condition was carried out. If significant, pairwise comparisons were carried out comparing all 4 misalignment conditions to the neutral condition using simultaneous inference. For omnibus tests of average joint angles and center of pressure variables at each 1% stance phase, p-values were adjusted for multiple

comparisons using the method of Benjamini and Hochberg (Benjamini and Hochberg 1995). Results for pairwise differences are presented with 95 percent confidence intervals. All analyses were performed in R 3.2.5 (Team 2013) with the lme4 (Bates et al. 2015) package to carry out the linear mixed effects regression and the multcomp package (Hothorn, Bretz, and Westfall 2008) to estimate the 95% confidence intervals.

2.4 Results

Gait simulation of arthrodesis was successful, as the *in vivo* target parameters for the RGS were matched. The tibia-to-ground kinematics of the simulations tracked the *in vivo* kinematics (Figure 2.6) and all directions of ground reaction forces were matched within five percent of body weight (Figure 2.7). The vertical ground reaction force was matched within 2.2% bodyweight RMS error. The anteroposterior and mediolateral ground reaction forces, which were not explicitly controlled for by the simulator, were within 4.4% and 2.1% bodyweight RMS error of the *in vivo* ground reaction forces, respectively.

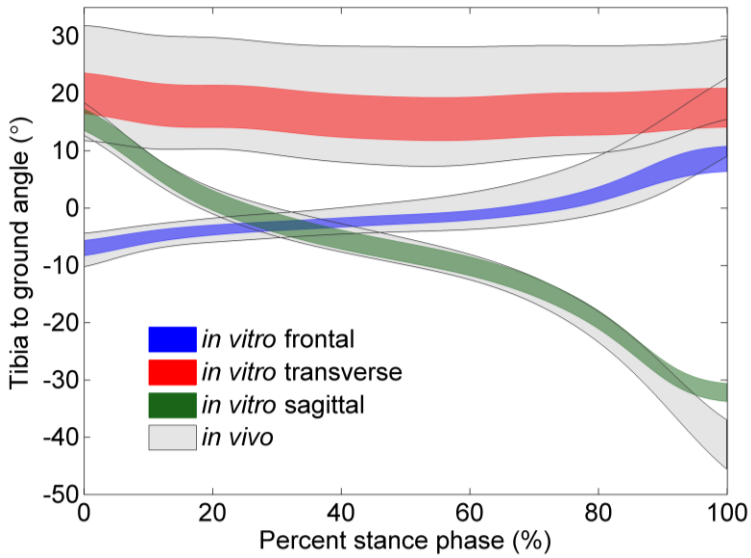

Figure 2.6: Tibia-to-ground kinematics comparing *in vivo* targets and *in vitro* simulation results, for frontal, transverse, and sagittal plane angles.

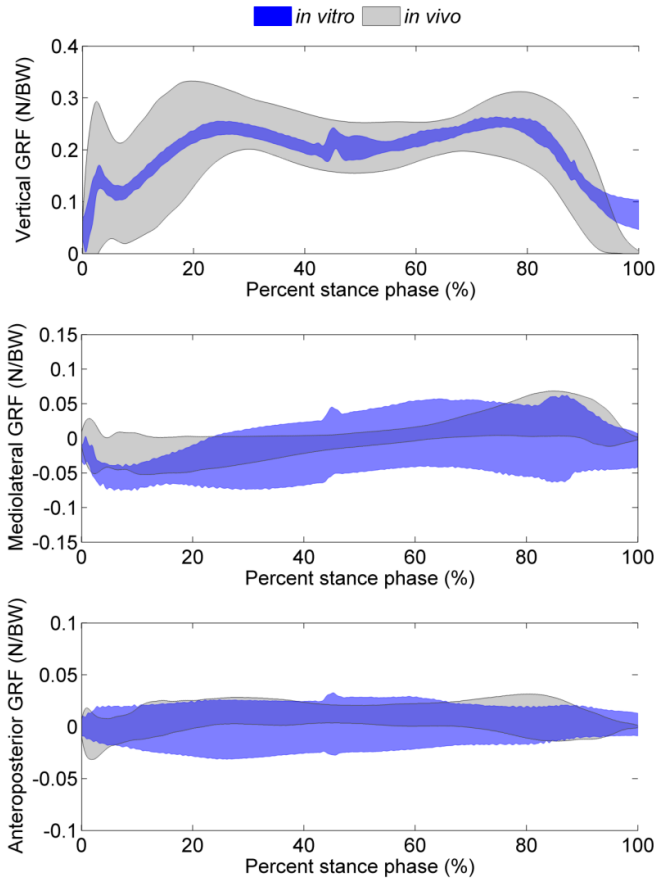

Figure 2.7: Results of the gait simulation, comparing the ground reaction forces (GRF) in each plane for the target *in vivo* gait lab data and the *in vitro* RGS simulations.

Fusion of the tibiotalar joint was achieved, with an average range of motion reduced to 2.5° or less in each cardinal plane. This was determined to be representative of the standard surgerical protocol, within the limitations of dynamically loading a cadaveric specimen, as shown by a validation study comparing the misalignment fixture to the standard protocol for arthrodesis surgery (Section 2.6 Supplemental Data Appendix 1).

Few significant changes in joint range of motion occurred due to misalignment (Tables 2.1 and 2.2). A significant decrease in sagittal plane range of motion occurred in the talocalcaneal joint for the 5ER condition compared to neutral (-1.0°, 14% decrease, $p = 0.002$).

In the cuneiform-first metatarsal joint, a significant decrease in frontal plane range of motion occurred for the 10IR condition compared to neutral (-1.0°, a 21% decrease, $p=0.009$), and a significant increase in transverse plane range of motion occurred for the 5IR conditions compared to neutral (0.9°, 30% decrease, $p<0.001$).

There were no significant changes in range of motion due to misalignment in several joints (Tables 2.1-2.2). Measured change in range of motion due to misalignments were less than 10% across all conditons for the sagittal plane of the naviculocuneiform joint, calcaneocuboid joint, and first metatarsal-talus relationship, and frontal plane of the first metatarsophalangeal joint.

For joint angle analyzed throughout stance phase, several intervals of significant changes were observed due to misalignment (Table 2.3). The tibiotalar joint was significantly internally rotated for the 10IR and 5IR conditions compared to neutral, and significantly externally rotated for the 10ER and 5ER conditions compared to neutral throughout stance phase, indicating that the desired misalignments were applied with the fusion misalignment fixture. The naviculocuneiform joint was significantly plantar flexed from 36-71% and 79-91% of stance phase for the 10IR alignment compared to neutral, and the 5IR alignment compared to neutral. The cuboid-fifth metatarsal joint was significantly everted from 38-95% of stance phase and dorsiflexed from 20-100% of stance phase for the 10IR alignment compared to neutral. This joint was also significantly everted from 61-77% and dorsiflexed from 66-93% of stance phase for the 5IR alignment compared to neutral, and dorsiflexed from 53-73% of stance phase for the 5ER alignment compared to neutral.

Table 2.1. Hindfoot joints mean range of motion (ROM) ± standard error for neutral arthrodesis, changes in range of motion for each misaligned condition with 95% confidence interval (CI) and omnibus p-value between all conditions.

Joint Angle	Mean ROM (degrees)	Difference in ROM between misaligned and neutral conditions (degrees)				p
	N ± SE	10ER-N (CI)	5ER-N (CI)	5IR-N (CI)	10IR-N (CI)	
Tibiotalar-F	1.4 ± 0.4	-0.3 (-1.0, 0.4)	0.1 (-0.5, 0.7)	0.2 (-0.5, 0.9)	-0.2 (-0.8, 0.4)	0.59
Tibiotalar-T	1.6 ± 0.2	-0.3 (-0.8, 0.3)	-0.0 (-0.7, 0.7)	0.1 (-0.4, 0.7)	-0.3 (-1.0, 0.4)	0.55
Tibiotalar-S	2.4 ± 0.2	0.2 (-0.7, 1.2)	0.2 (-0.4, 0.7)	-0.1 (-0.8, 0.5)	0.0 (-0.6, 0.7)	0.84
Talonavicular-F	7.9 ± 0.7	-0.4 (-1.6, 0.7)	0.2 (-0.7, 1.2)	0.3 (-0.5, 1.1)	1.1 (-0.5, 2.8)	0.25
Talonavicular-T	7.4 ± 1.2	-0.1 (-0.8, 0.6)	0.0 (-2.1, 2.1)	1.6 (-0.9, 4.1)	-0.1 (-2.3, 2.1)	0.62
Talonavicular-S	7.6 ± 1.4	0.0 (-1.1, 1.2)	0.3 (-1.6, 2.3)	1.1 (-0.9, 3.1)	0.5 (-1.1, 2.1)	0.57
Talocalcaneal-F	3.7 ± 0.7	0.1 (-0.8, 1.0)	0.2 (-0.5, 0.9)	0.1 (-0.6, 0.8)	0.7 (-0.6, 1.9)	0.63
Talocalcaneal-T	4.6 ± 0.5	-0.1 (-0.9, 0.7)	-0.6 (-1.3, 0.1)	0.4 (-0.8, 1.6)	-0.2 (-1.2, 0.7)	0.28
Talocalcaneal-S	7.4 ± 0.8	-0.6 (-1.5, 0.4)	-1.0 (-1.7, -0.3)*	-0.1 (-1.4, 1.2)	-0.1 (-1.4, 1.2)	0.036
Naviculocuneiform-F	3.3 ± 0.7	0.6 (-0.1, 1.3)	-0.2 (-0.7, 0.4)	0.1 (-0.6, 0.7)	0.2 (-0.5, 0.9)	0.23
Naviculocuneiform-T	2.5 ± 0.4	0.1 (-0.5, 0.7)	0.0 (-0.4, 0.4)	-0.4 (-0.8, 0.1)	-0.2 (-0.9, 0.4)	0.27
Naviculocuneiform-S	6.0 ± 0.8	-0.1 (-1.2, 1.0)	-0.6 (-1.7, 0.5)	0.1 (-0.7, 0.9)	-0.5 (-1.6, 0.5)	0.47
Calcaneocuboid-F	3.0 ± 0.3	0.4 (-0.9, 1.8)	-0.1 (-1.2, 1.0)	1.4 (-2.3, 5.1)	0.3 (-0.9, 1.4)	0.67
Calcaneocuboid-T	5.9 ± 2.5	1.0 (-2.3, 4.2)	0.7 (-1.0, 2.3)	0.7 (-3.0, 4.4)	1.4 (-0.5, 3.2)	0.44
Calcaneocuboid-S	7.3 ± 2.4	0.2 (-3.1, 3.6)	0.2 (-1.4, 1.8)	0.6 (-4.7, 5.8)	0.7 (-1.0, 2.4)	0.88

F-Frontal, T-Transverse, S-Sagittal. *****Pairwise comparisons where $p < 0.05$.
10ER-10° external rotational misalignment, 5ER-5° external rotational misalignment, N-neutrally aligned surgery, 5IR-5° internal rotational misalignment, 10IR-10° internal rotational misalignment.

Table 2.2**.** Forefoot joints mean range of motion (ROM) ± standard error for neutral arthrodesis, changes in range of motion for each misaligned condition with 95% confidence interval (CI) and omnibus p-value between all conditions.

Joint Angle	Mean Angle (degrees)	Difference between misaligned and neutral conditions in degrees (95% confidence interval)				p
	N ± SE	10ER-N (CI)	5ER-N (CI)	5IR-N (CI)	10IR-N (CI)	
Cuneiform-1st Metatarsal-F	4.7 ± 0.4	-0.4 (-1.3, 0.4)	0.1 (-0.8, 1.0)	-0.7 (-1.5, 0.0)	-1.0 (-1.8,-0.2)*	0.01
Cuneiform-1st Metatarsal T	3.0 ± 0.6	0.3 (-1.1, 1.8)	0.6 (-0.3, 1.5)	0.9 (0.4, 1.4)*	0.8 (-0.1, 1.7)	0.0015
Cuneiform-1st Metatarsal-S	3.8 ± 0.5	-0.2 (-1.0, 0.6)	0.5 (-0.4, 1.5)	-0.1 (-1.0, 0.8)	-0.1 (-0.9, 0.6)	0.65
Talus-1st Metatarsal-F	6.1 ± 0.8	-0.9 (-2.9, 1.1)	-0.1 (-1.1, 1.0)	-0.9 (-1.9, 0.0)	0.0 (-2.0, 2.0)	0.18
Talus-1st Metatarsal-T	6.3 ± 0.4	-0.2 (-1.0, 0.5)	0.5 (-1.0, 1.9)	0.6 (-0.6, 1.9)	0.7 (-0.2, 1.6)	0.17
Talus-1st Metatarsal-S	16.0 ± 1.1	-0.3 (-1.5, 1.0)	-0.3 (-1.4, 0.8)	0.5 (-0.7, 1.8)	0.2 (-1.3, 1.6)	0.7
Cuneiform-3rd Metatarsal-F	3.0 ± 0.3	-0.2 (-1.5, 1.0)	-0.4 (-1.1, 0.2)	-0.3 (-1.0, 0.4)	-0.4 (-0.9, 0.1)	0.17
Cuneiform-3rd Metatarsal-T	2.1 ± 0.4	0.4 (-0.4, 1.1)	0.3 (0.0, 0.6)	0.4 (-0.4, 1.2)	0.9 (-0.1, 1.9)	0.025
Cuneiform-3rd Metatarsal-S	3.8 ± 0.5	-0.4 (-1.0, 0.3)	0.5 (-0.8, 1.7)	-0.1 (-1.3, 1.0)	0.1 (-1.7, 2.0)	0.58
Cuboid-5th Metatarsal-F	5.1 ± 0.6	0.3 (-1.1, 1.8)	0.0 (-1.2, 1.3)	1.2 (-2.5, 4.9)	0.2 (-1.4, 1.7)	0.9
Cuboid-5th Metatarsal-T	8.3 ± 1.5	-0.5 (-3.9, 2.8)	0.3 (-3.3, 3.8)	1.2 (-1.7, 4.1)	1.1 (-0.7, 2.9)	0.49
Cuboid-5th Metatarsal-S	12.2 ± 1.4	-0.6 (-3.5, 2.3)	1.8 (-0.9, 4.4)	2.0 (-0.5, 4.4)	1.3 (-1.6, 4.2)	0.11
1st Metatarsophalangeal-F	8.7 ± 1.3	-0.6 (-2.6, 1.4)	-0.3 (-1.8, 1.3)	-0.1 (-2.0, 1.7)	-0.8 (-3.6, 2.0)	0.86
1st Metatarsophalangeal-T	6.5 ± 0.8	0.0 (-1.8, 1.7)	-0.3 (-1.7, 1.2)	1.8 (0.0, 3.7)	0.2 (-2.1, 2.5)	0.25
1st Metatarsophalangeal-S	22.8 ± 2.3	-0.5 (-3.0, 1.9)	0.1 (-2.4, 2.5)	0.2 (-1.9, 2.3)	0.1 (-3.1, 3.3)	0.98

F-Frontal, T-Transverse, S-Sagittal. *Pairwise comparisons where $p < 0.05$.

10ER-10° external rotational misalignment, 5ER-5° external rotational misalignment, N-neutrally aligned surgery, 5IR-5° internal rotational misalignment, 10IR-10° internal rotational misalignment.

Table 2.3. Intervals of stance phase with significant changes in joint angles between misalignment conditions and neutral alignment.

Joint or Relationship	Misalignment condition			
	10IR to Neutral	5IR to Neutral	5ER to Neutral	10ER to Neutral
Tibiotalar	0-100% internally rotated	0-100% internally rotated	0-100% externally rotated	0-100% externally rotated
Talonavicular	N/S	N/S	N/S	N/S
Naviculocuneiform	36-71%, 79-91% plantar flexed	36-71%, 79-91% plantar flexed	N/S	N/S
Talocalcaneal	N/S	N/S	N/S	N/S
Calcaneocuboid	N/S	N/S	N/S	N/S
Cuneiform-First Metatarsal	N/S	N/S	N/S	N/S
Talus-First Metatarsal	N/S	N/S	N/S	N/S
Cuneiform-Third Metatarsal	91-100% adduction	N/S	N/S	N/S
Cuboid-Fifth Metatarsal	38-95% everted, 20-100% dorsiflexed	61-77% everted, 66-93% dorsiflexed	53-73% dorsiflexed	N/S
1st Metatarsophalangeal	N/S	N/S	N/S	N/S

N/S-No significant changes observed,10ER-10° external rotational misalignment, 5ER-5° external rotational misalignment, N-neutrally aligned surgery, 5IR-5° internal rotational misalignment, 10IR-10° internal rotational misalignment.

Minimal changes were seen in pressure measurements due to misalignment. Pressure data were only collected on eight of the nine specimens, and was not detected in the medial and lateral midfoot regions for enough specimens to perform analysis on these regions. A significant decrease in pressure was observed for the 5ER condition compared to neutral (-9 kPa) in the third metatarsal region (Table 2.4). No significant changes in mediolateral center of pressure deviation due to misalignment were observed (Figure 2.8).

Table 2.4. Peak pressure ± standard error (SE) measured in each region of the foot for the neutrally aligned arthrodesis and the change in maximum pressure measurement for each misaligned condition with 95% confidence interval (CI) and omnibus p-value between all conditions.

Region	Neutral alignment peak pressure (kPa) ± SE	Difference between misaligned and neutral conditions in kPa (95% confidence interval)				p
		10ER-N (CI)	5ER-N (CI)	5IR-N (CI)	10IR-N (CI)	
Great Toe	93 ± 21	15 (-6, 35)	15 (-1, 31)	4 (-9, 17)	-19 (-41, 4)	0.018
Lesser Toes	88 ± 12	5 (-7, 18)	-1 (-13, 13)	-1 (-14, 11)	0 (-14, 15)	0.77
First Metatarsal	101 ± 22	6 (-9, 22)	10 (-12, 32)	1 (-14, 17)	-19 (-53, 16)	0.36
Second Metatarsal	113 ± 15	0 (-19, 20)	2 (-11, 14)	-2 (-9, 4)	-6 (-24, 12)	0.76
Third Metatarsal	105 ± 7	-4 (-14, 5)	-9 (-16, -3)*	1 (-16. 18)	1 (-23, 24)	0.054
Fourth Metatarsal	102 ± 16	-7 (-19, 5)	-6 (-18, 5)	-5 (-24, 14)	0 (-37, 36)	0.39
Fifth Metatarsal	108 ± 27	-5 (-24, 14)	-12 (-30, 6)	-4 (-23, 15)	23 (-24, 71)	0.29
Heel	151 ± 9	-10 (-24, 5)	0 (-19, 18)	6 (-4, 17)	7 (-5, 19)	0.11

*Pairwise comparisons where $p < 0.05$.

10ER-10° external rotational misalignment, 5ER-5° external rotational misalignment, N-neutrally aligned surgery, 5IR-5° internal rotational misalignment, 10IR-10° internal rotational misalignment.

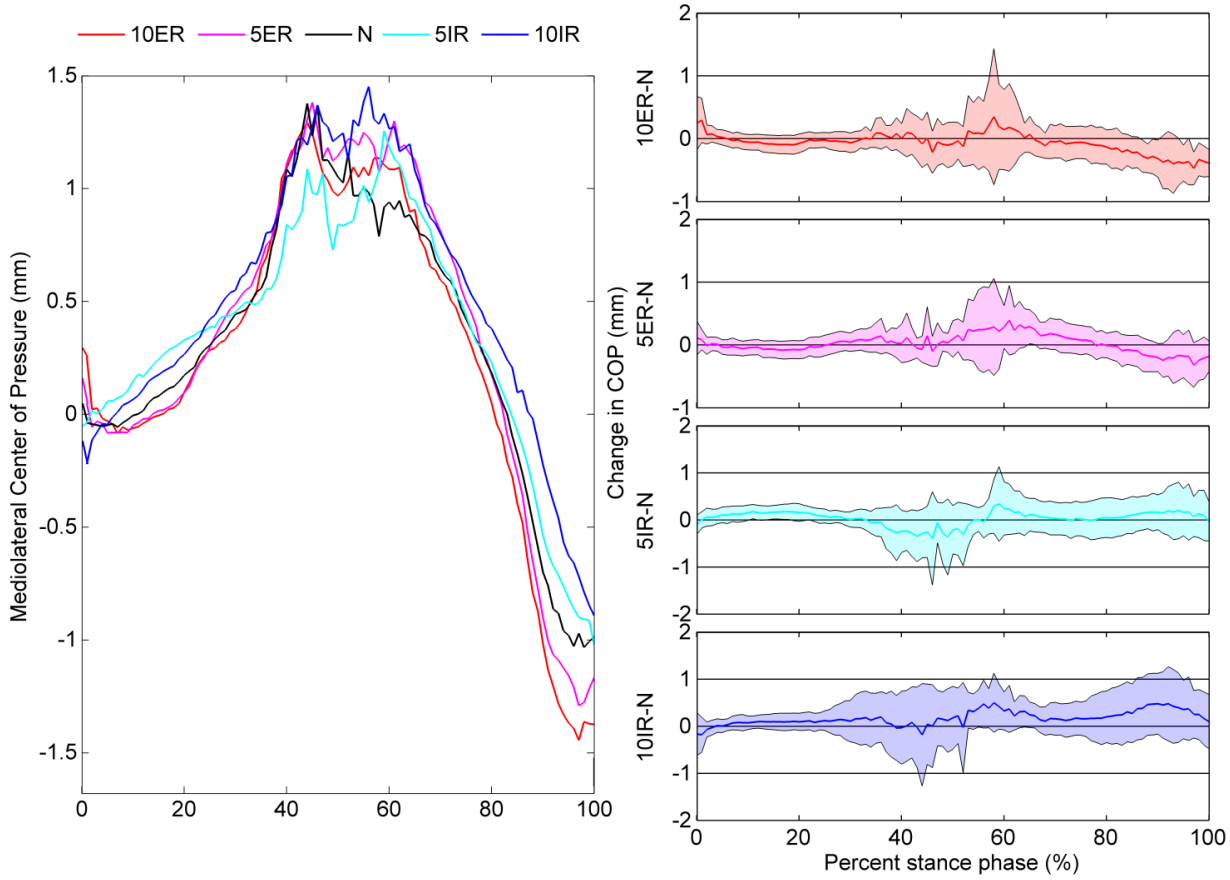

Figure 2.8: Average mediolateral center of pressure for each condition, and pairwise comparisons between each misaligned condition and the neutral arthrodesis surgery. 10ER-10° external rotational misalignment, 5ER-5° external rotational misalignment, N-neutrally aligned surgery, 5IR-5° internal rotational misalignment, 10IR-10° internal rotational misalignment.

2.5 Discussion

Cadaveric gait simulation with a custom misalignment fixture was used to evaluate ankle arthrodesis to determine how surgical misalignment changes joint kinematics and plantar pressure distribution of the foot. Limited changes were observed in both range of motion and plantar pressure distribution due to surgical misalignment. The hypotheses of joint motion and plantar loading shifting medially and laterally on the foot for internal and external rotational misalingments, respectively, was not supported. These parameters appear to be affected

differently by transverse plane misalignment of ankle arthrodesis than initially hypothesized. Significant changes in range of motion due to misalignment were observed for the sagittal plane of the talocalcaneal joint and frontal and transverse planes of the cuneiform-first metatarsal joint. However, due to the lack of significant changes in other joint ranges of motion, the study suggests that misalignment of ankle arthrodesis surgery in general does not substantially affect range of motion of hindfoot and midfoot joints. However, some internal rotational misalignments did affect joint angles throughout stance. In particular, the naviculocuneiform joint was in a more plantar flexed position and cuboid-fifth metatarsal joint was in a more dorsiflexed and abducted position in gait due to internal rotational misalignment. These findings suggest that these joints may be abnormally loaded when internal rotational misalignments of ankle arthrodesis occur.

Transverse plane misalignment of ankle arthrodesis has yet to be extensively studied, especially in a cadaveric model. Rotatational misalignment of arthrodesis has been associated with malunion (Hintermann et al. 2009; Casillas and Allen 2004), an aspect of the procedure the current study did not examine. Previous studies on ankle arthrodesis with dynamic loading of cadaveric specimens have examined the effect on the subtalar joint specifically. Our results showed a decrease in the sagittal plane range of motion, but no significant changes in the joint angles throughout stance for the subtalar joint or plantar pressure in the heel region. Wayne et. al applied static axial loading of various levels to cadaveric specimens and found a decrease in contact area of the subtalar joint due to arthrodesis misalignment in the coronal plane.(Wayne et al. 1997) While the present study does not measure contact area, a decrease in the sagittal plane range of motion for the talocalcaneal joint shows that transverse plane misalignment of ankle arthrodesis does have some influence on the motion of the subtalar joint. Suckel et al. found that the joint force and pressure was tranferred from the calcaneocuboid joint to the talonavicular

joint after ankle arthrodesis (Suckel et al. 2007). These parameters were not measured directly in the current study, but the lack of changes of motion between the talonavicular or calcaneocuboid joint suggest that transverse plane rotational misalignment minimally affects these joints. Several other studies compared unfused controls or conditions to examine the effect of ankle arthrodeis on the surrounding joints (Wu et al. 2000; Fuentes-Sanz et al. 2012; Hintermann et al. 2009; Hintermann and Nigg 1995; van der Plaat et al. 2015). While the current study did not explicitly examine the difference between unfused and ankle arthrodesis specimens, compared to a foot with a normal tibiotalar joint tested on the RGS (Whittaker, Aubin, and Ledoux 2011), the ranges of motion at each joint were reduced for all conditions of misalignment in the present study.

Several limitations existed in this study. Simulation of gait at 25% donor bodyweight was required to maintain fixation at the bone-fixture interface. This magnitude of loading in combination with the kinematic input of the system being from fused patients showed more limited motion of the foot. In comparison with an *in vivo* bone pin study of normal foot kinematics (Lundgren et al. 2008), ranges of motion were noticeably less at all measured joints. In a previous study with the RGS, examining changes in joint kinematics due to talonavicular joint fusion at 25% bodyweight testing, the ranges of motion at all distal foot joints for the unfused trials were also greater the values in this study (Wahl et al. 2016). In the plantar pressure measurement, the pattern of pressure was noticibly different from a physiologic distribution, particularly in the center of pressure for specimens with lower donor bodyweights. There was an uneven distribution of the sex of specimen donors (8 male, 1 female). However, there was no noticable differences between the single female donor specimen and male donor specimens, thus we consider the specimens obtained to be acceptable. The number of specimens tested (nine) reduced the statistical power, a limitation of using a cadaveric model for gait simulation.

This study allowed for a novel concept of multiple, specifically controlled misalignments of ankle arthrodesis to be tested in a cadaveric specimen in stance phase gait simulation. The overall lack of significant changes in joint kinematics or plantar pressure across the misaligned conditions suggests that transverse plane rotational misalignment may minimally affect these parameters. Based on negative patient outcomes associated with misalignment of ankle arthrodesis, misalignments may have a greater effect on parameters not evaluated in this study, such as joint stress or union of the tibiotalar fusion. Additional studies quantifying how misalignment affects union of the tibiotalar joint fusion and joint stresses, particularly of the subtalar and talonavicular joint, could lead to determining the biomechanical reasons for poorer patient results due to ankle arthrodesis misalignment. A future study examining joint kinematics and plantar pressure using the RGS to compare ankle arthrodesis and unfused ankle conditions within the same specimen could potentially provide insight into the development of adajecent joint OA postoperatively.

2.6 Supplemental Appendix 1: Validation of ankle fusion misalignment fixture compared to internal fixation.

During the experiments, it was observed that a non-zero range of motion was measured across the fused joint, and thus the use of a custom misalignment fixture to achieve tibiotalar joint fusion was further evaluated. To determine if the misalignment fixture replicated surgery well, a validation study was performed. Ankle arthrodesis using the gold standard surgical protocol of internal fixation of the tibiotalar joint was performed on a specimen by an experienced orthopedic surgeon. This included three 6.5 mm bone screws fusing the tibia and talus in lag fashion to compress the joint surface. The tibiofibular and talofibular joints were also

fused with two 3.5mm screws (Figure 2.9). This specimen was then tested on the RGS with the same protocol as the specimens with the misalignment fixture.

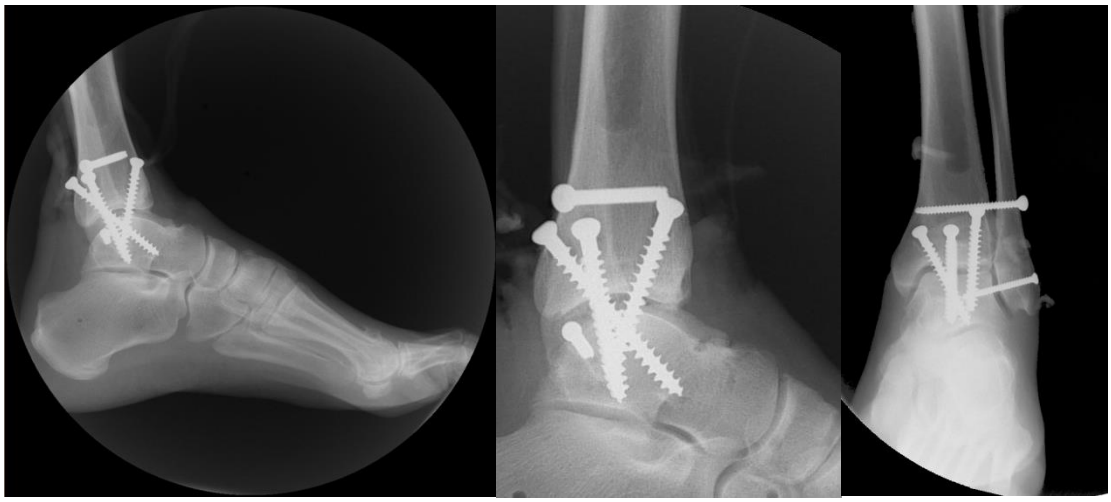

Figure 2.9: Arthrodesis of the ankle using standard internal fixation protocol.

The ranges of motion were similar for both the custom misalignment fixture and standard internal fixation in the transverse and sagittal planes (Table 2.5). The similarity between the sagittal plane, the major plane of motion for the tibiotalar joint, suggests these fixation methods agree. The internal fixation validation specimen did exhibit less motion in the frontal plane. In comparison to the normal, unfused ankle (Whittaker, Aubin, and Ledoux 2011), the misalignment fixation removes a substantial amount of motion in all planes. This discrepancy in frontal plane motion can be attributed to the lack of variability inherent in testing a single specimen for the validation study. Statistical analysis performed in to determine the average difference between the misalignment fixture and internal fixation validation, as well as 95% confidence intervals between the two (Table 2.6). Each confidence interval includes zero, and is sufficiently small to conclude there is no significant difference between the two fixations. The main mechanism of healing and formation of union in patients is bony ingrowth, a mechanism of

fixation not possible in cadaveric specimens. Due to the lack of differences in range of motion to the standard surgical internal fixation protocol, we concluded that the misalignment fixture replicated the surgery well, within the limitations of using a cadaveric model.

Table 2.5. Comparison of tibiotalar joint range of motion for misalignment fixture, validation study, and an unfused (normal) ankle.

Fusion Method	Tibiotalar joint range of motion (degrees)		
	Frontal	Transverse	Sagittal
Misalignment Fixture	1.43 ± 0.83	1.49 ± 0.76	2.46 ± 0.77
Internal Fixation Validation	0.38 ± 0.02	1.43 ± 0.07	2.85 ± 0.08
Unfused (normal) ankle	6.2 ± 3.8	11.0 ± 6.5	23.2 ± 4.6

Table 2.6. Difference and 95% confidence interval (CI) of tibiotalar joint range of motion between the misalignment fixture and internal fixation validation study.

Joint Angle		Difference in range of motion in degrees (CI)
Tibiotalar joint	Frontal	-0.275 (-2.75, 0.66)
	Transverse	-0.232 (-1.56, 1.48)
	Sagittal	-0.237 (-1.11, 1.94)

Chapter 3. Transverse Plane Misalignment of Total Ankle Arthroplasty in Cadaveric Gait Simulation

Formatted for submission to the Journal of Bone and Joint Surgery.

3.1 Abstract

Background

End-stage osteoarthritis can dramatically impair mobility for patients and total ankle arthroplasty (TAA) is a common surgical treatment for these patients. Misalignment of TAA does occur, and it can contribute to poorer patient outcomes, change range of motion of the ankle joint, and increase stress on the articular surfaces of the implant. The goal of this study is to quantify the effect of rotational misalignment of TAA on foot joint kinematics and plantar pressure distribution.

Methods

Seven fresh-frozen cadaveric foot specimens were obtained for the study. A custom surgical technique and fixture was designed to implant the Salto Talaris total ankle system into the specimen such that the neutral alignment replicated the in vivo surgery, but misalignments could be applied to the TAA. Specimens were tested in five, ten, and fifteen degree misalignments of internal and external rotation, in addition to the neutrally aligned surgery. Specimens were tested on the robotic gait simulator (RGS), which simulates walking and muscle tension on the cadaver specimen. Joint kinematics and plantar pressure data were measured, for these one-sixth in vivo speed and 50% bodyweight simulations.

Results

Internal rotational misalignment of the TAA significantly increases tibiotalar joint range of motion in the frontal plane. The misalignments also caused significant change in range of motion in the talocalcaneal, calcaneocuboid, and cuneiform-first metatarsal joints, and talus-first metatarsal relationship. Plantar pressure data was not significantly changed due to TAA misalignment.

Conclusions

Transverse plane rotational misalignment of TAA altered joint kinematics of not only the ankle joint, but distal foot joints as well. The effects of these changes in motion could be further analyzed with pressure measurement across the implant, to determine the effect on tibial bearing wear. Limited plantar pressure changes indicate these rotational misalignments do not greatly change plantar pressure distribution in gait.

3.2 Introduction

Ankle osteoarthritis is a debilitating disease that can dramatically impact activities of daily living for individuals, particularly in its end stage form. For these patients, surgical treatment with total ankle arthroplasty (TAA) improves patient mobility and overall functionality postoperatively (Buechel, Buechel, and Pappas 2003; Pyevich et al. 1998; Usuelli et al. 2016). Recent design improvements to TAA systems have improved revision rates (Henricson, Nilsson, and Carlsson 2011) compared to the first generation of devices, resulting in more widespread use of this treatment.

Misalignment of the TAA components can occur in surgery. In a radiographic analysis of 173 patients postoperatively, 15% of cases showed malpositioning (Preyssas et al. 2012). In another radiographic study of 81 patients, five (6%) exhibited misalignment in the coronal plane (Braito et al. 2015). Component misalignments can lead to negative patient outcomes and functionality. A more anterior position of the talar component relative to the tibia showed an increase in range of motion at the ankle joint (Cenni et al. 2012). The anteroposterior offset ratio of the talar and tibial components was measured for 317 patients retrospectively, and found significantly better patient outcomes for an offset ratio of zero, in both pain and range of motion (Barg et al. 2011). In contrast, examination of 108 patients post-operatively showed no difference in range of motion or clinical outcome score due to more anterior alignment of talar components compared to neutral (Lee et al. 2013). Similarly, a further examination of posterior translation of talar components of TAA showed migration of the implant in the first six months postoperatively, but no difference was found in range motion or patient outcome scores due to this change in alignment (Usuelli et al. 2016).

Cadaveric loading and computational simulation have been commonly utilized tools for evaluation of the effect of TAA implantation and TAA misalignment on the motion and loading of the foot. Dynamic loading and pressure measurement of the articulating surfaces of the TAA components determined that internal and external rotational misalignment of the talar component increases stress and decreases contact area compared to neutral alignment (Fukuda et al. 2010). When loading the specimen to represent sagittal plane motion of the ankle, anterior translational positioning of the TAA talar component limited range of motion of the tibiotalar joint (Tochigi et al. 2005). A similar study examining the effect of TAA misalignment on ligament strain showed a decrease in anterior talofibular ligament displacement due to external rotational misalignment,

and anteroposterior translational misalignment greatly affected several ligamentous structures constraining the ankle joint (Saltzman et al. 2004). A finite element model of TAA validated with loading of cadaveric specimens showed increased contact pressures on the tibial component due to external rotational misalignment of the talar component (Espinosa et al. 2010).

The goal of the present study is to use cadaveric gait simulation to quantify the effect of transverse plane rotational misalignment of ankle arthroplasty on foot bone kinematics and plantar pressure distribution. We hypothesize that either direction of misalignment will decrease range of motion at the tibiotalar joint, but minimally affect distal foot joint kinematics. Additionally, internal and external rotational misalignment of the TAA is hypothesized to increase the plantar pressure distribution on the medial and lateral sides of the foot, respectively.

3.3 Methods

Seven fresh frozen cadaveric right foot specimens (donor age 63.9 ± 8.4 years, donor weight 71.3 ± 10.6 kg, 6 male/1 female) were obtained for this study from LifeLegacy Foundation (Tuscon, AZ). Specimens were radiographically verified to have no anatomic deformities by an orthopaedic surgeon, using anteroposterior and lateral loaded fluoroscope images of each foot.

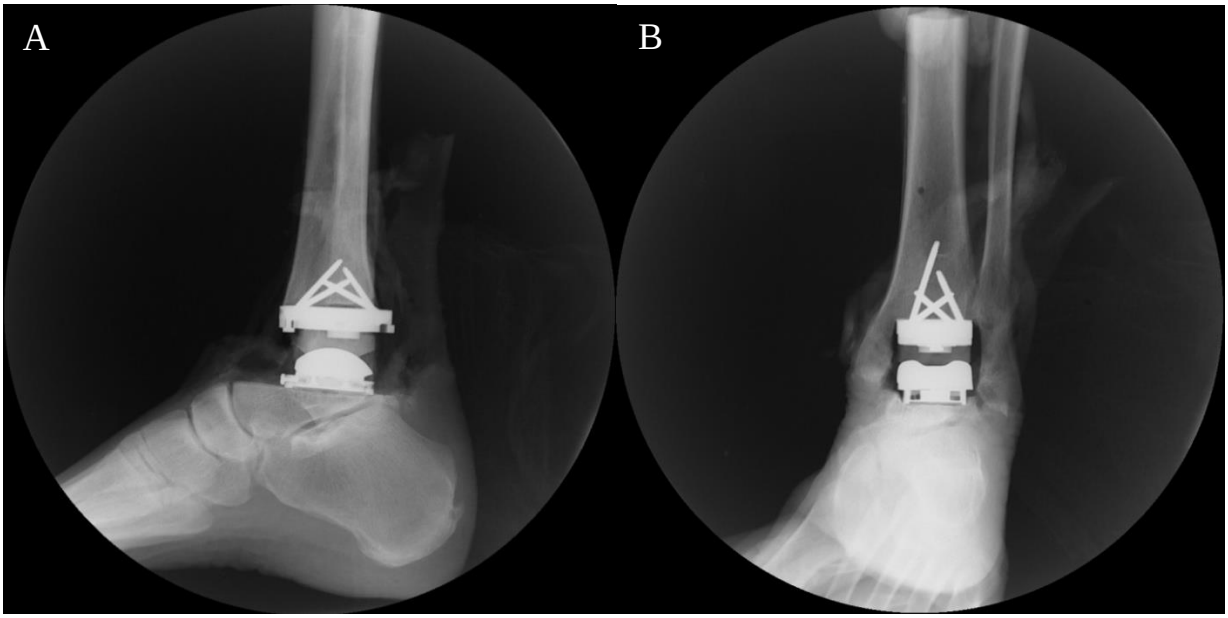

Figure 3.1:A) Lateral and B) mortise radiographs of Salto Talaris arthroplasty implanted in a specimen with the custom misalignment fixture.

Ankle arthroplasty surgery was first performed on the specimens using a custom modified version of the Salto Talaris Total Ankle Prosthesis (Integra LifeSciences Corp., Plainsboro, NJ) (Rush and Todd 2013). A custom fixture was designed to implant the arthroplasty into the specimen in the normal alignment for the surgery, but to allow for specific rotational misalignments to be applied to both the tibial and talar components to examine the effect of transverse plane rotational misalignment of the arthroplasty (Appendix D). The trial components for both the talar implant and tibial bearing were used for this study. A custom two-plate tibial component was used instead of the standard Salto Talaris tibial component. This component allowed the plates to be rotated relative to each other, then to be locked together, to allow for axial rotational misalignments to be applied to the tibial bearing. The trial talar component is identical to the standard implant, with the exception of a non-porous finish on the inferior side. A custom misalignment fixture was designed to interface rigidly with the triplanar inferior side of the talar component and provide rotational misalignment between the implant

connection piece and the distal fixation plate. Notably, the articular surface of the trial tibial component fully constrained the talar component, in contrast with the standard implanted tibial component, which has a less constrained surface congruency in transverse plane rotation and anteroposterior and mediolateral translation when articulating with the talar component.

The standard surgical protocol was followed for alignment of the tibial cut for the Salto Talaris, with the exception of a custom designed cutting guide was used to allow the talus to be cut at the same angle as the tibia. The bone was removed from the tibia and talus such that the superoinferior position of the native tibiotalar joint was maintained. The talar component fixture was adhered to the remaining talus bone using polymethylmethacrylate (PMMA) (LangDental Mfg. Co., Wheeling, IL). The top plate of the custom tibial component was then fixed to the tibia bone using four 3.5 mm bone screws, directed obliquely (Figures 3.1A and B). For one specimen, the medial malleolus was fractured during the tibial resection portion of the surgery, but was reduced and set anatomically with two bone screws, and reinforced with PMMA before testing. The arthroplasty was tested in neutral alignment, as well as five, ten, and fifteen degrees of internal (15IR, 10IR, 5IR) and external (15ER, 10ER, 5ER) rotational misalignments (Figures 3.2, 3.3).

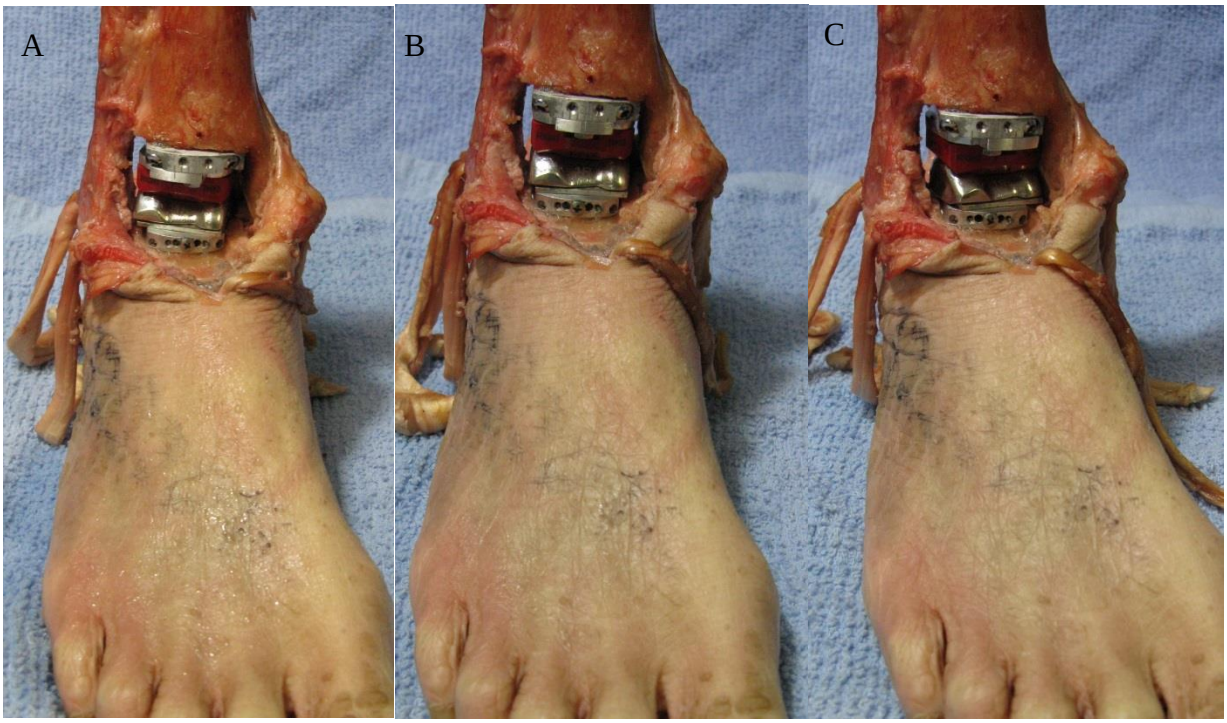

Figure 3.2: The Salto Talaris total ankle replacement implanted in a specimen using the custom misalignment fixture, in alignments of A) 15º external rotation, B) neutral, and C) 15º internal rotation.

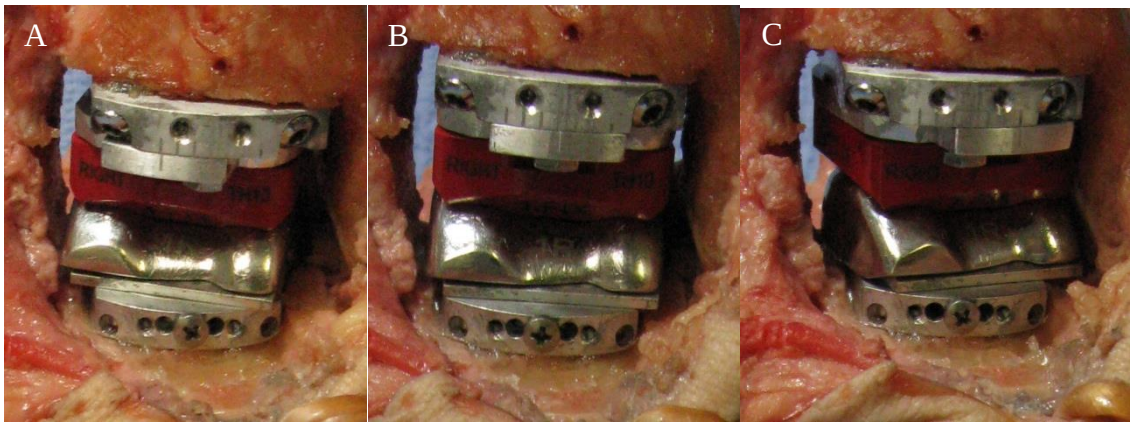

Figure 3.3: The custom designed ankle replacement fixture with the implanted Salto Talaris in a specimen, in alignments of A) 15º external rotation, B) neutral, and C) 15º internal rotation.

Further preparation was performed to each specimen to allow for testing on the gait simulator. The tibia and fibula were transected approximately 15 cm above to the lateral malleolus. The tendons of the following muscles were isolated: tibialis anterior, extensor hallucis longus, extensor digitorum longus, peroneus longus, peroneus brevis, flexor hallucis longus, flexor digitorum longus, tibialis posterior and triceps surae (Achilles tendon). All other soft

tissue proximal to the tibiotalar joint was removed. An 11.1 mm diameter hole was bore into the tibial shaft, and a custom mounting fixture was used to pot the tibia in PMMA, and rigidly connect the tibia to the mounting frame of the gait simulator. To provide for kinematic tracking of the foot bones, screws were placed in seven bones of interest in the foot, in locations that would not impact joint motion. Clusters of four retroreflective motion capture markers were rigidly connected to these screws. Markers were also placed on the dorsal skin of the hallux and on the tibial mounting fixture (Figure 3.4).

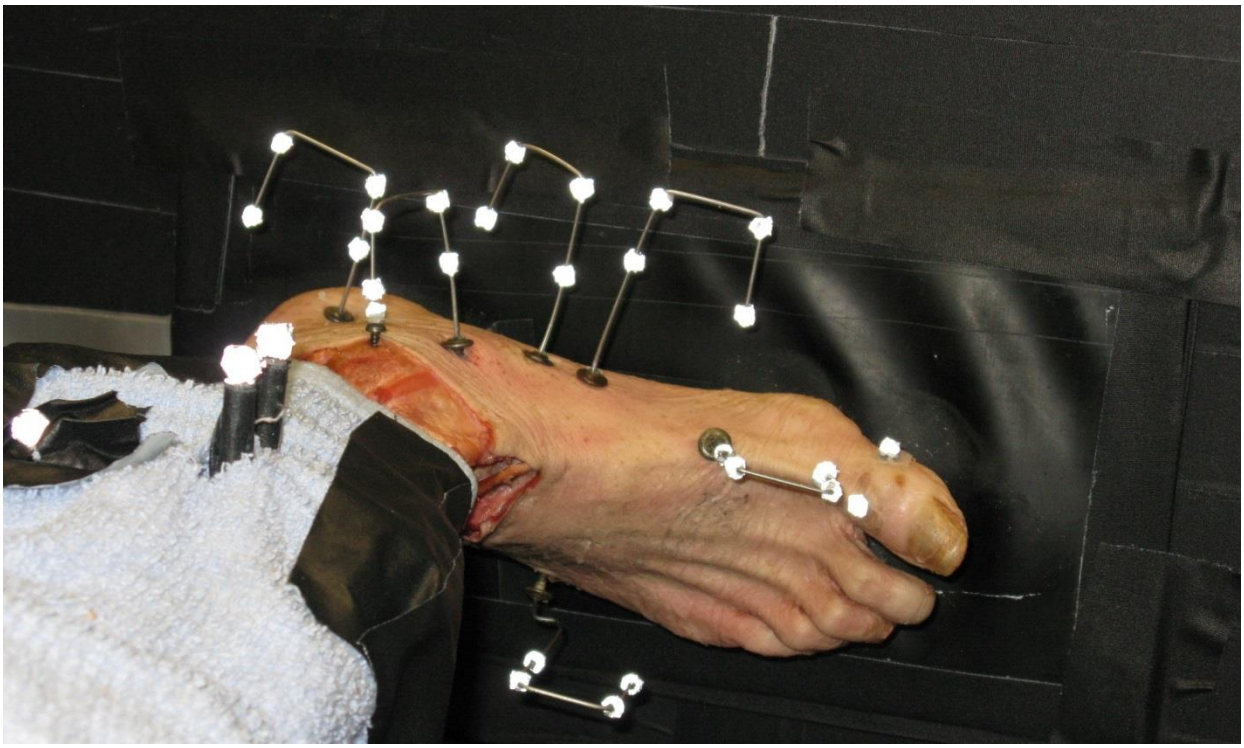

Figure 3.4: A specimen mounted on the RGS, with bone screws and marker clusters visible.

All specimens with the TAA surgery were tested using the robotic gait simulator (RGS) (Aubin, Whittaker, and Ledoux 2012). The RGS simulates walking for the cadaveric specimen, while measuring foot joint kinematics and plantar pressure. The system consists of a force plate mounted on a six-degree-of freedom robot (Mikrolar, Inc., Hampton, NH) that contacts the foot

in the same way the foot contacts the ground in normal gait (Figure 3.5). Actuators are connected to nine extrinsic muscle tendons, to dynamically simulate muscle forces. Metal clamps were used to connect to the tibialis anterior and Achilles tendons, with a liquid nitrogen freeze clamp used on the Achilles tendon. Each of the other isolated tendons was connected using a nylon string tied around a small nut and bolt through the tendon. Input muscle forces were estimated from muscle activation and physiologic cross sectional area of each of the nine muscles individually (Fukunaga et al. 1996; Wickiewicz et al. 1983; Zhou et al. 1995). The tibia-to-ground kinematics replicated by the RGS, and the target ground reaction forces the system is attempts to match, were both experimentally determined from gait analysis data from six patients, all of whom were one year postoperative from TAA surgery with the Salto Talaris. The target ground reaction force was matched by the RGS using a fuzzy logic control scheme, which controls the tibialis anterior and Achilles tendon forces in real time, and iteratively made small specific changes to the tibia to ground input kinematics. The gait simulations were performed with the target ground reaction force scaled to 50% of the donor's body weight for each specimen. To precondition tissue, three consecutive gait simulations were performed before data was collected on the fourth. Three trials of data were taken for each condition. The seven misalignment conditions were tested in randomized order, throughout the experiment.

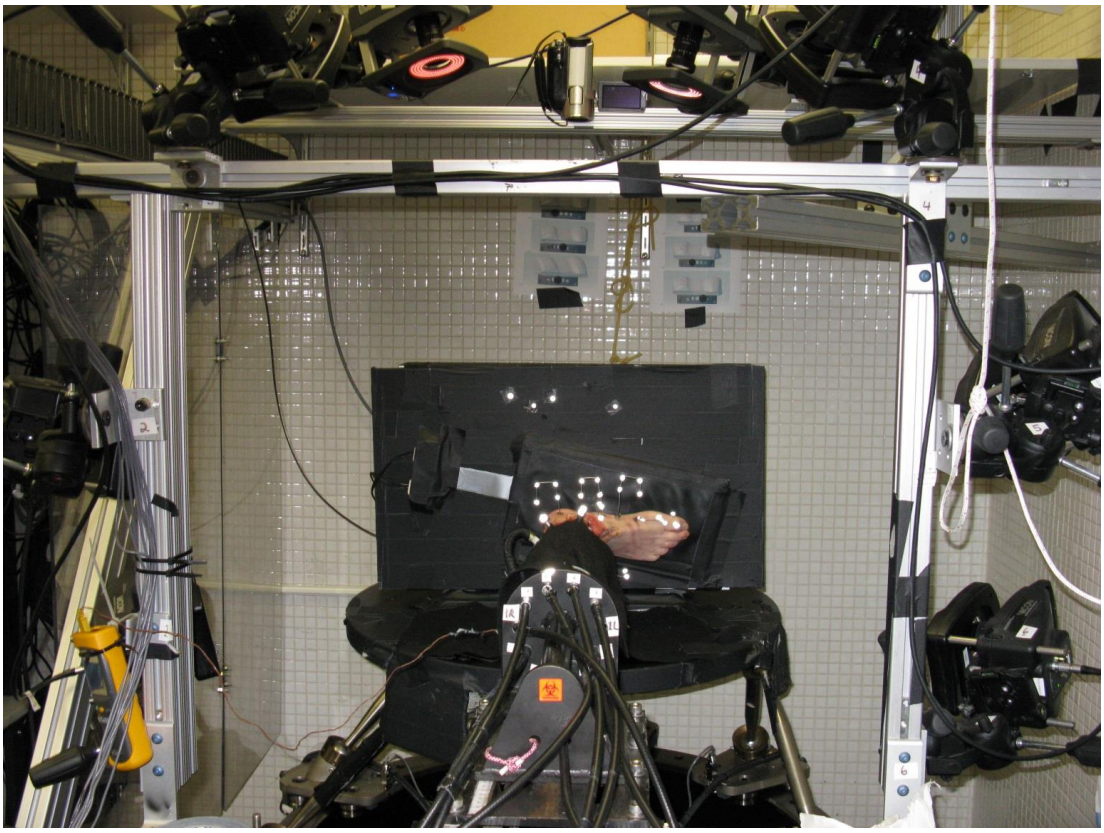

Figure 3.5: The robotic gait simulator.

Joint kinematics were collected to measure the changes in foot joint motion due to arthroplasty misalignment. An eight-camera motion capture system (Vicon Motion Systems, Denver, CO) was used to track joint kinematics. The marker clusters connected to screws in the foot bones were tracked throughout the simulation. Connecting the marker clusters directly to the bone improved accuracy of kinematic measurements by eliminating soft tissue motion from the measurement. Marker data was filtered using a Woltring filtering routine with a predicted mean square error of 10. Anatomical landmarks were created digitally on the tibia, talus, calcaneus, navicular, cuboid, and cuneiforms to establish anatomically-relevant coordinate systems. These landmarks were used in a custom nine-segment foot model (Whittaker, Aubin, and Ledoux 2011), which was used to determine joint angles for the following joints: tibiotalar, talocalcaneal, talonavicular, calcaneocuboid, naviculocuneiform, cuneiform-first metatarsal, cuboid-fifth

metatarsal, first metatarsophalangeal and relationship between the talus-first metatarsal. For each cardinal plane of each joint angle, the range of motion and joint angle at each 1% stance phase was analyzed.

Plantar pressure data was measured using a pliance (novel electronics inc., St. Paul, MN) pressure mat. The pressure mat was placed in series with the force plate such that the specimen contacted the mat during the simulation. Pressure measurements were thresholded at 40 kPa. After data collection, the pressure data was aligned to a superoinferior radiograph using Matlab (Mathworks, Natick, MA) to establish an anatomically meaningful coordinate system, whose anteroposterior axis was directed from the most posterior point on the calcaneus through the second ray (De Cock et al. 2008). Mediolateral deviation in center was pressure was calculated with respect to this foot centerline axis. The sensor mat was then partitioned into ten anatomical regions (hallux, lesser toes, first metatarsal, second metatarsal, third metatarsal, fourth metatarsal, fifth metatarsal, medial midfoot, lateral midfoot, and heel) based on the radiograph, and peak pressure was determined for each region.

Linear mixed effects regression was used to determine if the (dependent) outcome variable differed by condition type (modeled as the independent fixed effect with four dummy variables). Specimen and specimen condition interaction were modeled as random effects. First, an omnibus test for association between outcome variable and condition was carried out. If significant, pairwise comparisons were carried out comparing all 4 misalignment conditions to the neutral condition using simultaneous inference. Results for pairwise differences are presented with 95 percent confidence intervals. All analyses were performed in R 3.2.5 (Team 2013) with the lme4 (Bates et al. 2015) package to carry out the linear mixed effects regression and the

multcomp package (Hothorn, Bretz, and Westfall 2008) to estimate the 95% confidence intervals.

3.4 Results

The quality of the gait simulation was determined by the accuracy of matching the *in vivo* ground reaction forces and tibia-to-ground kinematics. The *in vivo* tibia-to-ground kinematics were matched well by the robot (Figure 3.6). The target vertical ground reaction force, which was controlled by the tendon force and iterative trajectory controller systems, was matched to 5.1% bodyweight RMS error. The mediolateral and anteroposterior ground reaction forces were not controlled by the RGS, but were matched to 3.9% and 13.0% bodyweight RMS error, respectively (Figure 3.7).

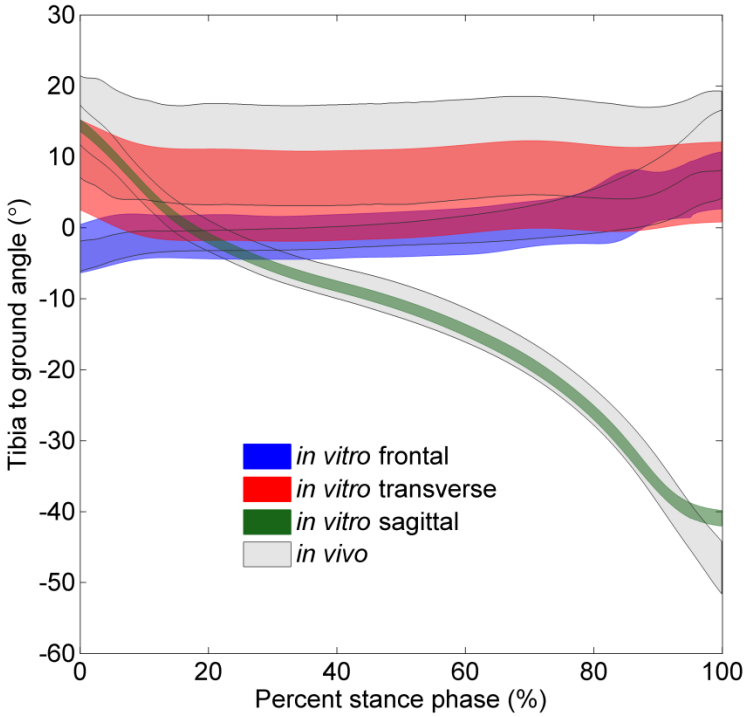

Figure 3.6: Standard deviation of tibia-to-ground kinematics comparing *in vivo* targets and *in vitro* simulation results, for frontal, transverse, and sagittal plane angles.

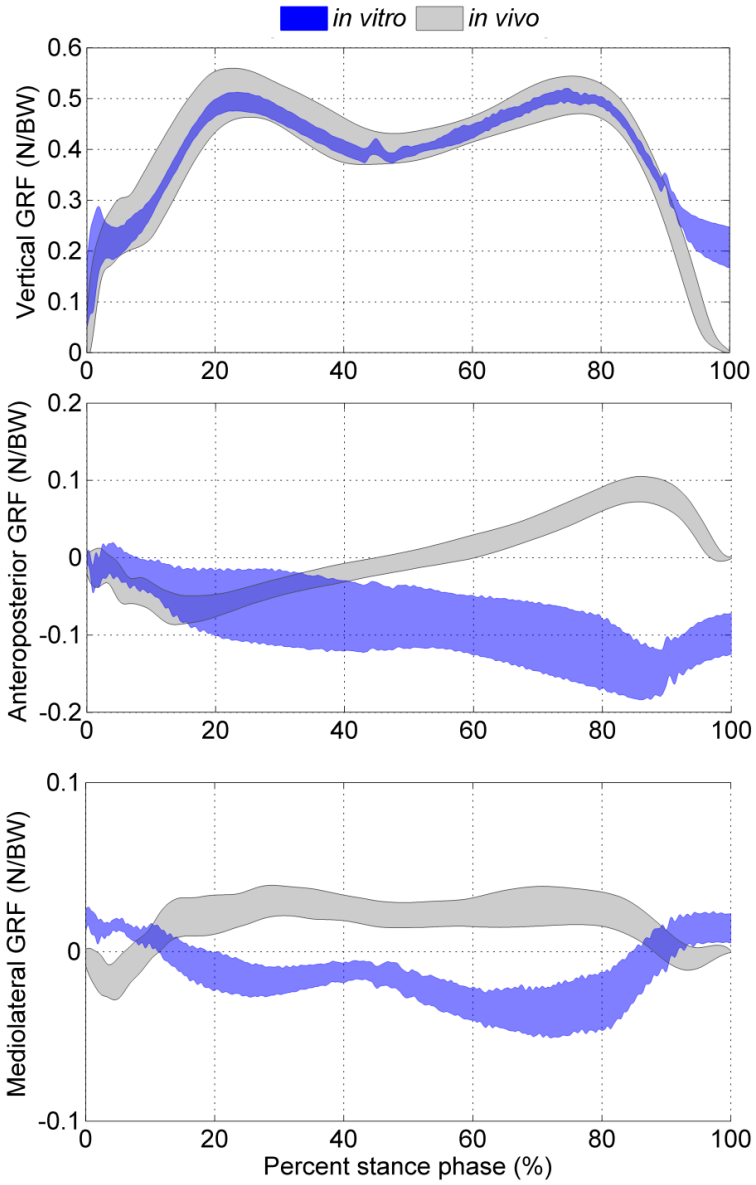

Figure 3.7: The three planes of ground reaction force data (GRF), comparing the target ground reaction forces (*in vivo*) and results of the study (*in vitro*).

The range of motion of several foot joints was affected by TAA misalignment. Compared to the neutrally aligned TAA, in the hindfoot range of motion was significantly increased for the frontal plane of the tibiotalar joint for the 15IR misalignment (1.6 degrees, 70% increase, $p<0.001$) and 10IR misalignment (1.0 degrees, 43% increase, $p=0.0132$), significantly decreased in the sagittal plane of the talocalcaneal joint for the 10IR misalignment (-0.4 degrees, 8%

decrease, p=0.026), significantly increased in the frontal plane of the calcaneocuboid joint for the 15ER misalignment (0.8 degrees, 20% increase, p = 0.047), and significantly increase in the transverse plane (1.9 degrees, 23% increase, p = 0.047), decreased for the sagittal plane of the calcaneocuboid joint for the 10IR misalignment (-1.3 degrees, 15% decrease, p = 0.018) (Table 3.1).

In the forefoot, the range of motion was significantly increased in the transverse plane of the cuneiform-first metatarsal joint for the 15ER misalignment (0.8 degrees, 15% increase, p = 0.0021), significantly decreased in the sagittal plane of the cuneiform-first metatarsal joint for the 15IR misalignment (-1.2 degrees, 17% decrease, p = 0.0016), and significantly decreased in the sagittal plane for the talus-first metatarsal relationship for the 15ER (-0.9 degrees, 5% decrease, p < 0.001), 10ER (-0.9º, 5% decrease, p < 0.001), and 5ER misalignments (-1.2 degrees, 6% decrease, p < 0.001) (Table 3.2).

Table 3.1. Hindfoot joints mean range of motion (ROM) ± standard error for neutrally aligned TAA, changes in range of motion for each misaligned condition with 95% confidence intervals (CI), and omnibus p-value between all conditions.

Joint Angle	Mean ROM (º)	Difference in ROM between misaligned and neutral conditions (º)						p
	N ± SE	15ER-N (CI)	10ER-N (CI)	5ER-N (CI)	5IR-N (CI)	10IR-N (CI)	15IR-N (CI)	
Tibiotalar Frontal	2.3 ± 0.6	0.2 (-2.1, 2.5)	0.1 (-1.5, 1.6)	0 (-0.7, 0.8)	0.7 (-0.2, 1.6)	1.0* (0.1, 2)	1.6** (0.7, 2.6)	0.002
Tibiotalar Transverse	3.3 ± 0.5	0.5 (-0.4, 1.5)	0.3 (-0.5, 1.2)	0.2 (-0.8, 1.2)	-0.1 (-0.9, 0.6)	-0.2 (-1, 0.6)	0.3 (-1.4, 1.9)	0.598
Tibiotalar Sagittal	12.8 ± 0.5	1.4 (-0.1, 2.8)	0.9 (-0.5, 2.4)	0.5 (-0.6, 1.7)	-0.2 (-0.9, 0.6)	-0.2 (-1.3, 1)	-0.4 (-1.5, 0.7)	0.089
Talonavicular Frontal	9.6 ± 0.9	0 (-1.1, 1.1)	0.0 (-1.1, 1)	0.2 (-1, 1.3)	0.0 (-1, 1)	-0.2 (-0.9, 0.5)	0.5 (-0.5, 1.4)	0.860
Talonavicular Transverse	9.1 ± 2.1	0.4 (-1.0, 1.7)	0.1 (-1.1, 1.3)	-0.2 (-1, 0.7)	-0.3 (-0.8, 0.2)	0 (-0.7, 0.6)	0.2 (-0.8, 1.2)	0.688
Talonavicular Sagittal	6.3 ± 1.7	-0.1 (-0.7, 0.5)	-0.2 (-0.8, 0.5)	-0.1 (-0.6, 0.4)	-0.6 (-1.5, 0.3)	-0.6 (-1.2, 0.1)	0.1 (-0.4, 0.6)	0.221
Talocalcaneal Frontal	4.7 ± 0.6	0 (-1, 1.1)	0.2 (-0.6, 0.9)	0.2 (-0.4, 0.9)	0.3 (-0.8, 1.4)	-0.1 (-0.7, 0.6)	0.1 (-1, 1.1)	0.917
Talocalcaneal Transverse	4.9 ± 0.6	-0.1 (-0.9, 0.8)	-0.1 (-0.9, 0.7)	-0.2 (-1.1, 0.7)	0 (-0.6, 0.6)	-0.4* (-0.7, 0)	0 (-0.7, 0.6)	0.360
Talocalcaneal Sagittal	4.6 ± 0.7	-0.1 (-0.7, 0.5)	0.0 (-0.4, 0.3)	0.0 (-0.6, 0.6)	0.5 (0.0, 1.0)	-0.1 (-0.8, 0.6)	0.3 (-0.1, 0.6)	0.164
Naviculocuneiform Frontal	5.9 ± 0.4	0.3 (-0.2, 0.8)	-0.1 (-0.7, 0.4)	0.5 (-0.7, 1.7)	0.4 (-0.9, 1.7)	-0.1 (-0.8, 0.5)	-0.2 (-1.3, 0.9)	0.361
Naviculocuneiform Transverse	3.0 ± 0.2	-0.4 (-1.3, 0.5)	-0.4 (-1.3, 0.5)	-0.3 (-1, 0.4)	0.1 (-0.9, 1.1)	-0.3 (-1, 0.4)	0.1 (-0.4, 0.5)	0.424
Naviculocuneiform Sagittal	10.6 ± 1.2	0.2 (-1, 1.3)	0.1 (-1, 1.3)	0.1 (-1, 1.2)	1.1 (-0.1, 2.2)	0.5 (-1, 2)	0.3 (-1, 1.6)	0.395
Calcaneocuboid Frontal	3.9 ± 0.4	0.8** (0.3, 1.3)	0.2 (-0.3, 0.6)	0.6 (-0.4, 1.5)	-0.1 (-0.9, 0.6)	0.0 (-0.7, 0.6)	-0.4 (-0.9, 0)	<0.001
Calcaneocuboid Transverse	8.2 ± 1.1	1.9* (0 , 3.9)	-0.1 (-1.5, 1.4)	3.1 (-1.5, 7.8)	0.2 (-1.9, 2.4)	-0.3 (-1.9, 1.2)	-0.3 (-2.3, 1.6)	0.100
Calcaneocuboid Sagittal	8.7 ± 1.1	0.5 (-1.1, 2)	-0.5 (-1.7, 0.6)	1.6 (-1.5, 4.8)	-0.2 (-1.9, 1.4)	-1.3* (-2.4, -0.1)	-0.6 (-1.5, 0.3)	0.034

*****Pairwise comparisons where $p < 0.05$, ** Pairwise comparisons where $p < 0.005$.
15ER-15° external rotational misalignment 10ER-10° external rotational misalignment, 5ER-5° external rotational misalignment, N-neutrally aligned surgery, 5IR-5° internal rotational misalignment, 10IR-10° internal rotational misalignment, 15IR-15° internal rotational misalignment

Table 3.2. Forefoot joints mean range of motion (ROM) ± standard error for neutrally aligned TAA, changes in range of motion for each misaligned condition with 95% confidence intervals (CI), and omnibus p-value between all conditions.

Joint Angle	Mean ROM (degrees)	Difference in ROM between misaligned and neutral conditions (degrees)						p
	N ± SE	15ER-N (CI)	10ER-N (CI)	5ER-N (CI)	5IR-N (CI)	10IR-N (CI)	15IR-N (CI)	
F-Cuneiform-First Metatarsal	6.9 ± 1.4	-0.1 (-0.6, 0.3)	0 (-0.6, 0.6)	-0.1 (-0.8, 0.6)	0.5 (-0.4, 1.3)	0.3 (-0.1, 0.6)	0.2 (-0.8, 1.1)	0.268
T-Cuneiform-First Metatarsal	5.4 ± 1	0.8** (0.2 , 1.4)	0.4 (0, 0.8)	0.3 (-0.5, 1.1)	0.6 (-0.1, 1.3)	0.5 (-0.5, 1.4)	-0.2 (-1.7, 1.3)	0.007
S-Cuneiform-First Metatarsal	6.8 ± 0.6	-0.4 (-1.5, 0.8)	-0.7 (-2.1, 0.6)	-0.3 (-0.9, 0.3)	-0.6 (-1.7, 0.6)	-1.0 (-2.1, 0.1)	-1.2** (-2, -0.3)	0.007
F-Talus-First Metatarsal	7.2 ± 0.9	-0.1 (-2.2 , 2)	-0.9 (-2.8, 1)	-0.6 (-2.3, 1.2)	-0.2 (-2, 1.6)	-0.3 (-1.6, 0.9)	-0.3 (-1.6, 1.1)	0.749
T-Talus-First Metatarsal	11.2 ± 0.7	0.7 (-0.6, 2)	0.0 (-0.9, 0.9)	-0.2 (-0.8, 0.5)	0.6 (-0.5, 1.7)	-0.1 (-0.9, 0.8)	-0.3 (-1.5, 0.9)	0.536
S-Talus-First Metatarsal	20.0 ± 1.9	-0.9** (-1.4, -0.5)	-0.9** (-1.5, -0.4)	-1.2** (-2, -0.4)	-0.2 (-1.1, 0.6)	-0.5 (-1.6, 0.6)	-0.3 (-1.3, 0.7)	<0.001
F-Cuboid-Fifth Metatarsal	9.1 ± 0.9	0.4 (-0.3, 1.1)	-0.1 (-1.4, 1.2)	0.0 (-0.9, 1)	-0.3 (-1.3, 0.8)	-0.6 (-2.3, 1.1)	-1.0 (-2.8, 0.8)	0.315
T-Cuboid-Fifth Metatarsal	14.2 ± 2.2	-1.4 (-4.3, 1.5)	-1.6 (-3.5, 0.4)	-0.9 (-4.7, 2.9)	-2 (-4.2, 0.1)	0.1 (-2.4, 2.6)	-0.8 (-3.1, 1.6)	0.115
S-Cuboid-Fifth Metatarsal	18 ± 3	-1.3 (-5. , 2.5)	-0.5 (-3.2, 2.3)	-1.9 (-5.9, 2.2)	-1.5 (-4.4, 1.4)	0.7 (-1.2, 2.6)	0.7 (-1.4, 2.7)	0.357
F-First Metatarsophalangeal	17.8 ± 2.6	1.6 (-0.5, 3.7)	0.1 (-2.2, 2.4)	-0.2 (-1.5, 1.1)	0.7 (-2.3, 3.6)	0.3 (-2.4, 2.9)	0.3 (-2.5, 3.2)	0.585
T-First Metatarsophalangeal	20 ± 3.0	-0.6 (-2, 0.8)	-1.0 (-2.9, 0.8)	-2.1 (-6.2, 1.9)	0.2 (-2.6, 3)	-0.9 (-3.2, 1.4)	-1.4 (-3.8, 1)	0.214
S-First Metatarsophalangeal	45.7 ± 3.1	-1.0 (-3.6, 1.5)	0.2 (-1.1, 1.6)	-1.1 (-3.1, 1)	1.4 (-2.7, 5.5)	0.7 (-2.3, 3.7)	1.6 (-1.7, 4.9)	0.352

F-Frontal, T-Transverse, S-Sagittal

*****Pairwise comparisons where $p < 0.05$, ** Pairwise comparisons where $p < 0.005$.

15ER-15° external rotational misalignment 10ER-10° external rotational misalignment, 5ER-5° external rotational misalignment, N-neutrally aligned surgery, 5IR-5° internal rotational misalignment, 10IR-10° internal rotational misalignment, 15IR-15° internal rotational misalignment

Plantar pressure distribution was minimally affected by TAA misalignment. No significant changes were found in peak plantar pressure measurement over stance phase for any of the ten regions of the foot (Table 3.3). Additionally, no significant changes were found in the mediolateral deviation in the center of pressure (Table 3.4).

Table 3.3. Peak pressure ± standard error (SE) measured in each region of the foot for the neutrally TAA, changes in maximum pressure measurement for each misaligned condition with 95% confidence interval (CI), and omnibus p-value between all conditions.

Region	Mean peak pressure measurement (kPa)	Difference in peak pressure between misaligned and neutral conditions (kPa)						p
	N ± SE	15ER-N (CI)	10ER-N (CI)	5ER-N (CI)	5IR-N (CI)	10IR-N (CI)	15IR-N (CI)	
Great Toe	257.1 ± 39	11.8 (-45.4, 69)	-1.8 (-60.6, 57)	2.7 (-40.2, 45.7)	-27.3 (-71.4, 16.9)	-26.7 (-64, 10.7)	-21.4 (-67.8, 25)	0.26
Lesser Toes	181.8 ± 20.1	-10.1 (-26.4 , 6.1)	-14.3 (-37.6, 9.1)	-12.1 (-36, 11.7)	-9.3 (-36, 17.5)	5.6 (-35.6, 46.8)	-1.2 (-45.8, 43.4)	0.42
Met 1	263.6 ± 84.7	6 (-18.4, 30.3)	-1.2 (-25.6, 23.3)	16.8 (-22.3, 55.9)	-10.6 (-61.8, 40.6)	-15 (-46, 16)	1.8 (-23.8, 27.4)	0.68
Met 2	243.7 ± 51.4	-30.7 (-95.7, 34.3)	-23.7 (-69, 21.6)	-31.3 (-91.7, 29)	-10.2 (-34.5, 14)	-6.5 (-23.7, 10.6)	-27.9 (-93.1, 37.4)	0.22
Met 3	197.6 ± 16.4	-3.5 (-42.8, 35.9)	1.0 (-27.1, 29)	-7.9 (-28.6, 12.9)	-10 (-35.7, 15.7)	-4.5 (-17.4, 8.4)	6.3 (-11.9, 24.5)	0.61
Met 4	173.8 ± 40	18.9 (-60.9, 98.8)	19.5 (-27.6, 66.6)	26.5 (-41.1, 94.2)	5.5 (-43.4, 54.4)	20 (-56, 96)	22.1 (-30.6, 74.9)	0.60
Met 5	96.5 ± 11.6	-6.4 (-42.1, 29.3)	-8.1 (-34.5, 18.3)	-0.8 (-35.8, 34.1)	-5.4 (-34.4, 23.7)	-3.6 (-24.8, 17.6)	-0.1 (-23.5, 23.3)	0.97
Lateral Midfoot	43.7 ± 11.9	-0.2 (-4.2 , 3.7)	1.1 (-4, 6.2)	-0.4 (-4.3, 3.6)	-5 (-25, 15)	-3.8 (-24.1, 16.5)	-1.9 (-16.7, 12.9)	0.96
Heel	233.8 ± 68	5.1 (-14.2, 24.4)	1.8 (-17, 20.5)	-1.2 (-34.2, 31.8)	3 (-11.9, 17.8)	-2.7 (-10.1, 4.7)	-8.9 (-25.6, 7.8)	0.65

*****Pairwise comparisons where $p < 0.05$, ** Pairwise comparisons where $p < 0.005$.
15ER-15° external rotational misalignment 10ER-10° external rotational misalignment, 5ER-5° external rotational misalignment, N-neutrally aligned surgery, 5IR-5° internal rotational misalignment, 10IR-10° internal rotational misalignment, 15IR-15° internal rotational

Table 3.4. Mediolateral (ML) Center of Pressure (COP) at four instances during stance phase ± standard error (SE) for the neutrally alignment TAA, changes in COP for each misaligned condition with 95% confidence interval (CI), and omnibus p-value between all conditions.

Instance of stance phase	Mean ML COP (mm) N± SE	Difference in ML COP between misaligned and neutral conditions (mm) 15ER-N (CI)	10ER-N (CI)	5ER-N (CI)	5IR-N (CI)	10IR-N (CI)	15IR-N (CI)	p
25%	-0.26 ± 0.8	0.48 (-1.9, 2.9)	0.43 (-1.7, 2.6)	0.41 (-0.9, 1.7)	0.63 (-1.7, 2.9)	0.5 (-0.8, 1.8)	1.37 (-1.5, 4.2)	0.80
50%	4.08 ± 1.4	0.14 (-2.6, 2.9)	0.35 (-2.8, 3.5)	-0.72 (-3.4, 2)	-0.48 (-5.1, 4.1)	0.54 (-1.8, 2.9)	1.06 (-3.7, 5.8)	0.95
75%	0.16 ± 1.5	-0.04 (-2, 1.9)	-0.05 (-2.6, 2.5)	-0.1 (-2.2, 2)	-0.7 (-4.1, 2.7)	0.47 (-0.6, 1.5)	0.92 (-2.2, 4)	0.86
90%	-8.39 ± 1.5	-0.49 (-2.2, 1.2)	-0.44 (-3.5, 2.6)	-1.23 (-4.8, 2.4)	-1.46 (-6.2, 3.3)	0.07 (-2.6, 2.8)	1.0 (-4.3, 6.3)	0.86

*****Pairwise comparisons where $p < 0.05$, ** Pairwise comparisons where $p < 0.005$.
15ER-15° external rotational misalignment 10ER-10° external rotational misalignment, 5ER-5° external rotational misalignment, N-neutrally aligned surgery, 5IR-5° internal rotational misalignment, 10IR-10° internal rotational misalignment, 15IR-15° internal rotational

3.5 Discussion

TAA surgery was performed in cadaveric specimens using a custom surgical technique and fixture system to allow for prescribed rotationally misalignments of the Salto Talaris total ankle system to be applied in the transverse plane; gait was then simulated for each misalignment. Misalignment of the TAA significantly increased tibiotalar joint frontal plane range of motion due to internal rotational misalignment. Significant changes in range of motion due to misalignment were also found in the talocalcaneal, calcaneocuboid, and cuneiform-first metatarsal joints, and talus-first metatarsal relationship. Plantar pressure distribution was not changed due to misalignment of the TAA. This could be partially attributed to misalignment of both implants together, and potential changes in loading at the tibiotalar joint due to misalignment not significantly changing the way the plantar surface of the foot is loaded.

Previous studies on TAA misalignment have focused on the implant kinematics and stress. Fukuda et al. used a finite element model to show increased pressure and deceased contact area due to transverse plane misalignments of TAA (Fukuda et al. 2010). As that study did not examine joint kinematics, and the current study did not examine pressure at the implant interface, few direct comparisons can be made. Implantation misalignment of TAA in the anteroposterior direction did show a decrease in ankle joint range of motion (Tochigi et al. 2005). A different ankle system was used in this study, and the loading conditions were less dynamic, but the current study agrees that misalignment does change the kinematics of the ankle joint. Misalignment of TAA has been associated with increased polyethylene wear, both in patients (Buechel, Buechel, and Pappas 2003) and in cadaveric studies where implant stress was measured directly (Espinosa et al. 2010). While the current study did not measure pressure between the TAA components directly, the change in tibiotalar range of motion could change the loading of the implants. Adding measurement of inter-component pressure in a future study could give insight into how the changes in range of motion due to misalignment would affect implant wear. The results of the present study indicate similar average values of range of motion in the neutrally alignment tibiotalar joint to a study that dynamically tracked implant position using fluoroscopy (Leszko et al. 2008). Transverse plane motion was observed to be greater in this *in vivo* fluoroscopy study, but this could be attributed to the implant evaluated, the Salto mobile-bearing implant, which is less constrained in the transverse plane than the fixed-bearing Salto Talaris.

This study did include some limitations. The dorsal talonavicular ligament was cut when bone was removed from the talus on four of the seven specimens. The talonavicular joint kinematics seemed to show little difference in specimens with this ligament damage compared to

those with the ligament intact, suggesting that the results of the talonavicular joint kinematics are still valid. The use of the trial tibial bearing did further constrain tibiotalar joint motion compared to the standard implant. The standard tibial bearing allows more freedom of motion in the transverse plane for talar component (Morris et al. 2015), thus misalignment could have less of an effect with the standard tibial bearing. Specimens were tested at 50% specimen body-weight to prevent damage to the specimen, which limits the conclusions that can be drawn about full body-weight testing. Being a cadaveric study, the sample size also limited statistical power.

The present study provides the framework for examination of TAA misalignment using dynamic cadaveric loading. Three additional specimens have yet to be tested in this study, thus the data presented are preliminary. Anteroposterior translational and frontal plane rotational misalignments will also be evaluated on the RGS in separate studies. Further examination into the changes in joint stresses both at the implant surfaces, and adjacent foot joints, could better measure the biomechanical changes in these joints due to TAA misalignment.

Chapter 4. Conclusion

4.1 Summary

Ankle arthrodesis and arthroplasty are common surgeries for end stage ankle arthritis. Misalignment occurs in both of these surgeries (Hintermann et al. 2009; Preyssas et al. 2012) and can lead to pain, functional limitations, and other negative patient outcomes. The goal of this thesis was to develop a method to simulate misalignments of these surgeries in cadaveric specimens, and determine the biomechanical effect of misalignment in gait simulation. These studies utilizing the robotic gait simulator (RGS) to dynamically load these specimen, and showed minor changes due to transverse plane rotational misalignment for the arthrodesis, but more major changes for misalignment of the arthroplasty.

Arthrodesis surgery was simulated using a custom fixture to fuse the talus and tibia, and allow for testing of multiple rotational misalignments. Misalignments had minimal effect on the parameters measured in ankle arthrodesis. Changes in joint angles over stance phase suggested abnormal loading could occur in the naviculocuneiform and cuboid-fifth metatarsal joints. Additionally, range of motion and plantar pressure distribution were predominantly unaffected by these misalignments. These data suggest that transverse plane misalignment of ankle arthrodesis does not change range of motion at adjacent joints. Further examination of other relevant parameters, such as stresses in adjacent joints, could better quantify the biomechanical reason why patients have poorer outcomes due to misalignment of ankle arthrodesis compared to the neutrally aligned surgery (Coester et al. 2001).

A custom surgical technique and fixture system was developed for total ankle arthroplasty (TAA) as well. Transverse plane rotational misalignment of TAA significantly

affected foot joint kinematics. Frontal plane range of motion of the tibiotalar joint was increased for internal rotational misalignments of the TAA, which could change the loading of the implant. Significant changes in range of motion due to misalignment were also found in the talocalcaneal, calcaneocuboid, and cuneiform-first metatarsal joints, and talus-first metatarsal relationship. Similar to the arthrodesis misalignment study, plantar pressure parameters were not significantly affected by misalignment. Further analysis of three additional specimens yet to be tested will add power to the study, and additional findings may become apparent.

Based on the results of these studies, ankle arthrodesis surgery is less sensitive than TAA to changes in foot joint range of motion due to transverse plane misalignment. However, plantar pressure distribution was minimally effected by misalignment for either surgery. Comparisons between the studies are challenging though, due to the difference in loading (25% for the arthrodesis study vs. 50% for the arthroplasty study). Further analysis of the TAA study will allow for comparison of the percent stance phase joint angles between the study.

4.2 Future Work

The techniques developed for this thesis have been applied to evaluate other directions of misalignment in ankle arthrodesis and arthroplasty. Examinations of anteroposterior translational (Imsdahl et al.) and coronal plane rotational misalignment (Wright et al.) of ankle arthrodesis were tested similarly using the RGS. Similarly, a study on anteroposterior misalignment of ankle arthroplasty (McKearney et al.) is underway, and a similar study examining coronal plane rotational misalignment of ankle arthroplasty will be performed on the RGS soon. Completion of these studies will allow for conclusions to be drawn of which misalignments of these surgeries have the largest impact on the foot biomechanically.

Cadaveric gait simulation could be utilized to further quantify the biomechanical changes to the foot and ankle caused by ankle arthrodesis and arthroplasty. A paired study could provide insight into the direct comparison into the biomechanical changes the foot undergoes after each surgery. In such a study, both specimens would first be tested in gait simulation with the native (unaltered) ankle, and then one side would receive ankle arthroplasty and the other arthrodesis, and be tested again. This could potentially help clinicians in their decision for which end stage ankle arthritis surgery to perform on patients. This study idea could be utilized to evaluate the effect of different ankle replacement systems on foot joint kinematics as well. Determining a way to measure joint stress in cadaveric gait simulation would further improve the clinical applicability of this research. Continuing to utilize the RGS as a tool to evaluate foot ankle ankle orthopaedic surgeries can provide clinicians valuable information that cannot be determined *in vivo*.

References

Aubin, P. M., E. C. Whittaker, and W. R. Ledoux. 2012. 'A Robotic Cadaveric Gait Simulator With Fuzzy Logic Vertical Ground Reaction Force Control', *IEEE Transactions on Robotics*, 28: 246-55.

Barg, A., A. Elsner, A. E. Anderson, and B. Hintermann. 2011. 'The effect of three-component total ankle replacement malalignment on clinical outcome: pain relief and functional outcome in 317 consecutive patients', *J Bone Joint Surg Am*, 93: 1969-78.

Barg, A., G. I. Pagenstert, T. Hugle, M. Gloyer, M. Wiewiorski, H. B. Henninger, and V. Valderrabano. 2013. 'Ankle osteoarthritis: etiology, diagnostics, and classification', *Foot Ankle Clin*, 18: 411-26.

Bates, D., M. Maechler, B. Bolker, and S. Walker. 2015. 'Fitting Linear Mixed-Effects Models Using lme4', *Journal of Statistical Software*, 67: 48.

Benjamini, Y., and Y. Hochberg. 1995. 'Controlling the false discovery rate: a practical and powerful approach to multiple testing.', *Journal of the Royal Statistical Society Series B*, 57: 289-300.

Braito, M., D. Dammerer, A. Reinthaler, G. Kaufmann, D. Huber, and R. Biedermann. 2015. 'Effect of Coronal and Sagittal Alignment on Outcome After Mobile-Bearing Total Ankle Replacement', *Foot Ankle Int*, 36: 1029-37.

Buck, P., B. F. Morrey, and E. Y. Chao. 1987. 'The optimum position of arthrodesis of the ankle. A gait study of the knee and ankle', *J Bone Joint Surg Am*, 69: 1052-62.

Buechel, F. F., Sr., F. F. Buechel, Jr., and M. J. Pappas. 2003. 'Ten-year evaluation of cementless Buechel-Pappas meniscal bearing total ankle replacement', *Foot Ankle Int*, 24: 462-72.

Casillas, M. M., and M. Allen. 2004. 'Repair of malunions after ankle arthrodesis', *Clin Podiatr Med Surg*, 21: 371-83, vi.

Cenni, F., A. Leardini, A. Cheli, F. Catani, C. Belvedere, M. Romagnoli, and S. Giannini. 2012. 'Position of the prosthesis components in total ankle replacement and the effect on motion at the replaced joint', *Int Orthop*, 36: 571-8.

Coester, L. M., C. L. Saltzman, J. Leupold, and W. Pontarelli. 2001. 'Long-term results following ankle arthrodesis for post-traumatic arthritis', *J Bone Joint Surg Am*, 83-A: 219-28.

Cushnaghan, J., and P. Dieppe. 1991. 'Study of 500 patients with limb joint osteoarthritis. I. Analysis by age, sex, and distribution of symptomatic joint sites', *Ann Rheum Dis*, 50: 8-13.

De Cock, A., J. Vanrenterghem, T. Willems, E. Witvrouw, and D. De Clercq. 2008. 'The trajectory of the centre of pressure during barefoot running as a potential measure for foot function', *Gait Posture*, 27: 669-75.

Demetriades, L., E. Strauss, and J. Gallina. 1998. 'Osteoarthritis of the ankle', *Clin Orthop Relat Res*: 28-42.

Espinosa, N., M. Walti, P. Favre, and J. G. Snedeker. 2010. 'Misalignment of total ankle components can induce high joint contact pressures', *J Bone Joint Surg Am*, 92: 1179-87.

Flavin, R., S. C. Coleman, S. Tenenbaum, and J. W. Brodsky. 2013. 'Comparison of gait after total ankle arthroplasty and ankle arthrodesis', *Foot Ankle Int*, 34: 1340-8.

Fuentes-Sanz, A., J. Moya-Angeler, F. Lopez-Oliva, and F. Forriol. 2012. 'Clinical outcome and gait analysis of ankle arthrodesis', *Foot Ankle Int*, 33: 819-27.

Fukuda, T., S. L. Haddad, Y. Ren, and L. Q. Zhang. 2010. 'Impact of talar component rotation on contact pressure after total ankle arthroplasty: a cadaveric study', *Foot Ankle Int*, 31: 404-11.

Fukunaga, T., M. Ito, Y. Ichinose, S. Kuno, Y. Kawakami, and S. Fukashiro. 1996. 'Tendinous movement of a human muscle during voluntary contractions determined by real-time ultrasonography', *J Appl Physiol (1985)*, 81: 1430-3.

Glazebrook, M. 2010. 'End-stage ankle arthritis: magnitude of the problem and solutions', *Instr Course Lect*, 59: 359-65.

Haddad, S. L., J. C. Coetzee, R. Estok, K. Fahrbach, D. Banel, and L. Nalysnyk. 2007. 'Intermediate and long-term outcomes of total ankle arthroplasty and ankle arthrodesis. A systematic review of the literature', *J Bone Joint Surg Am*, 89: 1899-905.

Henricson, A., J. A. Nilsson, and A. Carlsson. 2011. '10-year survival of total ankle arthroplasties: a report on 780 cases from the Swedish Ankle Register', *Acta Orthop*, 82: 655-9.

Hintermann, B., A. Barg, M. Knupp, and V. Valderrabano. 2009. 'Conversion of painful ankle arthrodesis to total ankle arthroplasty', *J Bone Joint Surg Am*, 91: 850-8.

Hintermann, B., and B. M. Nigg. 1995. 'Influence of arthrodeses on kinematics of the axially loaded ankle complex during dorsiflexion/plantarflexion', *Foot Ankle Int*, 16: 633-6.

Holt, E. S., S. T. Hansen, K. A. Mayo, and B. J. Sangeorzan. 1991. 'Ankle arthrodesis using internal screw fixation', *Clin Orthop Relat Res*: 21-8.

Hothorn, T., F. Bretz, and P. Westfall. 2008. 'Simultaneous inference in general parametric models', *Biom J*, 50: 346-63.

Huch, K., K. E. Kuettner, and P. Dieppe. 1997. 'Osteoarthritis in ankle and knee joints', *Semin Arthritis Rheum*, 26: 667-74.

Imsdahl, S.I., C.J. Stender, B.K. Cook, G. Pangrazzi, C. Patthanacharoenphon, B. J. Sangeorzan, and W. R. Ledoux. 'Anteroposterior translational misalignments of ankle arthrodesis in cadaveric gait simulation', *Manuscript in Preparation*.

Lawrence, R. C., D. T. Felson, C. G. Helmick, L. M. Arnold, H. Choi, R. A. Deyo, S. Gabriel, R. Hirsch, M. C. Hochberg, G. G. Hunder, J. M. Jordan, J. N. Katz, H. M. Kremers, F. Wolfe, and Workgroup National Arthritis Data. 2008. 'Estimates of the prevalence of arthritis and other rheumatic conditions in the United States. Part II', *Arthritis Rheum*, 58: 26-35.

Lee, K. B., M. S. Kim, K. S. Park, K. J. Cho, and A. Primadhi. 2013. 'Effect of anterior translation of the talus on outcomes of three-component total ankle arthroplasty', *BMC Musculoskelet Disord*, 14: 260.

Leszko, F., R. D. Komistek, M. R. Mahfouz, Y. A. Ratron, T. Judet, M. Bonnin, J. A. Colombier, and S. S. Lin. 2008. 'In vivo kinematics of the salto total ankle prosthesis', *Foot Ankle Int*, 29: 1117-25.

Lundgren, P., C. Nester, A. Liu, A. Arndt, R. Jones, A. Stacoff, P. Wolf, and A. Lundberg. 2008. 'Invasive in vivo measurement of rear-, mid- and forefoot motion during walking', *Gait Posture*, 28: 93-100.

McKearney, D., C.J. Stender, B.K. Cook, B. Monier, B. J. Sangeorzan, and W. R. Ledoux. 'Anteroposterior translational misalignment of total ankle arthroplasty in cadaveric gait simultion', *Manuscript in Preparation*.

Morris, C. H., J. C. Christensen, R. P. Ching, F. Chan, and J. M. Schuberth. 2015. 'Articular congruency of the Salto Talaris total ankle prosthesis', *Foot Ankle Surg*, 21: 206-10.

Piriou, P., P. Culpan, M. Mullins, J. N. Cardon, D. Pozzi, and T. Judet. 2008. 'Ankle replacement versus arthrodesis: a comparative gait analysis study', *Foot Ankle Int*, 29: 3-9.

Preyssas, P., E. Toullec, M. Henry, J. B. Neron, C. Mabit, and J. Brilhault. 2012. 'Total ankle arthroplasty - three-component total ankle arthroplasty in western France: a radiographic study', *Orthop Traumatol Surg Res*, 98: S31-40.

Pyevich, M. T., C. L. Saltzman, J. J. Callaghan, and F. G. Alvine. 1998. 'Total ankle arthroplasty: a unique design. Two to twelve-year follow-up', *J Bone Joint Surg Am*, 80: 1410-20.

Rush, S. M., and N. Todd. 2013. 'Salto Talaris fixed-bearing total ankle replacement system', *Clin Podiatr Med Surg*, 30: 69-80.

Saltzman, C. L., Y. Tochigi, M. J. Rudert, T. E. McIff, and T. D. Brown. 2004. 'The effect of agility ankle prosthesis misalignment on the peri-ankle ligaments', *Clin Orthop Relat Res*: 137-42.

Shibuya, N., D. C. Jupiter, L. J. Ciliberti, Jr., V. VanBuren, and J. La Fontaine. 2011. 'Prevalence of podiatric medical problems in veterans versus nonveterans', *J Am Podiatr Med Assoc*, 101: 323-30.

Suckel, A., O. Muller, T. Herberts, and N. Wulker. 2007. 'Changes in Chopart joint load following tibiotalar arthrodesis: in vitro analysis of 8 cadaver specimens in a dynamic model', *BMC Musculoskelet Disord*, 8: 80.

Team, R Core. 2013. 'R: A language and environment for statistical computing'.

Thomas, R., T. R. Daniels, and K. Parker. 2006. 'Gait analysis and functional outcomes following ankle arthrodesis for isolated ankle arthritis', *J Bone Joint Surg Am*, 88: 526-35.

Thomas, R. H., and T. R. Daniels. 2003. 'Ankle arthritis', *J Bone Joint Surg Am*, 85-A: 923-36.

Tochigi, Y., M. J. Rudert, T. D. Brown, T. E. McIff, and C. L. Saltzman. 2005. 'The effect of accuracy of implantation on range of movement of the Scandinavian Total Ankle Replacement', *J Bone Joint Surg Br*, 87: 736-40.

Usuelli, F. G., C. Maccario, L. Manzi, and E. W. Tan. 2016. 'Posterior Talar Shifting in Mobile-Bearing Total Ankle Replacement', *Foot Ankle Int*, 37: 281-7.

van der Plaat, L. W., S. J. van Engelen, Q. E. Wajer, R. P. Hendrickx, K. H. Doets, H. Houdijk, and C. N. van Dijk. 2015. 'Hind- and Midfoot Motion After Ankle Arthrodesis', *Foot Ankle Int*, 36: 1430-7.

Wahl, E. P., W. R. Ledoux, E. C. Whittaker, B.K. Cook, and B. J. Sangeorzan. 2016. 'Normal and Misaligned Talonavicular Fusion Alters Cadaveric Foot Pressure and Kinematics', *Journal of Orthopedic Research*, In revision for publication.

Wayne, J. S., K. W. Lawhorn, K. E. Davis, K. Prakash, and R. S. Adelaar. 1997. 'The effect of tibiotalar fixation on foot biomechanics', *Foot Ankle Int*, 18: 792-7.

Whittaker, E. C., P. M. Aubin, and W. R. Ledoux. 2011. 'Foot bone kinematics as measured in a cadaveric robotic gait simulator', *Gait Posture*, 33: 645-50.

Wickiewicz, T. L., R. R. Roy, P. L. Powell, and V. R. Edgerton. 1983. 'Muscle architecture of the human lower limb', *Clin Orthop Relat Res*: 275-83.

Wright, W., E. C. Whittaker, B.K. Cook, D. Thuillier, B. J. Sangeorzan, and W. R. Ledoux. 'Coronal plane rotational misalignments of ankle arthrodesis in cadaveric gait simulation', *Manuscript in Preparation*.

Wu, W. L., F. C. Su, Y. M. Cheng, P. J. Huang, Y. L. Chou, and C. K. Chou. 2000. 'Gait analysis after ankle arthrodesis', *Gait Posture*, 11: 54-61.

Younger, A. S., K. J. Wing, M. Glazebrook, T. R. Daniels, P. J. Dryden, K. A. Lalonde, H. Wong, H. Qian, and M. Penner. 2015. 'Patient expectation and satisfaction as measures of operative outcome in end-stage ankle arthritis: a prospective cohort study of total ankle replacement versus ankle fusion', *Foot Ankle Int*, 36: 123-34.

Zhou, S., D. L. Lawson, W. E. Morrison, and I. Fairweather. 1995. 'Electromechanical delay in isometric muscle contractions evoked by voluntary, reflex and electrical stimulation', *Eur J Appl Physiol Occup Physiol*, 70: 138-45.

APPENDIX A: Ankle Fusion Surgical Procedure for Misalignment Fixture

The following procedure was developed with the assistance of Dr. Bruce Sangeorzan, Dr. Matthew Beuchel, Dr. Dan Thuillier, and Eric Whittaker.

A.1 Introduction

The following guide outlines the surgical protocol used to prepare a cadaveric specimen for installation of a custom fixture to simulate ankle fusion surgery and misalignment. Bone is removed from the tibia and talus, with the exact size of removed bone corresponding to the height of the custom misalignment fixture. These cuts are made using the instrumentation from the Salto Talaris total ankle replacement with a custom designed cutting guide. Proper alignment of the cutting planes in the coronal and sagittal planes allows for ankle arthrodesis to be properly imitated with the custom fusion fixture. These fixtures allow for misalignment to be applied in a single direction, in order to quantify the effects specific misalignments of ankle arthrodesis. This protocol was used for studies examining coronal plane and transverse plane rotational misalignments, and anteroposterior translational misalignment of an arthrodesis.

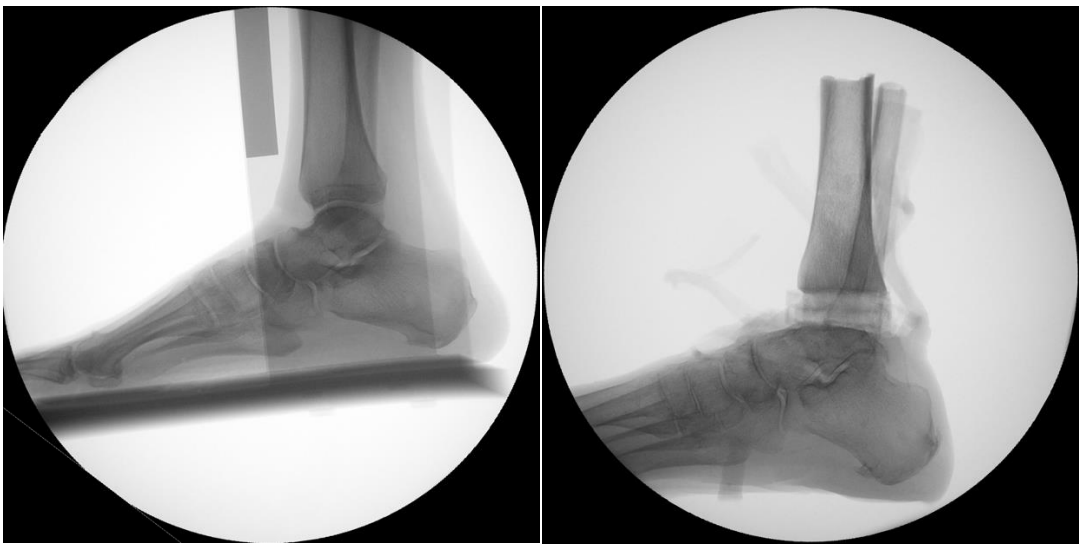

Figure A.1**:** Specimens before and after bone removal of custom arthrodesis surgery.

A.2 Surgical Technique

1. Place aluminum rod into tibia, to extend bone, and serve as a virtual “tibial tuberosity” to pin the alignment guide to. If necessary, bore out the tibia with the 12.7 drill bit. Place a long (75mm) pin in one of the holes in the tibia rod (as the holes are slightly oversized, it may be required to put tape around the pin to get a secure fit). Use the suction cup stand to keep the specimen in place throughout the surgery (Figure A.2). Wait until the alignment guide has been put onto the specimen to hammer the tibia into the bone.

Figure A.2: Initial preparation of the specimen.

2. Make an incision along anterior aspect of ankle (Figure A.3), between the tibialis anterior and extensor hallicis longus tendons. Cut through into joint capsule of ankle. Removal of a portion of the talar head osteophyte may be required for placement of alignment guide.

Figure A.3: Anterior incision (left), cutting through the joint capsule to reveal the tibiotalar joint surface (middle) and removal of osteophyte on talar head (right).

3. Place alignment guide on pin in tibia rod. Once the alignment guide is in approximately the correct superior/inferior position, hammer the tibia rod into the bone to establish a secure fit (Figure A.4). Start the alignment guide at "0 mm" for the adjustable superior/inferior portion. Drill a pilot hole for the lower pin to be placed above the ankle. Set the transverse plane alignment of the cutting guide, by aligning the anterior-posterior axis with the second ray by eye. Take the specimen to the C-arm fluoroscope for rest of the alignment of cutting guide (Figure A.5).

Figure A.4: Placing the alignment guide onto the specimen (left), drilling the pilot hole for the lower pin (right)

Figure A.5: The distal tibia pin in place, above the ankle (left) and the specimen placed on the table on the C-arm.

4. Take fluoroscope images to establish good alignment of the cutting guide. Use of the acrylic board can act as a ground to put the foot in neutral position. The alignment of the cutting guide must be set in following directions:
    a. Superoinferior position: align the cutting plane with the joint line of the ankle.
    b. Sagittal plane rotation: With the tibia at a 90 degree angle to the ground, move the cutting plane of the alignment guide parallel with the ground (Figure A.6).
    c. Coronal plane rotation: Align cutting plane normal to the axis of the tibia and/or with the bottom of the tibia (Figure A.7).
    d. Mediolateral translation: Align the alignment guide centered between the malleoli (Figure A.8).

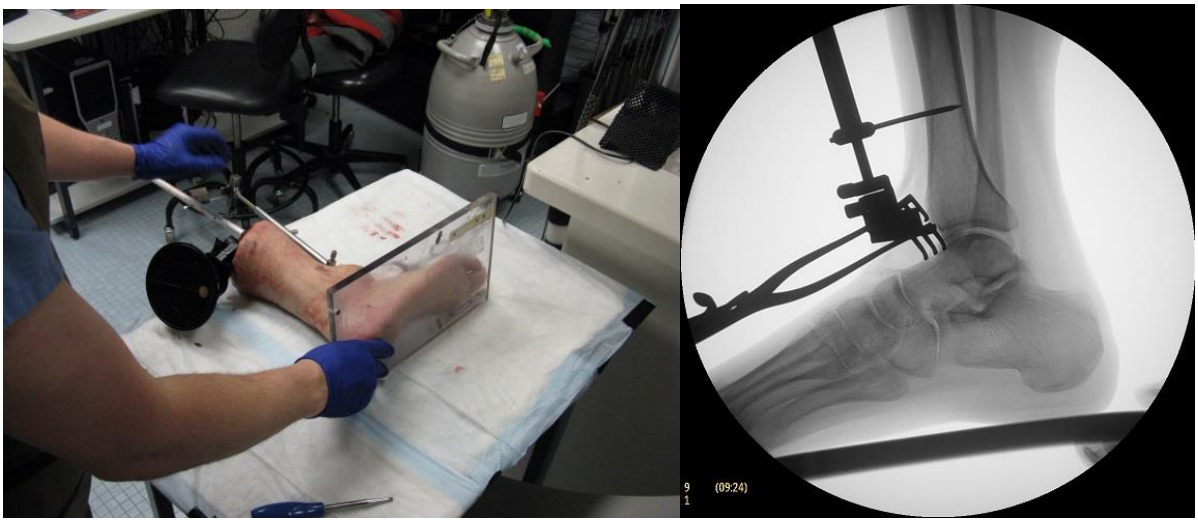

Figure A.6: Use of the acrylic board to find neutral position (left) and sagittal plane alignment, with cutting guide parallel to ground, with translational alignment at joint line.

Figure A.7: Coronal plane alignment.

5. Put on the tibial cutting guide. Move the guide up (superiorly) on the tibia to the cutting position (Figure A.8). For a large foot, move up 6-7 mm, for a small foot move up 8-9 mm. Take additional fluoroscope images to confirm the medial lateral alignment of the cutting guide, making sure the holes on both the medial and lateral side are aligned such that they will not allow the drill bit to go into the malleolus. The talus cut will be based off the location of the tibial cut. It was found that on larger feet, the higher tibia cut (8-9 mm) would result in very little of the talar dome being cut, resulting in a small plane of contact for the fusion device and talus, and a less stable connection.

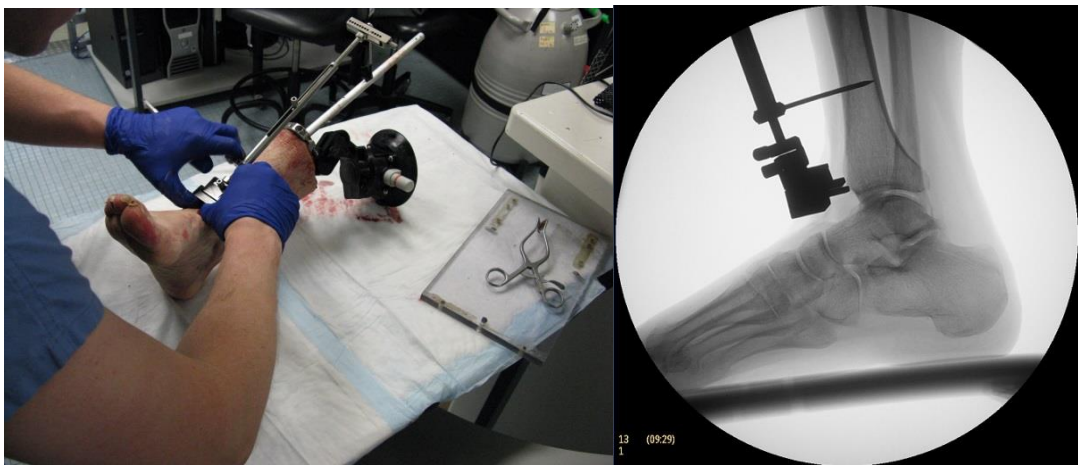

Figure A.8: Cutting guide added to setup (left), cutting guide added in fluoroscope image.

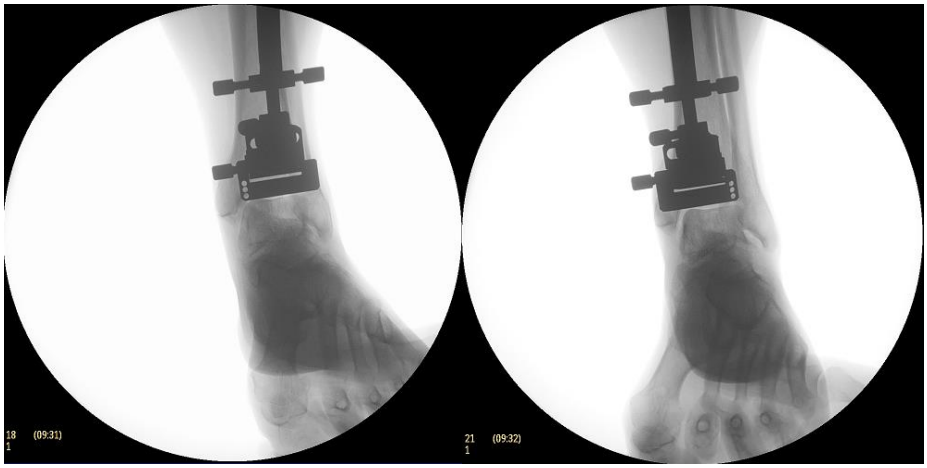

Figure A.9**:** Fluoroscope image with foot angle such that the medial (left) and lateral (right) holes in the cutting guide can be checked.

6. Place pins in tibia cutting guide to secure it to the bone. Drill out the bottom two holes to create a cutting plane for the medial and lateral malleolar gutters (Figure A.10).

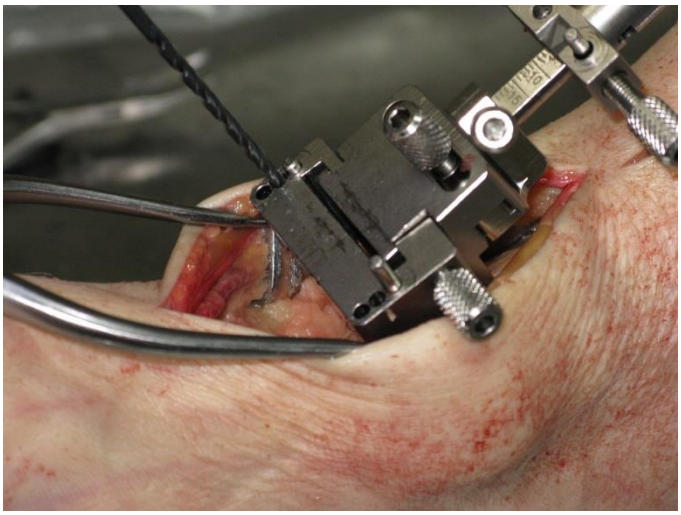

Figure A.10: Cutting guide with pins placed, drilling out other holes.

7. Make the tibial cut using the Microaire saw (Figure A.11). Remove as much of anterior bone as possible from the cut, the posterior part can be removed easier after talar cut is made (Figure A.12).

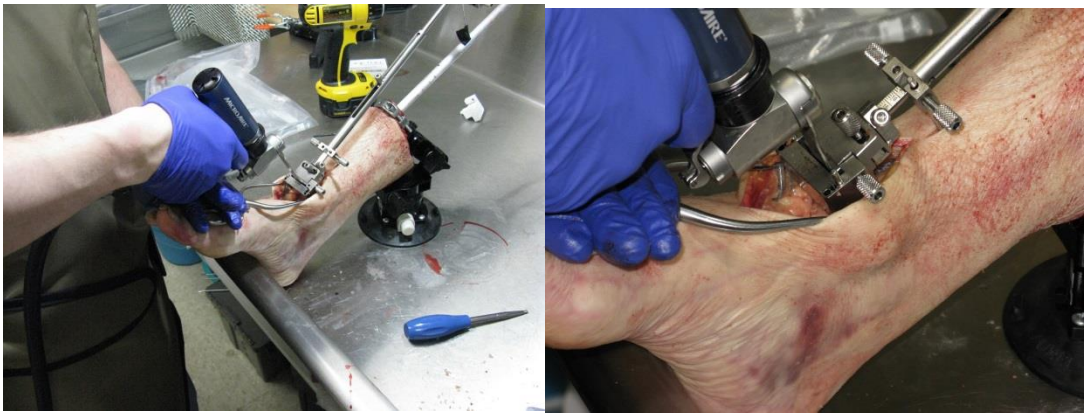

Figure A.11: Making the tibial cut with the Microaire saw.

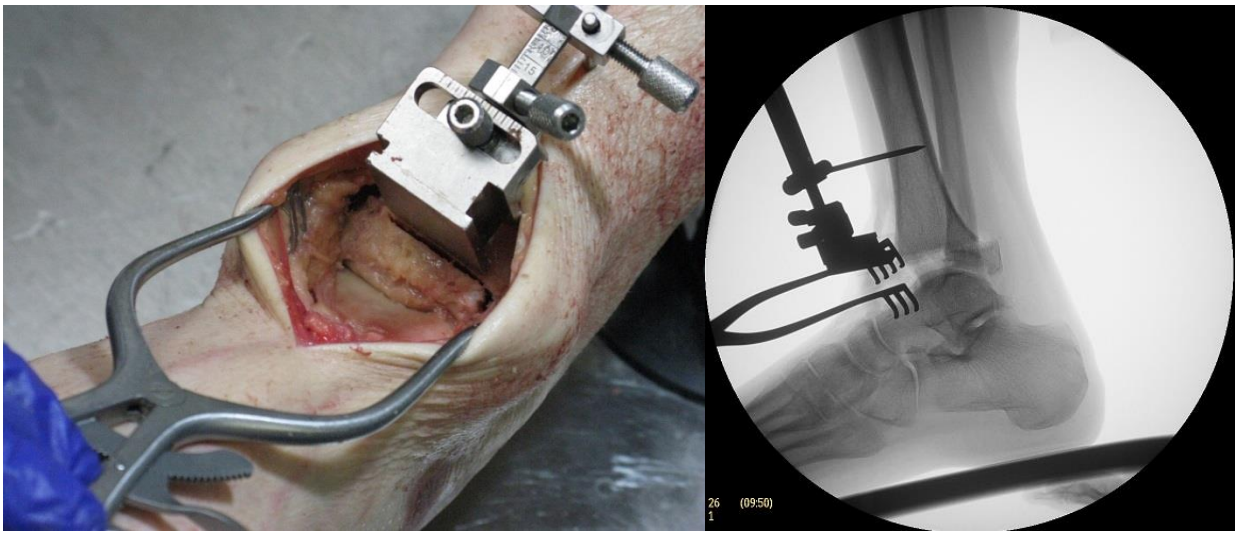

Figure A.12: Tibial cut before any bone is removed (left), fluoroscope image after tibial cut and removal of bone (right).

8. Place the custom talus cutting guide onto the stock alignment guide. (For these images, the cutting guide was 3D printed from plastic, but has subsequently been machined out of steel.) Establish a 90 degree again between the tibial axis and floor. Place the pins for the alignment guide into the talus, making sure the pins do not defect when going into the talus (Figure A.13).

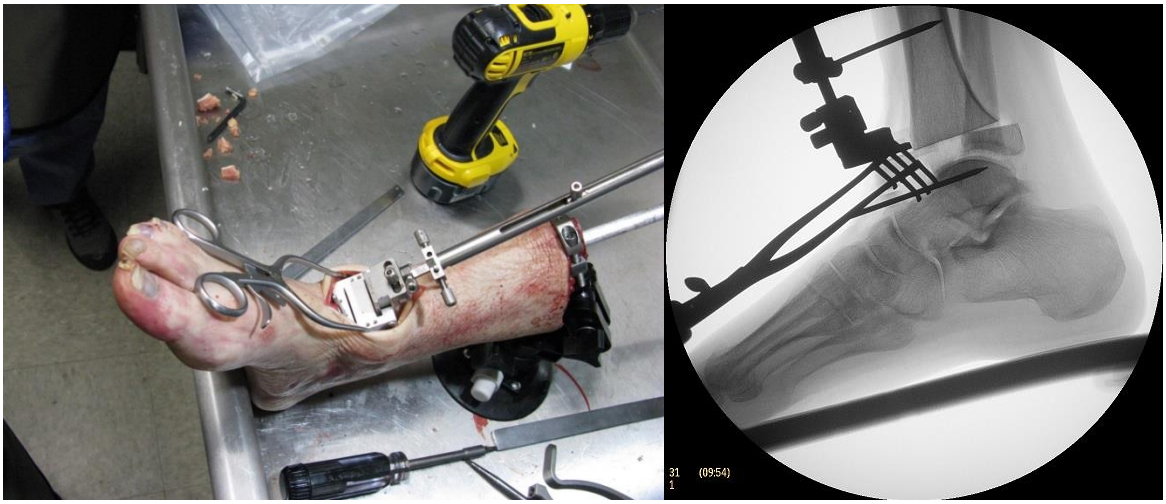

Figure A.13: The plastic talar cutting guide with one pin placed in the talus (left), fluoroscope image of one pin placed in talus (right).

9. Make the talar cut, using the bottom slot on the talus cutting guide. Remove all bone from the cut. Additional bone may also be taken from the malleolar gutters depending on which misalignment is being performed (Figure A.14, A.15).

Figure A.14: Making the talus cut (left). The piece of talar dome removed in talus cut (right). Note: the piece of bone should generally be larger than this.

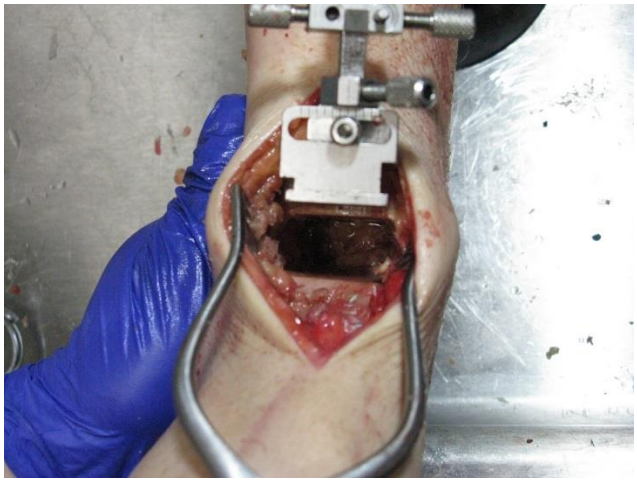

Figure A.15: The ankle joint after all of the bone is removed.

10. Size up the fusion device to confirm the cut is the correct dimension using the fluoroscope.

    Ideally, there should be a tight fit between the fusion device and the bone (Figure A.16).

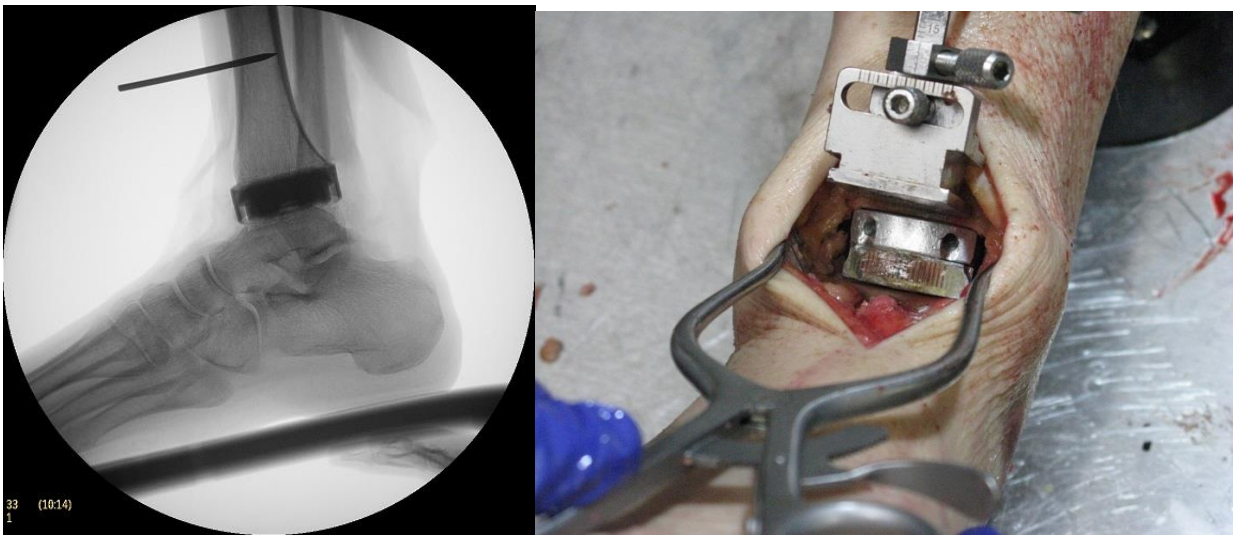

Figure A.16**:** The fusion device implanted in the ankle.

11. Finally, a large incision can be made on the posterior side, to the point just deep of the Achilles tendon, as this tendon must be reflected in order to access the posterior side of the fusion device. Additionally, a smaller incision can be made on the medial side, making sure to keep the tibialis posterior, flexor digitorum longus, and flexor hallicis longus tendons intact.

APPENDIX B: RGS Testing of Ankle Fusion: Specimen Preparation and Testing Protocol

B.1 Introduction

The following protocol overviews testing ankle fusion specimens on the robotic gait simulator (RGS). The RGS was developed with the idea of testing normal, unfused feet. Thus, when a major source of sagittal plane motion in the foot is fixed, the controllers behave slightly differently, making it far more challenging to match the ground reaction force (GRF). This protocol outlines the minor changes made to specimen preparation, in order to test on the RGS efficiently and successfully. This protocol was developed after the ankle fusion transverse plane rotational misalignment study, and the ideas were implemented in the anteroposterior ankle fusion study, resulting in a far greater success rate of specimens being tested, and far fewer trials required during the testing day, reducing tissue degradation.

B.2 Preparation of Specimen

The dissection required for the specimen was altered in the following ways in order to access the fusion fixture. Complete removal of the ankle joint capsule on the anterior and posterior side was needed to have enough room to access the bone screw through-holes in the tibia plate. On the lateral posterior side, most of the tendon sheath, retinaculum, fat, and other soft tissue had to be removed, while being careful not to cut the peroneus brevis or peroneus longus. Accessing the posterior medial joint side usually required cutting down the tendon sheath/retinaculum of the tibialis posterior and flexor digitorum longus. The angle of the bone

screw and space required to start the screw must be taken into account, so it was determined that much more soft tissue had to be taken out than what was necessary to just have the two plates fit in the area. The Achilles tendon was reflected down to or below the level of the posterior talus, in order to have posterior access to the fixture. On the anterior side, it was found that the soft tissue got in the way during bone screw installation if any tibialis anterior tendon sheath was in the way, thus the tibialis anterior tendon (and the extensor hallucis longus and extensor digitorum longus tendons) was cut from all attachments proximal to the ankle joint. The downside of cutting away these attachments is the line of action for each of these tendons was moved quite a bit anterior. This was remedied by using Coban (Coban, 3M Inc., Maplewood, Minn.) to make a "retinaculum/tendon sheath" for the pretibial tendons, which will be described in detail later. If there was excessive fat around the tibialis anterior near the talonavicular joint, it sometimes had to be removed to make the anteromedial tibia screw easier to insert.

Once the dissection is complete, additional removal of bone is required. The gutters of the malleoli were cut down using the Stryker saw and rongeurs. The amount of bone removed was intended to provide enough space for adequate for the rotational misalignment of the transverse plane misalignment project, but cutting down these malleoli can give more medial/lateral (ML) space when lining up the fixture for placement.

For Vicon screws, there is not much difference from a normal foot, besides using a "calcaneus" (longest) screw for the talus, because the surgical incision causes the soft tissue to be very loose around the bone, and the extra screw length prevents the screw head from getting lost in the excess tissue, allowing for the quad to be placed in much easier. If the screw does not feel secure when placed in the talar head, the screw can be placed in the posterior talus instead, depending on how much bone is left by the surgical cut on the talus. It is important to place the

talus screw in such a way that the talus quad will not be completely in the way for adjustments of the fixture/changing misalignments. Putting the screw to easily orient the quad directly medially can help make the misalignments easier.

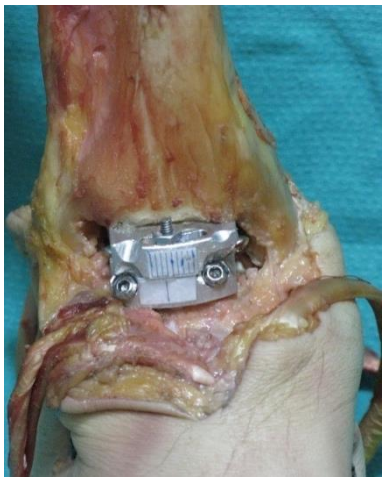

Figure B.1**:** Anterior view of the ankle fusion fixture after dissection, with tendons' attachment to tibia removed, and joint capsule removed on medial and lateral side.

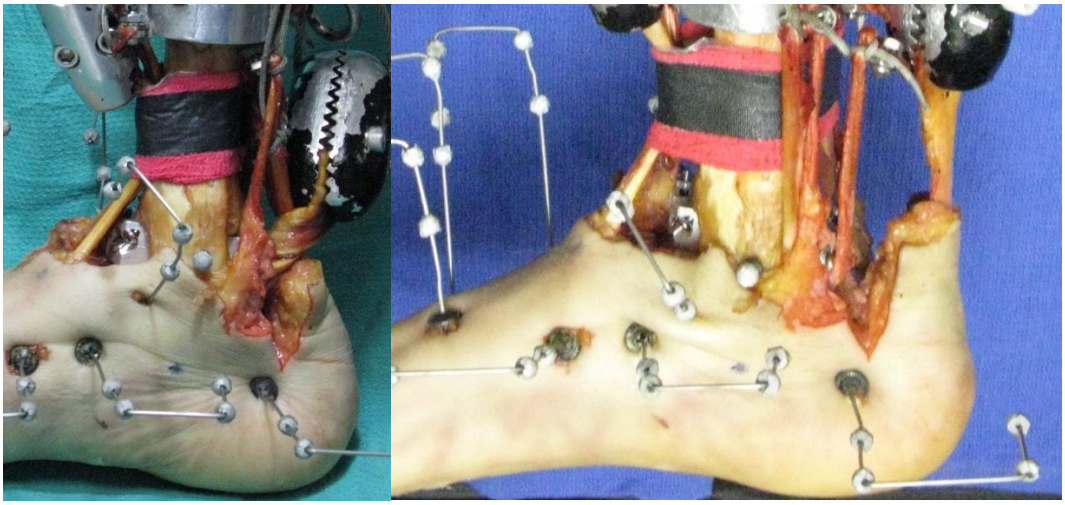

Figure B.2: Medial views of the ankle fusion fixture implanted in a specimen, post-dissection.

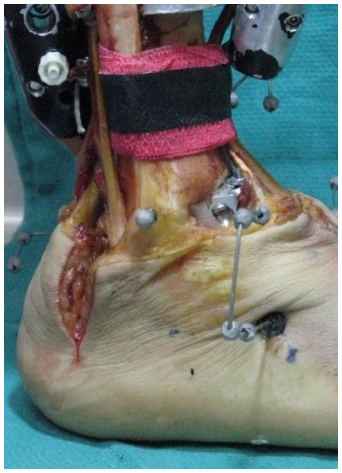

Figure B.3: Lateral view of the ankle fusion fixture implanted in a specimen-post dissection.

B.3 Implantation of fusion fixture

All Vicon screws must be installed prior to fixture placement. Under the C-arm, the fixture was lined up in neutral position that would mimic the position of the actual ankle fusion surgery. The fixture must be lined up in neutral anteroposterior translational position, ML translational position, and transverse plane rotation. The anterior/posterior (AP) position was found using a lateral radiograph. Superiorly, the anterior of the tibia must be aligned with the middle of the fixture, and inferiorly, the fixture was centered on the talus. ML position was determined using an AP Radiograph (down the talocrural joint), and the fixture should be centered between the malleoli. Depending on how the malleolar gutters are cut down, this can make the ML placement look asymmetrical compared to the space cut out, so determination of center of the joint should be made in reference to the center point between the medial and lateral malleoli. The transverse plane alignment was determined using a radiograph down the axis of the tibia (superior/inferior), and the fixture was lined up such that it was parallel to the second ray. In the case that there was substantial abduction of the second toe relative to the second metatarsal,

only the second metatarsal was used for alignment. For extreme cases where the second metatarsal was severely adducted, and the second toe was abducted, the difference was split between the two for the alignment (i.e., the access from the base of the second metatarsal to a middle point approximating the two axes). For the AP translational misalignment study, this neutral AP position is much more important, so it may be useful to mark the tibia and talus prior to the surgery using small radio-opaque screws or pins, or drill holes that pins can be placed in after the surgery to keep the pre-surgery alignment in order to mimic the anatomical neutral position.

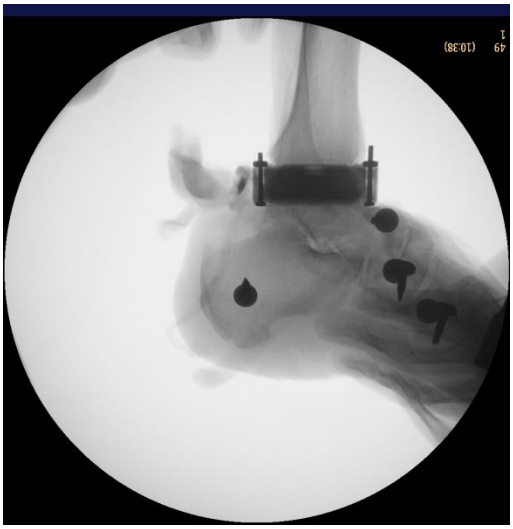

Figure B.4: A lateral radiograph to determine the AP neutral position (this image has the fixture slightly too far posterior on the talus).

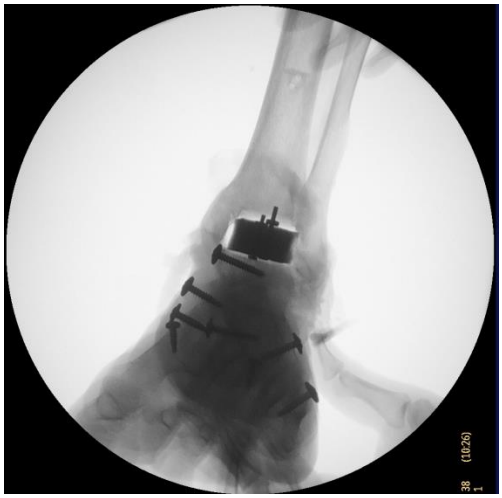

Figure B.5: A mortise radiograph to determine ML neutral position (this image seems like good alignment, but a better radiograph directly perpendicular to the side of the fixture would be preferable).

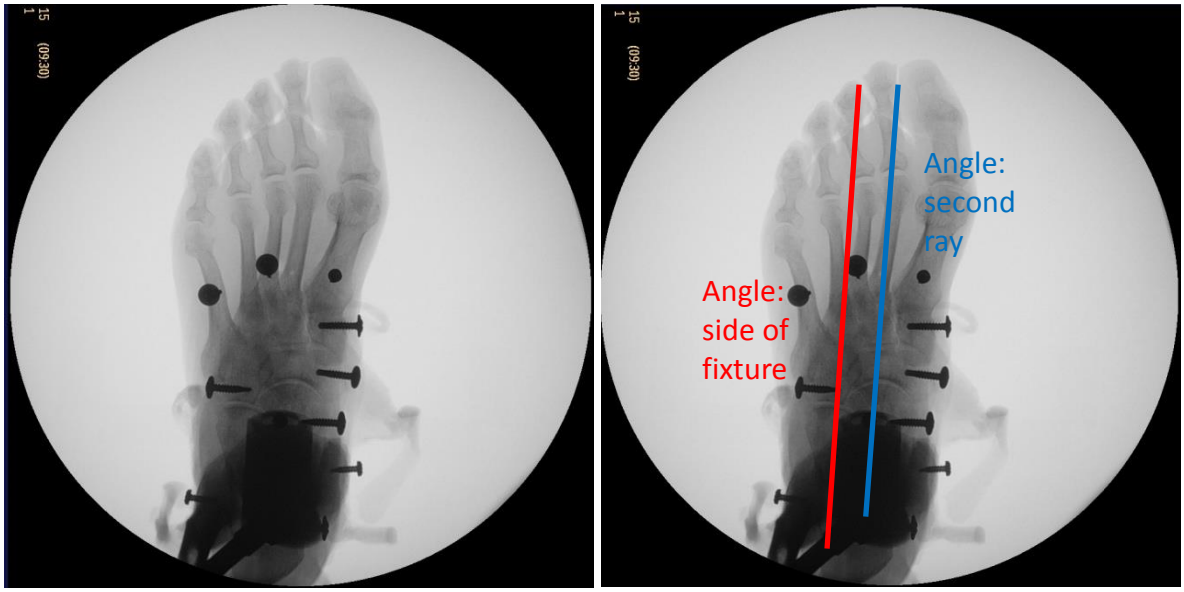

Figure B.6: (Left) Superior-Inferior radiograph to determine neutral transverse plane alignment, using the screwdriver to press on the tibia to get hands out of the fluoroscope field (Left). The goal is to line up the fixture parallel to the second ray, measured by lining up the side of the fixture parallel to the axis of the second ray (Right). If the second metatarsal is adducted and the second toe is abducted, only the second metatarsal was used for alignment, or the different was split in extreme cases.

For implanting of bone screws, the tibia was always done first. The alignment of the device must be continually checked, and re-checked, to ensure that neutral position was

maintained throughout the placement of screws. The fixture was always set at neutral position (0 degrees misalignment) when being put into the ankle. Even though it is possible to move the talus relative to the fixture after tibia has been fixed, it is better to determine neutral position before the tibia is fixed, to prevent a "neutral" position where the soft tissue is very tight, making misalignment very difficult. This will probably be less of an issue in terms of limiting misalignment for the AP misalignment study compared to the transverse plane, but still good practice to line everything up before any screws are put in. Do not use the drill with a hex head to tighten the screws, as that will damage the fixture's holes. The green handled hex driver is the correct size (2.5 mm) for all of the bones screws the fixture was designed for. Starting two different bone screws (opposite corners) is preferable to prevent movement of the fixture as the screws are tightened (one bone screw inserted completely still allows rotation of the fixture relative to the bone as it is tightening, which can alter the alignment of the fixture). Once the first two screws are fully tightened, the other two screws can be put directly in. I preferred to use the long (50-75mm) for the tibia. It is good to insert screws into the fixture before the fixture is in the ankle (i.e., in air), to confirm there will be no interference, and have a plan on know which size screws to use in each of the eight holes using fluoroscopy. Screw size on the talus is very important, as each screw must penetrate the inferior cortex of the talus, but not go into the subtalar joint. The 20-30 mm long screws were used, depending on the specimen and the surgical cuts. It can be beneficial to examine lateral radiograph views to get an idea of how far the screws are going to go inferiorly into the talus. This can be done by placing the screws in the holes, which will show the angle they will be going into the bone, allowing you to estimate how far that screw size will go into the talus. Pilot holes can be used if the screws are difficult to start, but allowing the screw to self-tap allows for better thread fixation. Once all eight screws are in, make

sure the fusion feels solid, as there should only be subtalar joint motion when the tibia is moved around. If the subtalar joint motion feels rough, there is a chance one of the screws was placed too far inferiorly into the talus, so a smaller screw must be used.

Figure B.7: Checking the rotation as the screws are put in (anterolateral tibia screw started).

Figure B.8: After placement of tibial bone screws.

Figure B.9: Sizing talar screw and examining the insertion angle to determine if it will go into the subtalar joint.

Figure B.10: Confirming the transverse plane rotational neutral position after two of the talar screws are started, but not tightened down (anteromedial and posterolateral).

Figure B.11: Two talar screws installed. The anterior screw should go much further inferior than this, so a larger screw would have been preferable. The posterior screw is adequately placed in the inferior cortex.

Figure B.12: All four screws installed in talus (same specimen as previous image). The second anterior screw was a better length.

Figure B.13: An AP radiograph with all eight screws installed.

B.4: Remaining specimen prep:

The Vicon markers/tendon connections are very similar to the normal foot prep. It was preferred to wait until just the clamps/strings were put on to mark the digitizing point landmarks, because the foot is handled so much before that point, that the marks come off the skin. A Coban retinaculum/tendon sheath was used to correct the line of action for the pretibial tendons. This was usually done by cutting a 3cm x 10cm piece from a garbage bag liner, and taping it using rolled gaffers tape to one end of a 150cm piece of Coban, folded length-wise. This Coban was placed around the tibialis anterior, flexor hallucis longus, and flexor digitorum longus tendons, and wrapped around the posterior part of the specimen anterior to the deep posterior

compartment tendons (i.e. against the tibia). It is best to put the liner at the end of the Coban piece, then wrap the Coban around onto itself, and then use gaffers tape around the Coban to secure it, all while making sure the liner ends up over the pretibial tendons. This was done just before putting in the Vicon marker clusters, and right after attaching strings to the tendons It is important not to tangle the three tendons within the Coban, as this can create issues when the actuators pull on them.

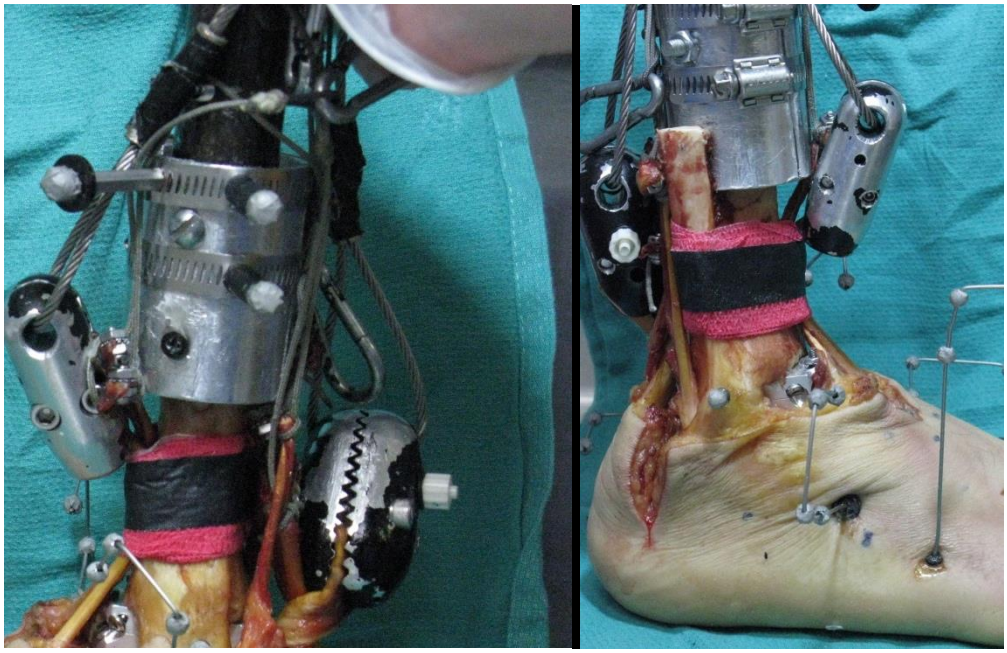

Figure B.14: The Coban retinaculum in medial (left) and lateral (right) images. The Coban only wraps around the tibialis anterior, extensor hallucis longus, and extensor digitorum longus, and is directly contacting the posterior tibia.

B.6: Beginning of RGS Testing

Static tendon forces: The static forces in the table below were used successfully in ankle fusion RGS testing. The large force on the tibialis anterior assists with keeping the foot in a slightly dorsiflexed position at heelstrike, but it can also make the foot very inverted. If the

pliance data shows only lateral foot or if the foot looks too inverted, increasing the PL and PB to 10-20 N can evert the foot more towards neutral.

Table B.1: Static muscle actuator forces used for ankle fusion testing.

Muscle/Tendon	Static Force (N)
Achilles	15
Extensor digitorum longus	12
Extensor hallicus longus	8
Peroneus longus	4
Peroneus brevis	4
Flexor digitorum longus	4
Flexor hallicus longus	4
Tibialis posterior	4
Tibialis anterior	30

The best practice for testing multiple conditions for the transverse plane misalignment study was to match the target vGRF curve with the foot in neutral condition. After this "starting point" trajectory is created, go through each randomized misaligned condition, using this trajectory to begin the process again. Usually there was very little difficultly matching the vGRF once the trajectory was created for matching the neutral condition.

For the pliance system, a new mask/.mfg file (defining different sensors to be scanned) was created for each misaligned condition, to increase the sample rate. With the 32x32 sensor array all working, it should be easy to place the pliance mat on the robot such that the mat will not need to be moved between testing conditions.

B.7: Matching the Vertical Ground Reaction Force

Matching the ground reaction force can be challenging, as the system is tuned to match 50% bodyweight target curves, for normal feet. The biggest challenge is to prevent major

discontinuity of the vGRF curve when the Achilles controller turns on at 40% stance phase. Although the iterative delta-x controller and Achilles controller are supposed to ramp down and ramp up respectively at this transition, it can still cause major discontinuities. In general, our more successful specimens have been with overshooting the ground reaction force curve by moving the trajectory closer to the foot. It is desirable to have vGRF at the transition point (40%) just at or just above the target value. The iterative controller and TA fuzzy controller will fix everything before the transition, and the Achilles tracks well after 40%, but it is a major key to have the vGRF right at the target value for this transition to prevent the Achilles controller from over-shooting. The iterative learning control (ILC) gain for bring the vGRF curve down to the target can be 3.5-5.0 if there are big changes, but the non-linear nature of relationship between the foot-position and vGRF makes it difficult to make minor changes, thus a larger gain can be necessary to make small changes (<20 N difference). It is best to match the iterative portion of the curve first without the Achilles fuzzy controller, making sure the vGRF will be close to the target when the Achilles controller turns on (un-check the Achilles fuzzy controller button until you know the vGRF curve will be correct at the point of the controller transition). The overall expectations of an “acceptable” vGRF should be lower, compared to a normal foot at 50% body weight. Having nearly all the curve within the 10% band besides some noise at the Achilles controller transition and being above the target from 90-100% stance phase has been considered acceptable for challenging specimens. If few trials have been used to get a perfect vGRF, then it may be worth fine-tuning, but more than 40-50 trials to get the vGRF to an adequate match, it can set up for degradation of the specimen, especially if your study is attempting several different conditions. The most number of trials run on a single fusion specimen was 196. The four examples below give an idea of the thought process behind matching the target vGRF curve.

B.8 Examples of matching the vertical ground reaction force with the RGS.

Example 1: Specimen 0184L-BW 1111.25 N (changed trajectory file after ~12 trials, so example matching begins on Sim19.

Sim 19

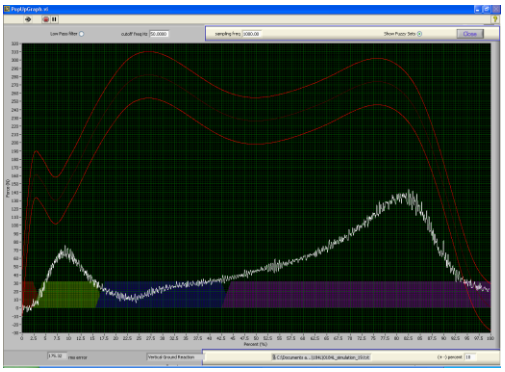

Standard low contact pattern, brought force plate closer to foot for next.

Sim20

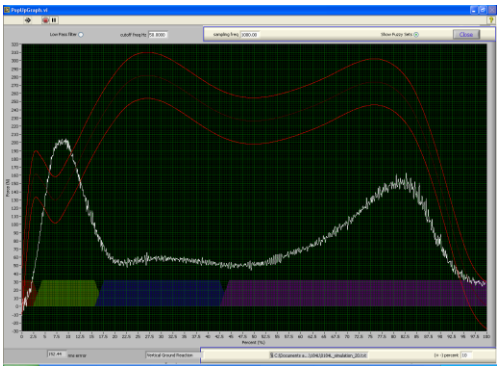

Still slightly low GRF, brought in force plate more for next.

Sim21

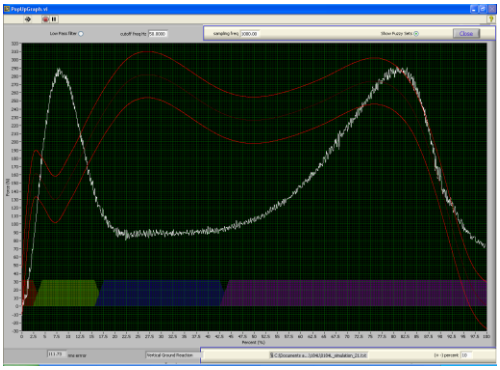

Bring in slightly more, start iterative set next.

Sim 22-Start IFLC set

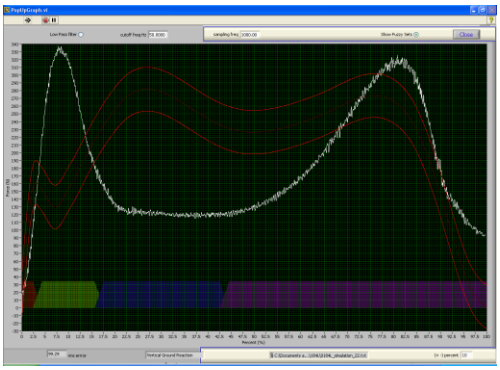

Okay starting point, will not reach target in 30-40%

Sim23

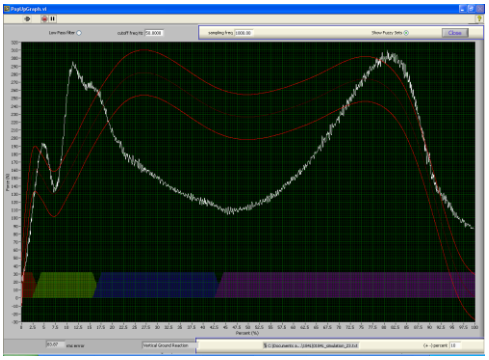

Sim24

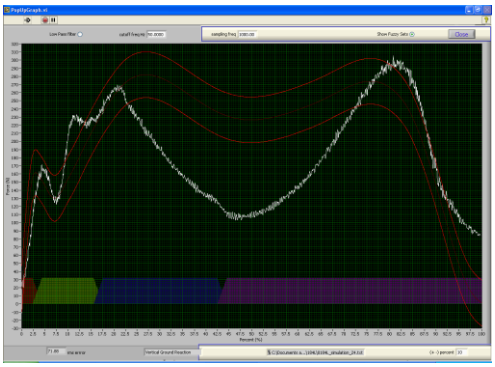

Sim25-Result from 22

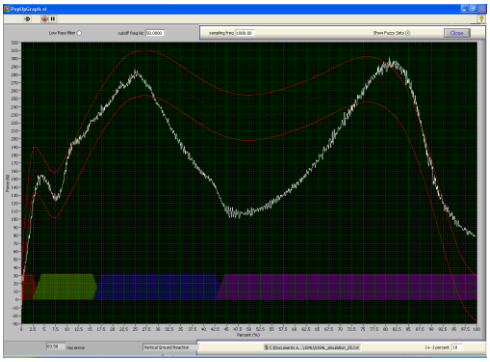

Looks great for first 25% stance.

Sim 26-Start IFLC set, building off traj. 24

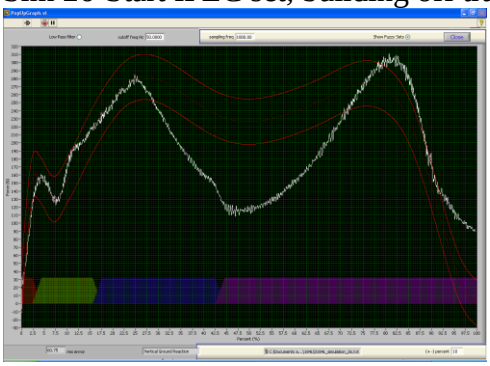

Sim27

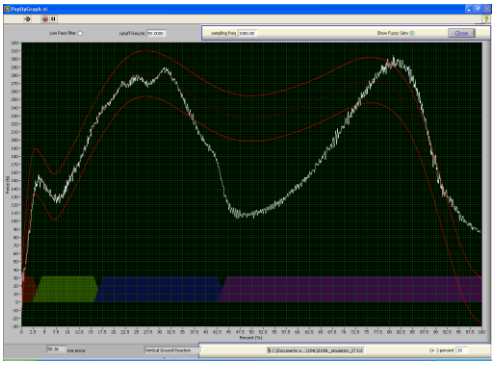

Sim28

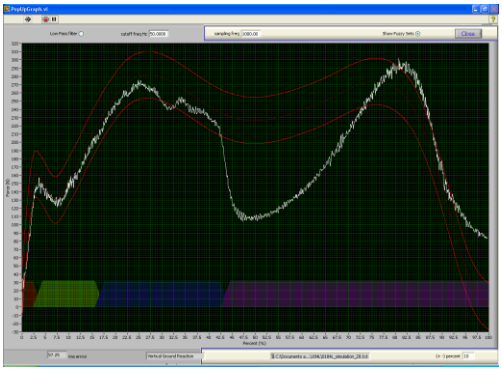

Sim29-Results from 26

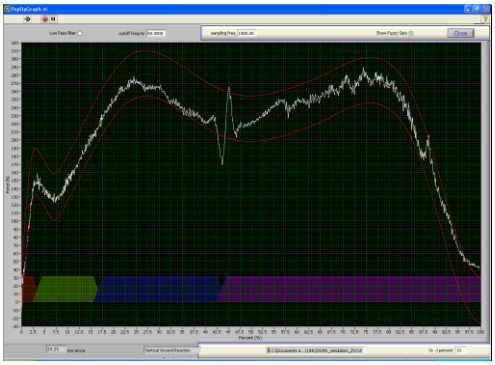

Close, but very apparent drop at 40% as delta-x controller is turning off, which caused the discontinuity.

Sim30-Start IFLC set, building off traj. 28-brought FP closer to foot.

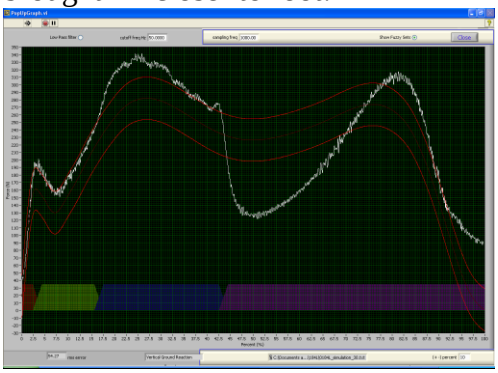

Sim31

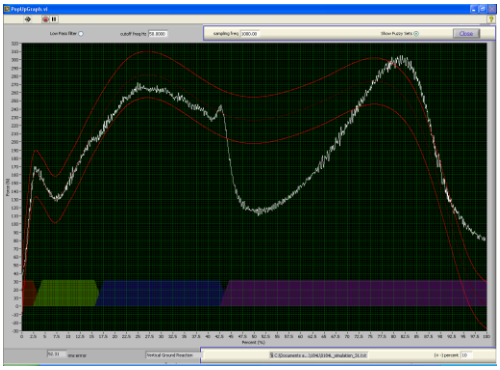

Sim32

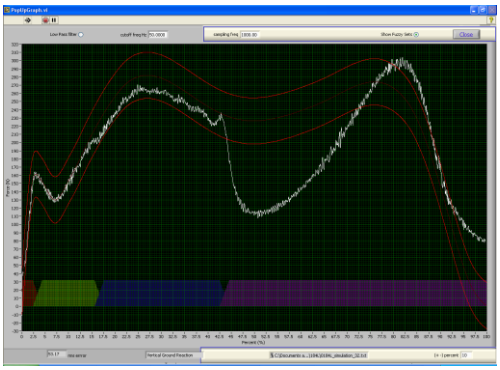

Sim33-Results from 30 (kept data).

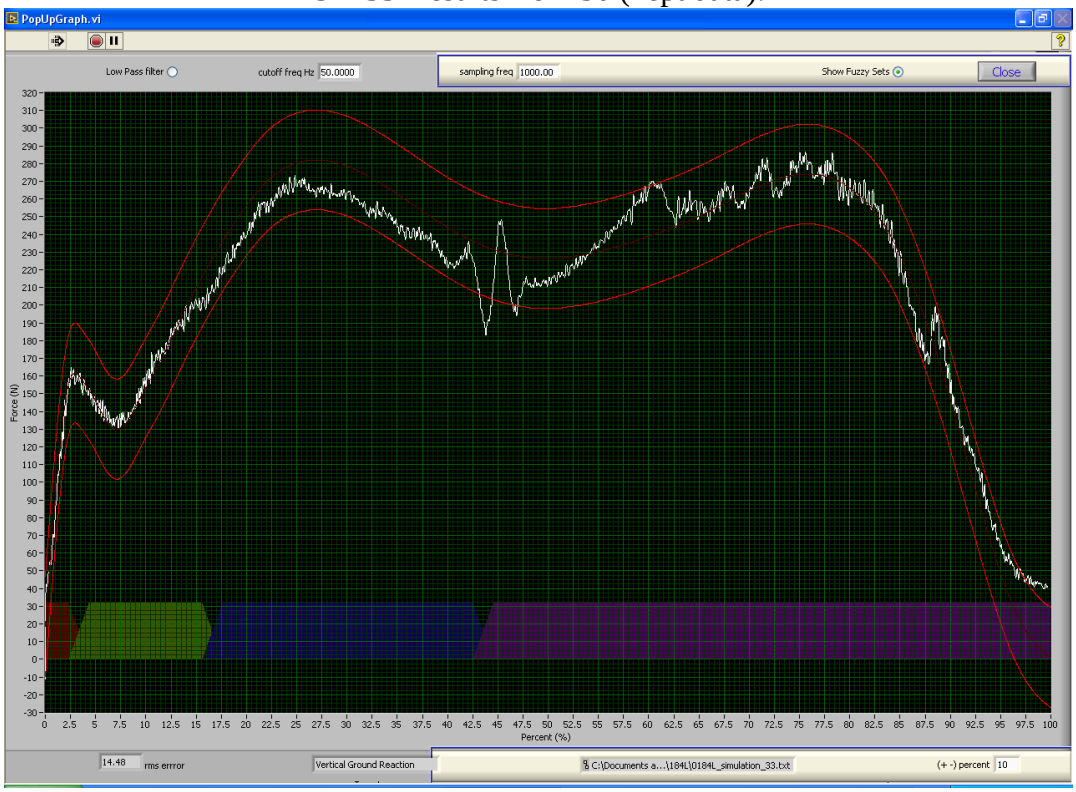

This is acceptable data, even with the discontinuity at as the Achilles controller turned on. The data got a little better for this foot as the day went on, this trial has an RMS error of 5.2% (N/25%BW), well within the goal of 10% error.

Example 2: Specimen 215R (BW 1023.5 N)

Sim 2

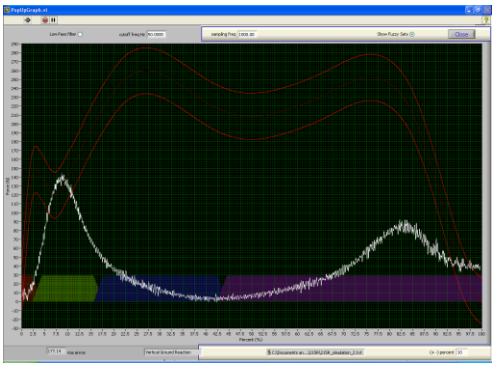

Brought in force plate closer to foot next.

Sim3

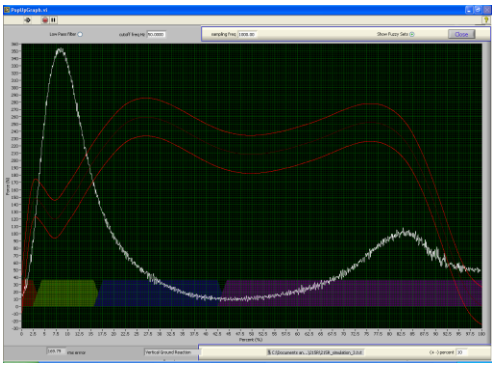

Sim4

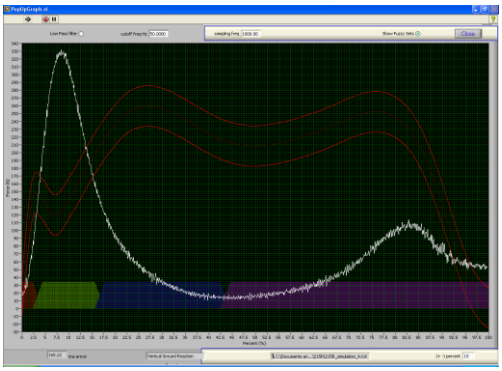

Sim5

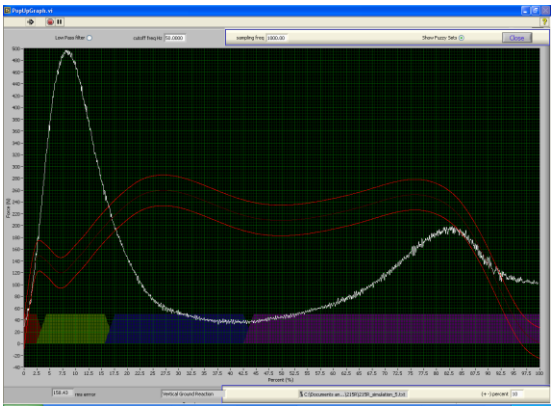

Too high, brought away slightly next.

Sim6

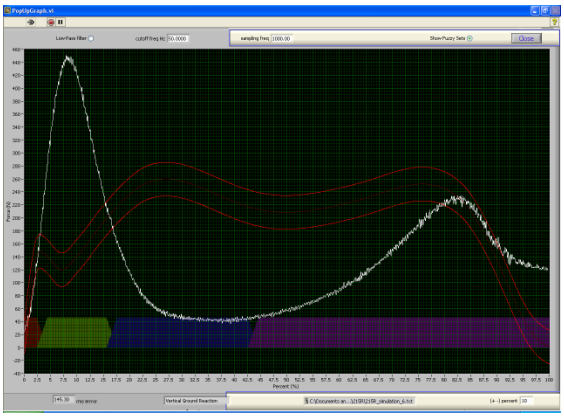

Brought away from foot slightly, start IFLC.

Sim7-Start IFLC set.

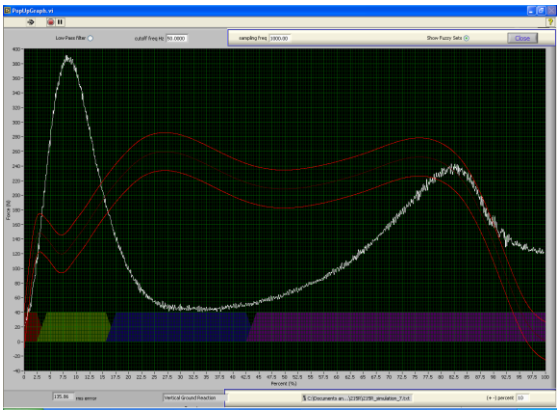

Sim8

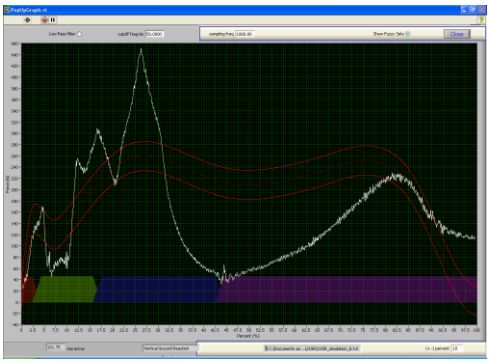

Sim9

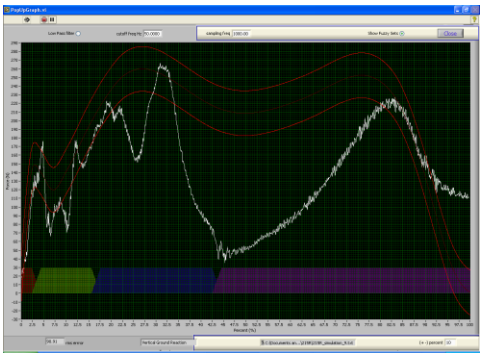

Sim10-Result from 7.

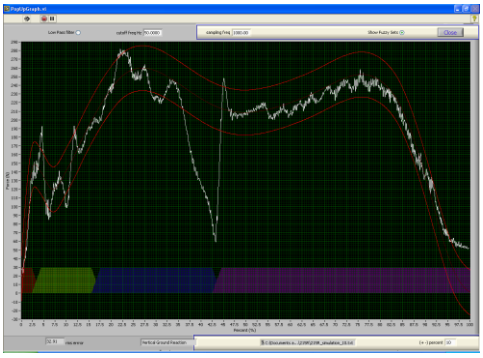

Sim11

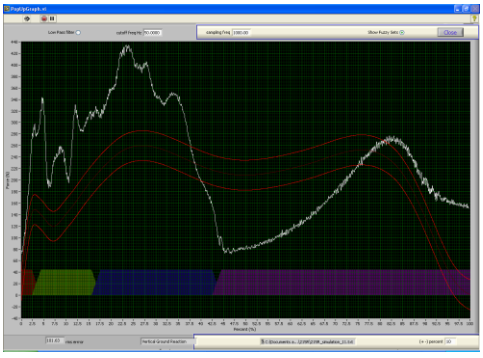

Brought closer to foot.

Sim12

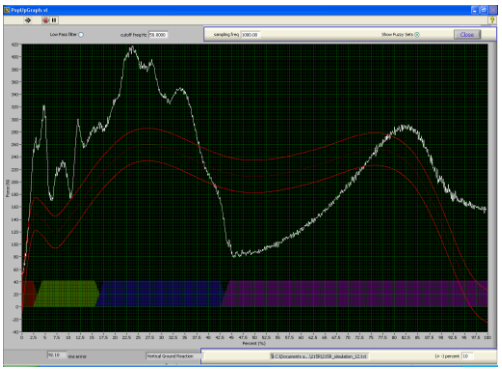

Moved back from foot slightly.

Sim13-start IFLC set

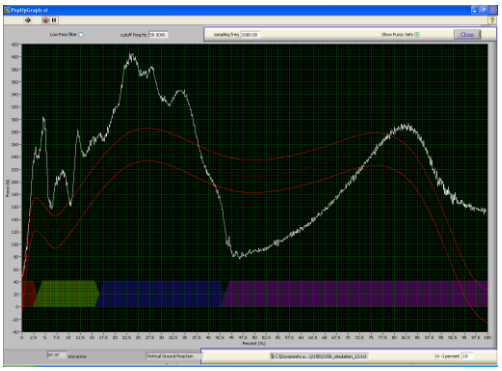

Sim14

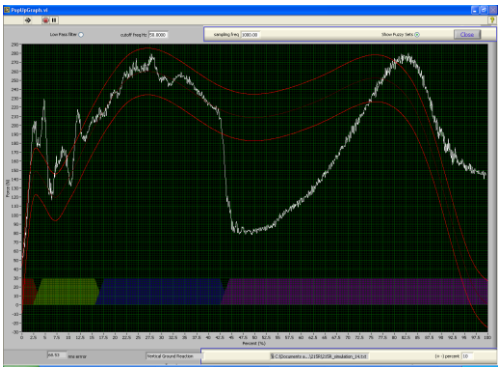

Sim15

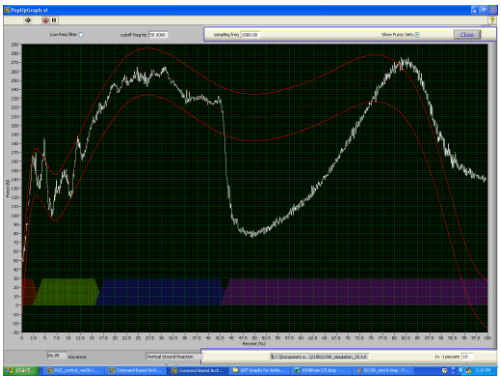

Sim16-result from 13.

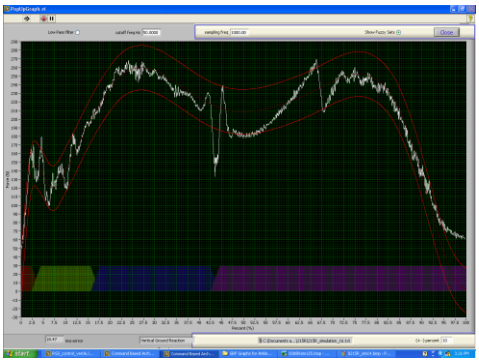

Close, just re-ran iterative controller next.

Sim17-start IFLC set.

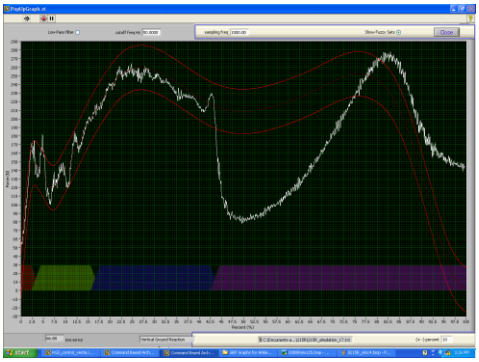

Sim18

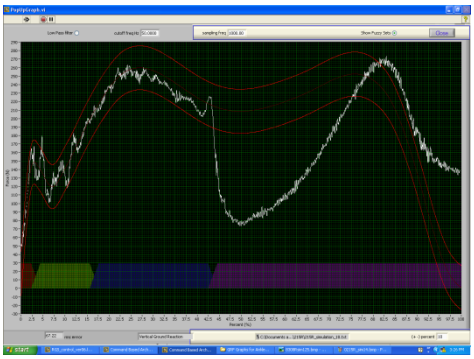

Sim19

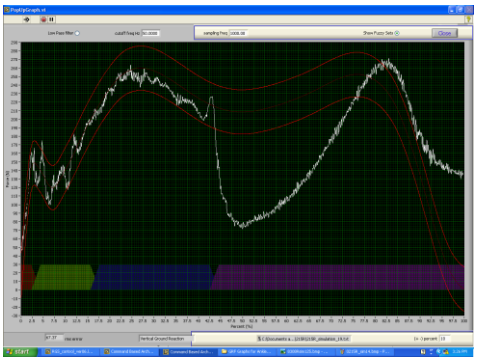

Sim20-result from 17

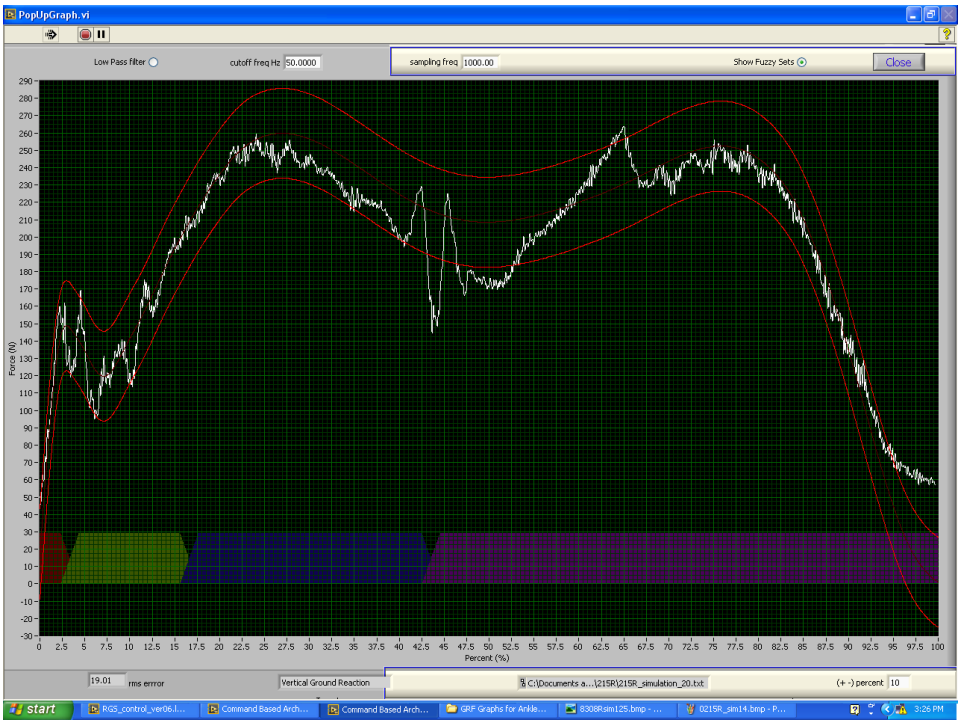

Kept Data

Sim24

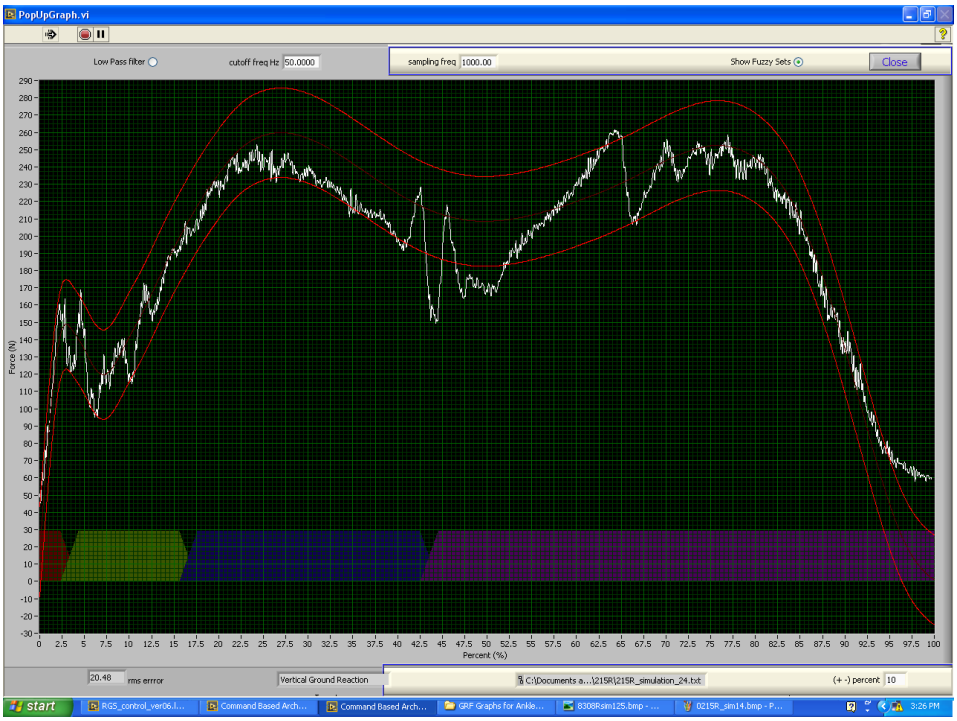

Result from next IFLC set (kept data again).
As seen from sim20 and sim24, there is discontinuity at the transition to the Achilles controller.
The RMS error is 7.7% (N/25%BW) for sim20, again within the 10% target.

Example 3: 0249L (BW 890 N)

Sim2

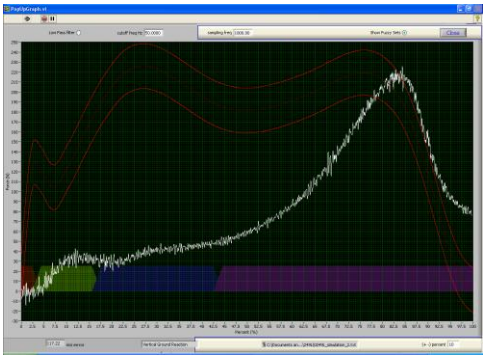

Starting Point: brought in closer for next.

Sim3

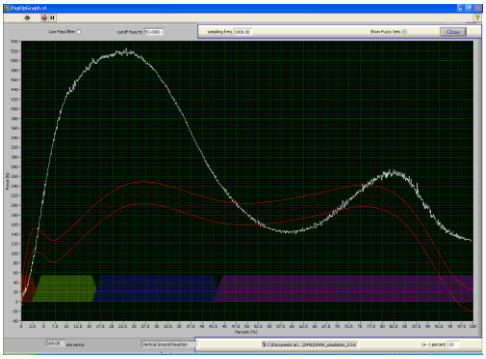

Too close, backed off for next.

Sim4

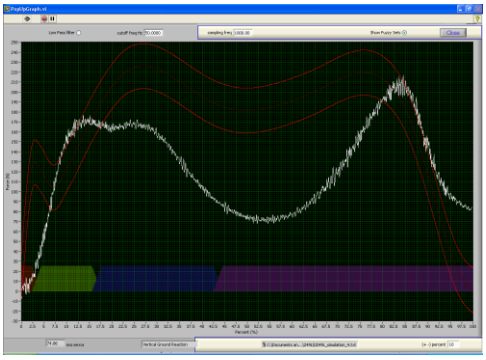

Sim5

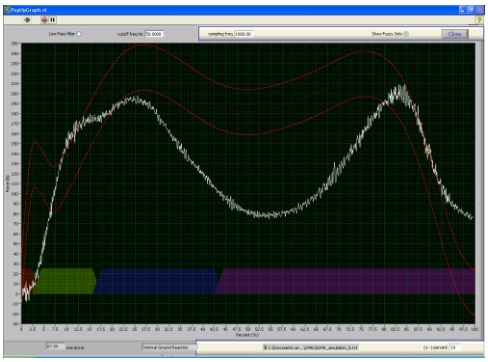

Sim6

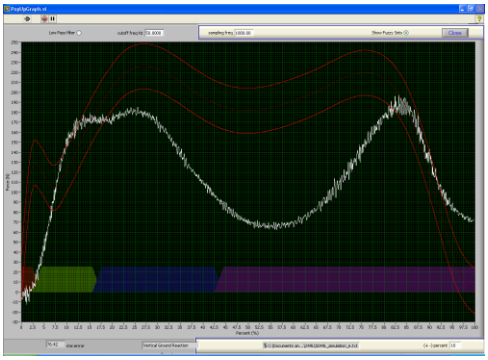

Sim7

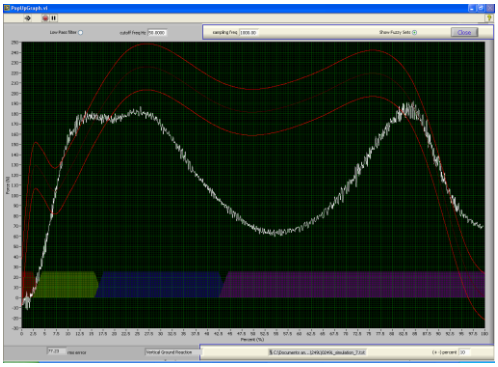

Sim8

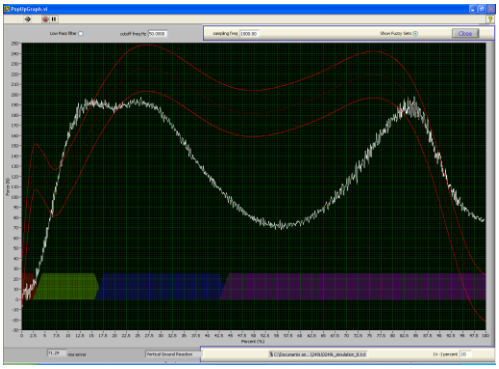

Sim9

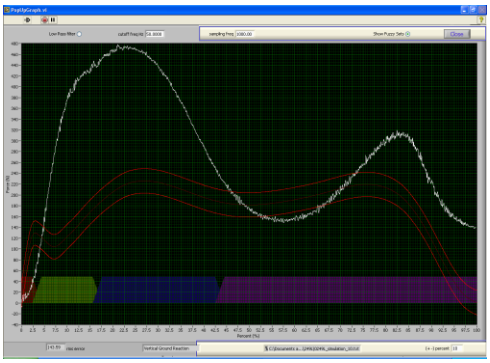

Sim13

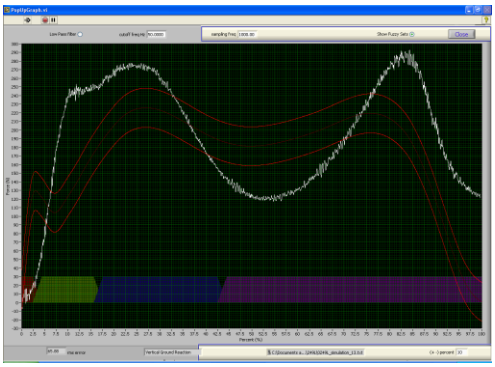

Sim10

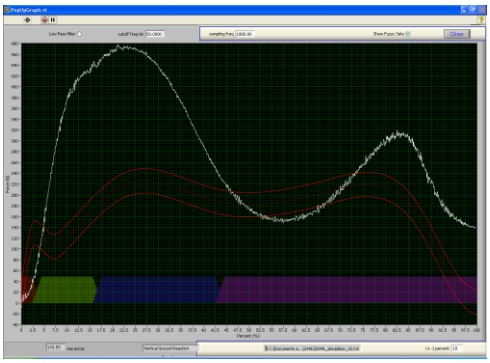

Sim14-Start IFLC set

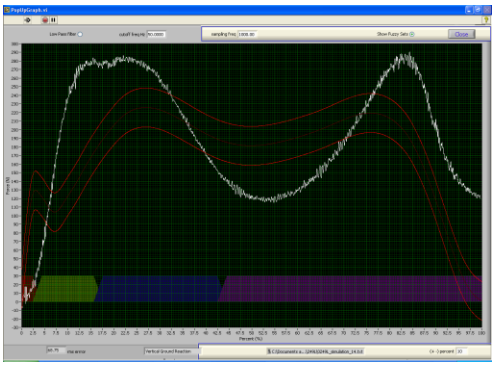

Sim11

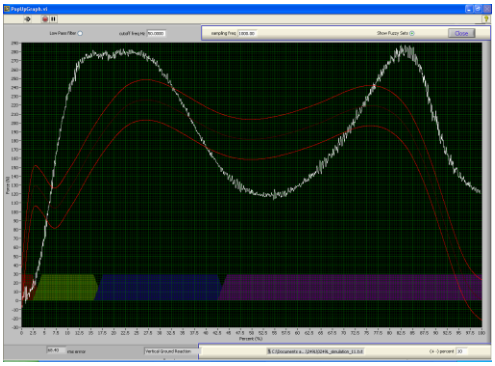

Sim15

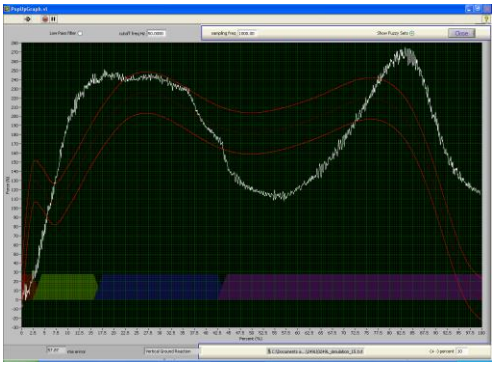

Sim12

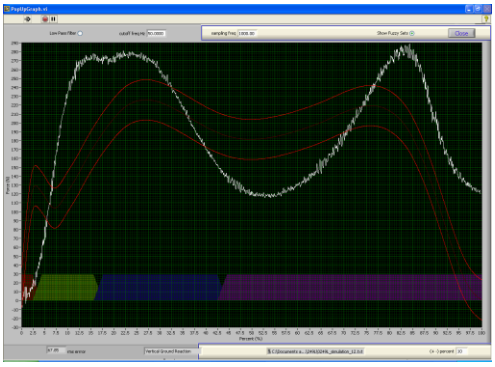

Sim16

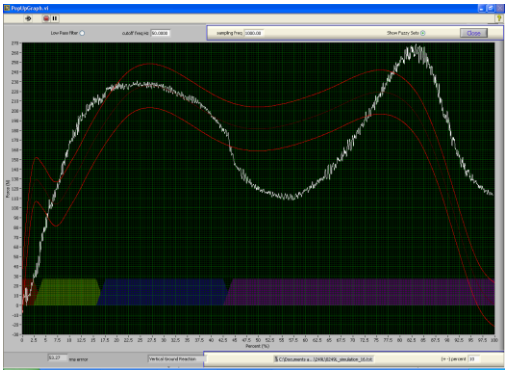

Sim17-Result from 14

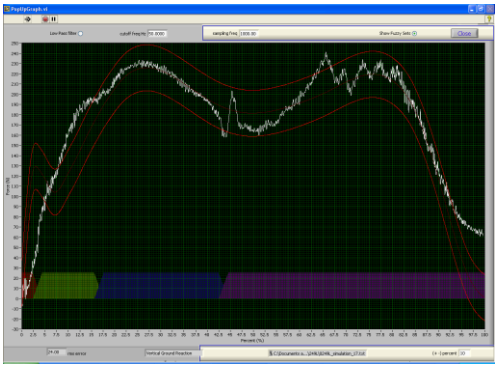

Slight discontinuity at start Achilles controller. Re-ran to see if improvement could be made.

Sim18-start IFLC set

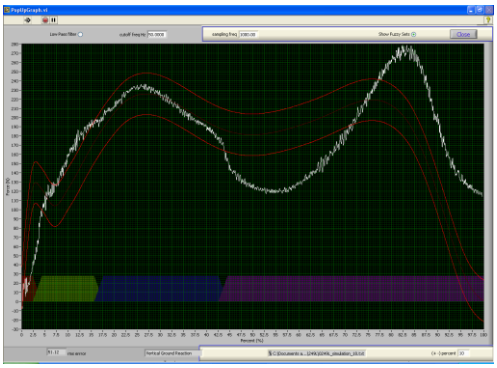

Sim19

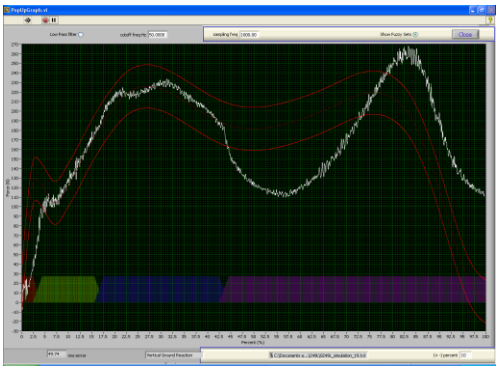

Sim20

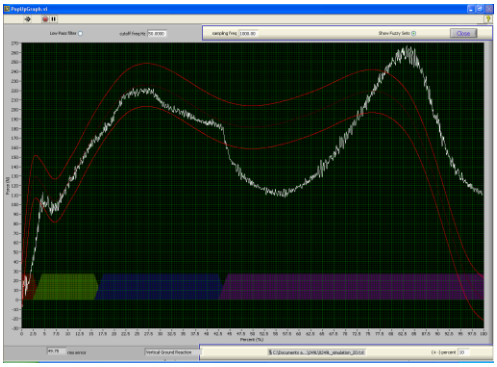

Sim21-result from 18 (kept data).

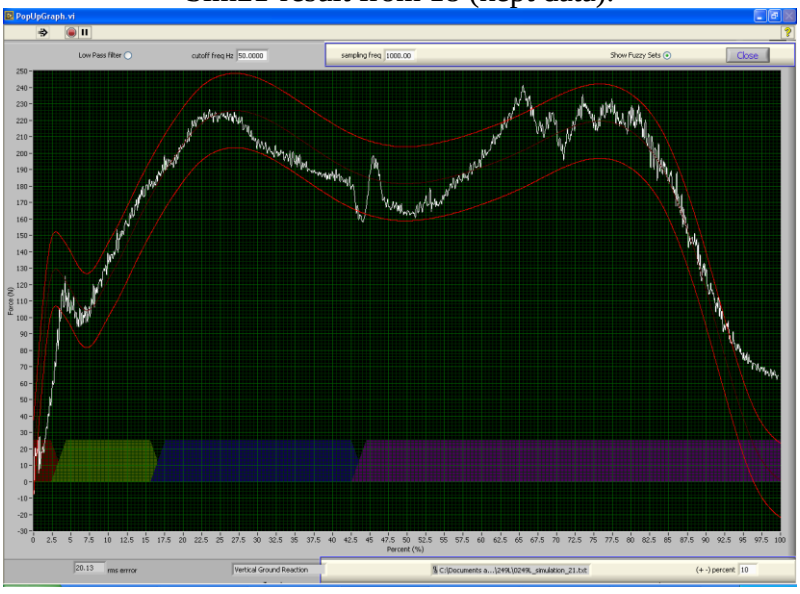

This RMS error was 8.90% (N/25%BW)

Example 4: 8308R (BW 801 N)
This foot was fused in a slightly plantar flexed position, making it quite challenging to match the target vGRF.

Sim4

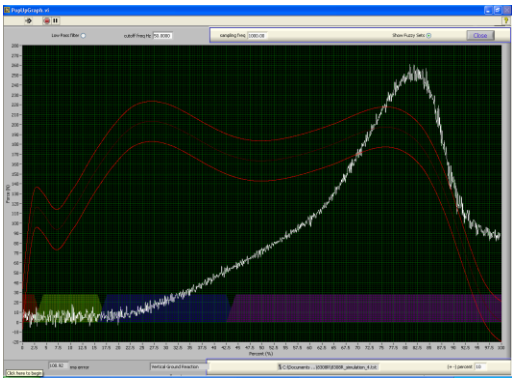

Bring closer to foot next.

Sim5

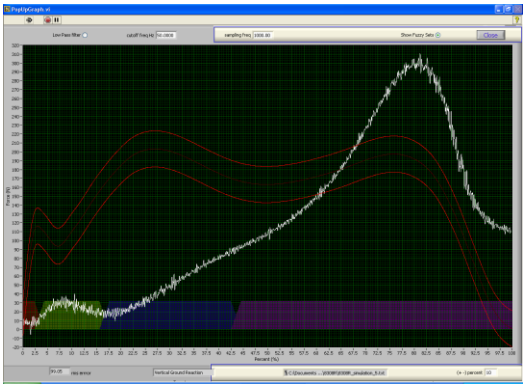

Bring closer to foot next.

Sim6

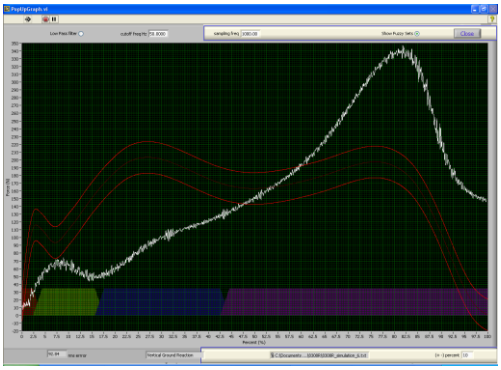

Bring in closer and lower Achilles gain.

Sim7

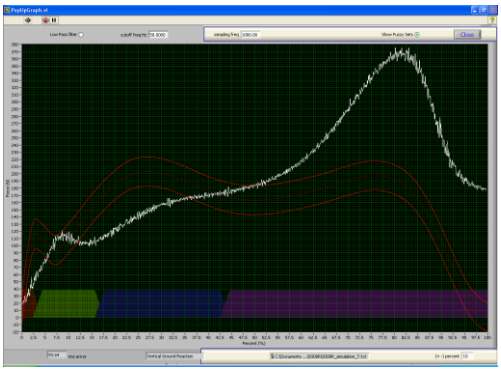

Sim8-Start IFLC set.

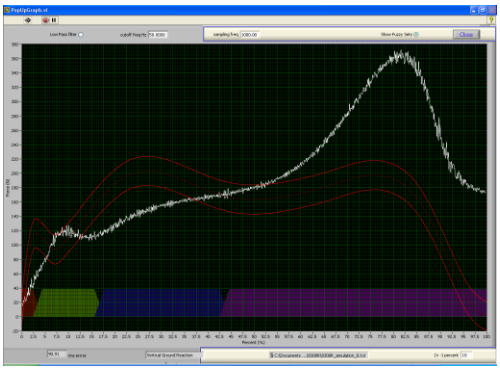

Sim9

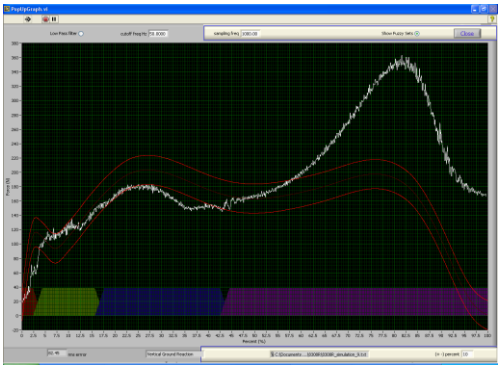

Sim10

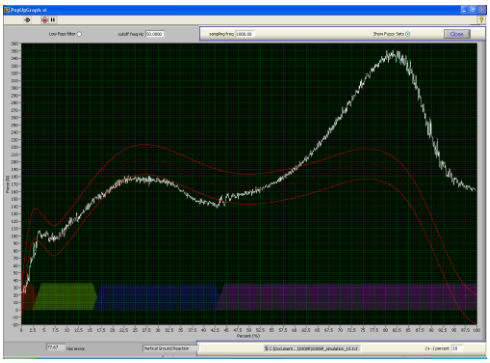

Sim11-Result from 8.

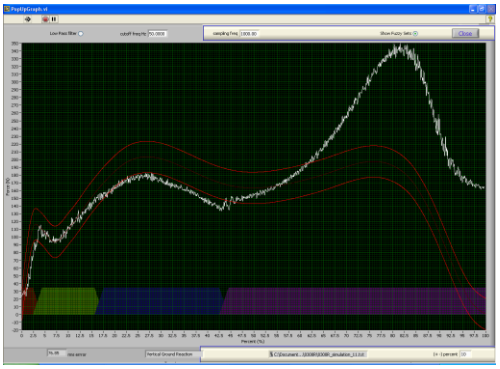

Do another iterative set next to try to bring up force from 0-40%.

Sim 12-Start IFLC set

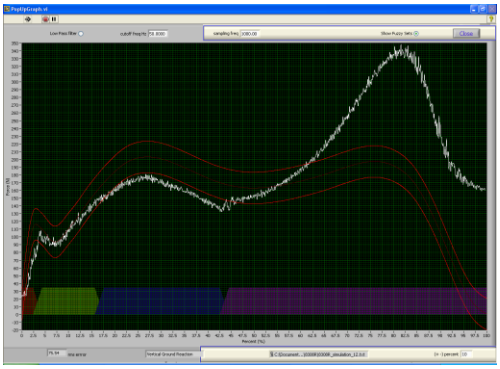

Sim13

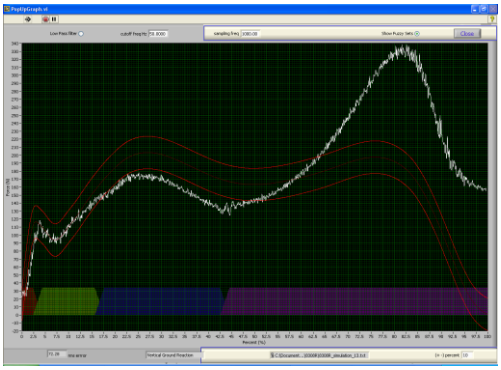

Sim14

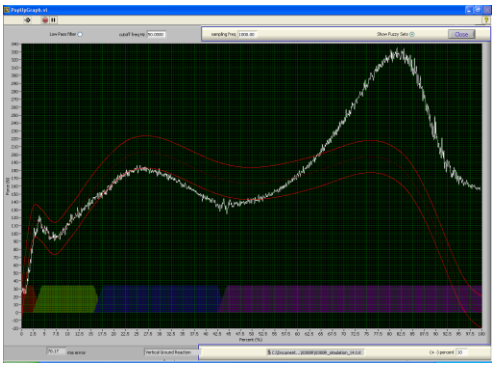

Sim15-Result from 12.

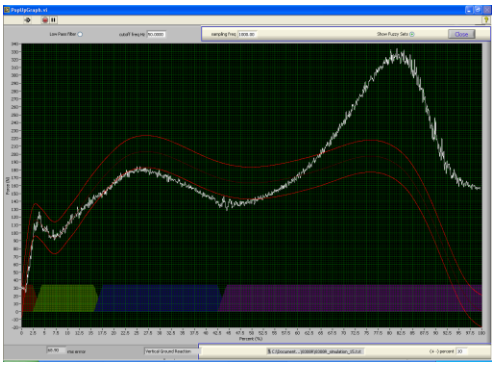

Bring force plate closer to foot next, iterate again

Sim16-Start IFLC set

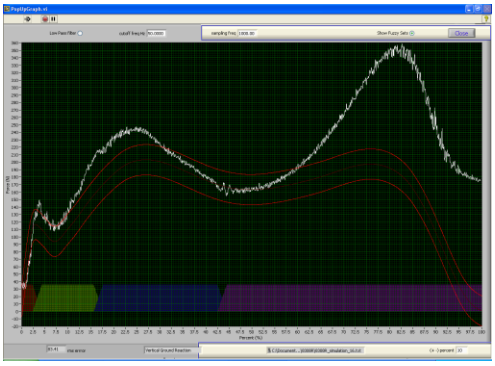

Sim17

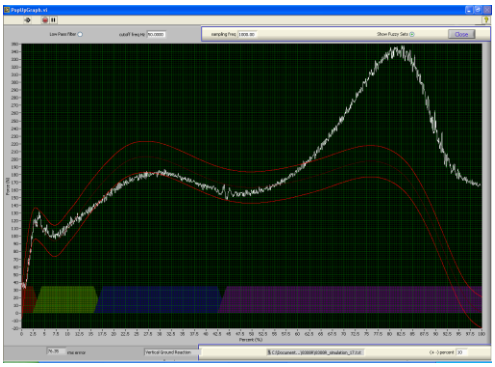

Sim18

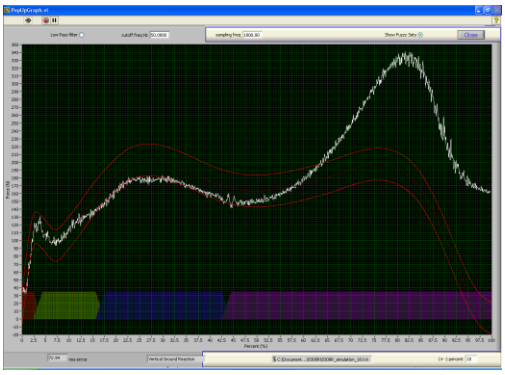

Sim19-result from 16

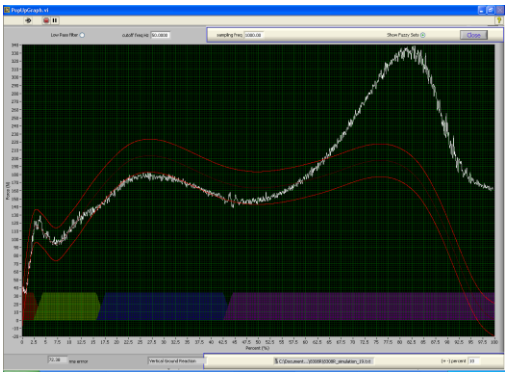

Delta-x controller overshot bringing force down. Redo iterating on traj 15, with lower IFLC gain next.

Sim20-Start IFLC set (2 precondition trials)

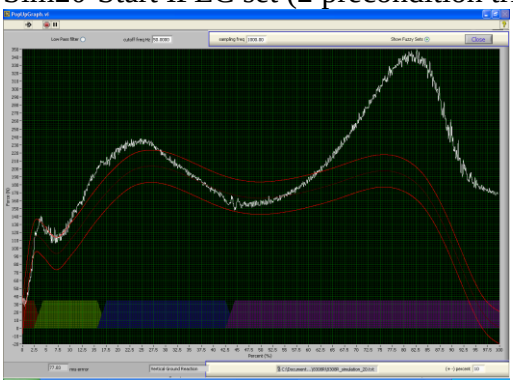

Sim21

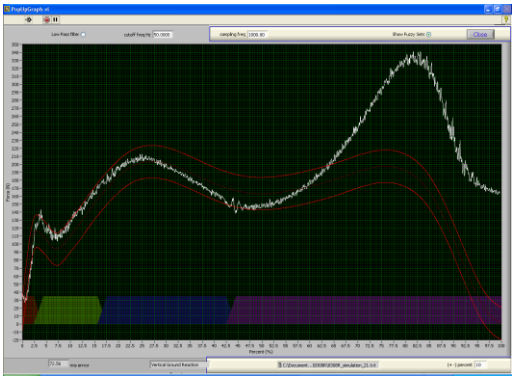

Sim22-result from 20.

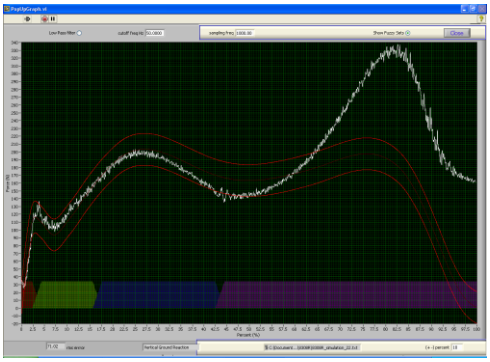

Sim23-start IFLC-see if this is close enough.

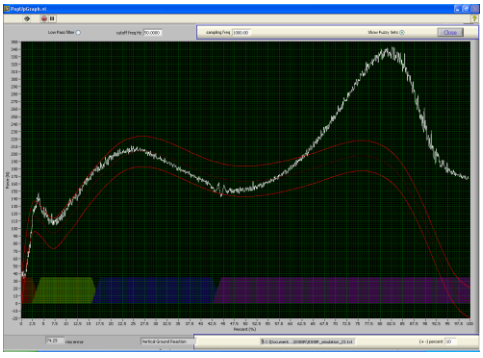

Sim24

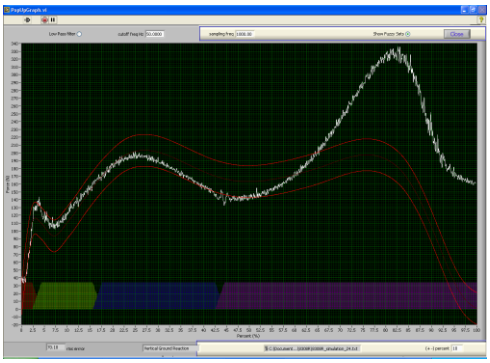

Sim25

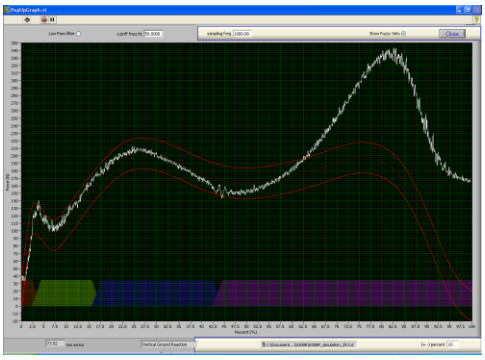

Sim26-result from 23.

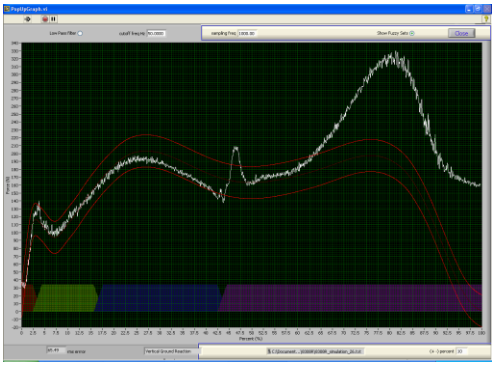

The discontinuity at 40% was found to be due to the difference in the trajectory from the changes made by the delta-x controller before 40% stance phase. We decided iterating more would not make this better, so we started over from the original trajectory.

Sim27-starting over

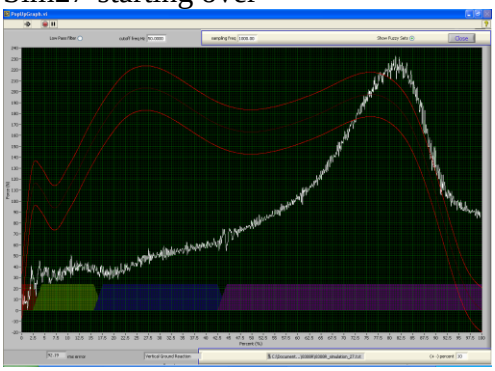

Sim28

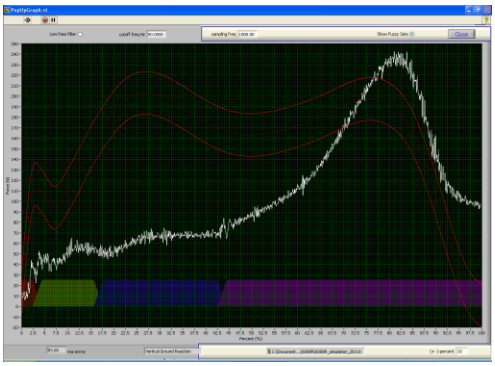

Sim29

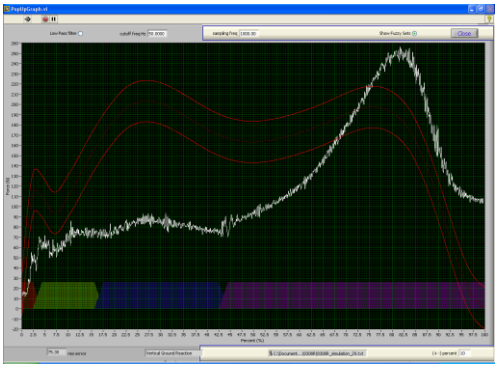

Sim30-Start IFLC with 1 preconditioning trial

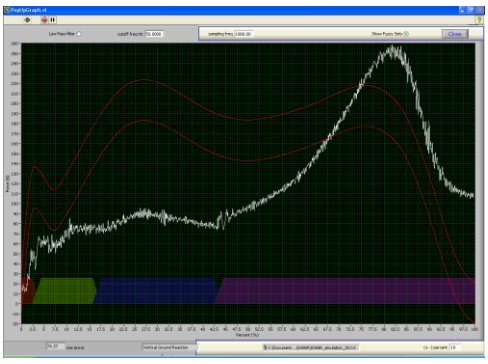

Sim31-Result from 30.

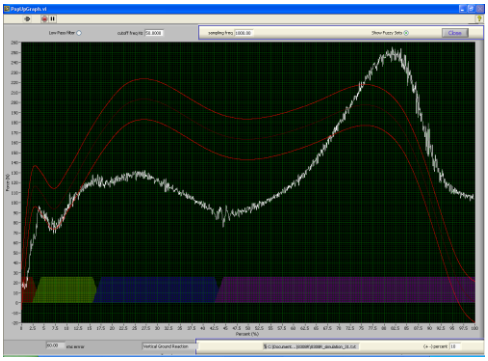

Sim32-Start IFLC

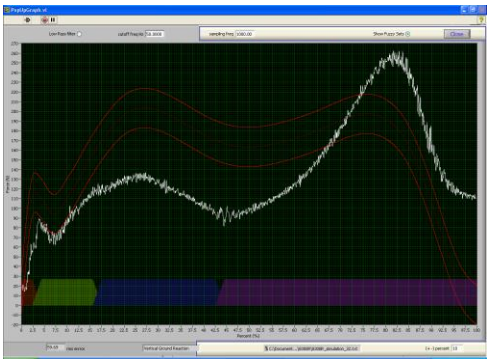

We are trying to get the delta-x controller to bring up the vGRF from 0-40% stance phase. The IFLC gain was probably 6-7.5 (don't remember exactly) to get the controller to increase the vGRF Notice the second peak not overshooting the target nearly as much. This is better starting point.

Sim33

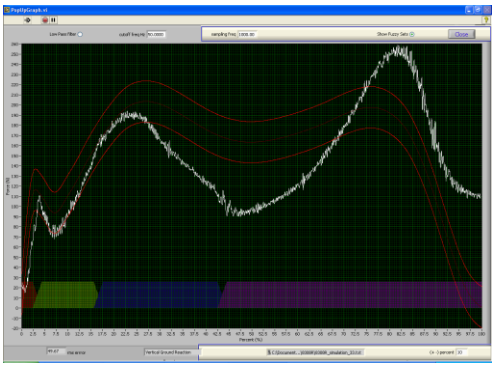

Sim34

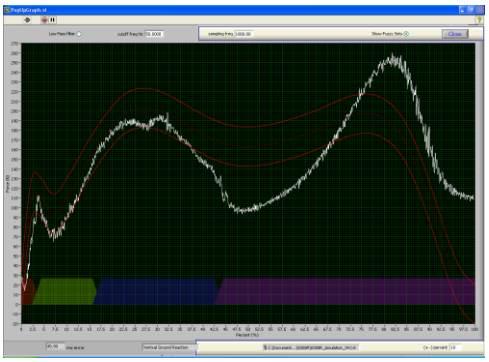

Sim35-Result from 32.

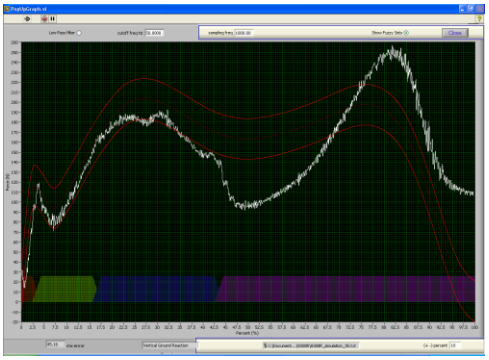

Getting better

Sim36

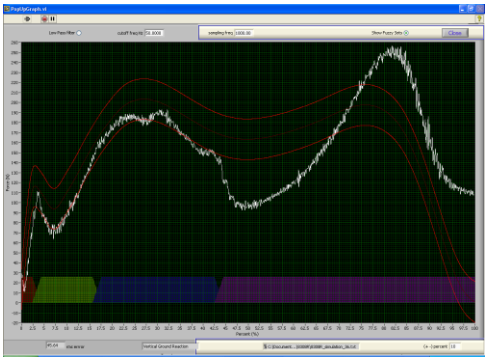

Sim37

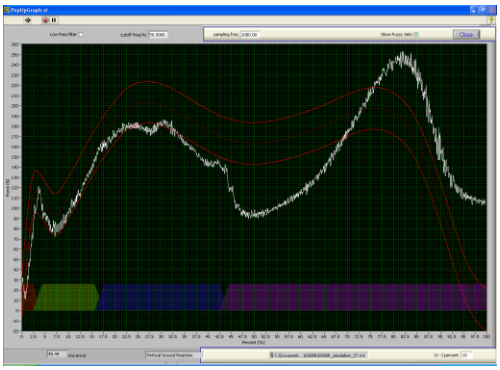

Sim38

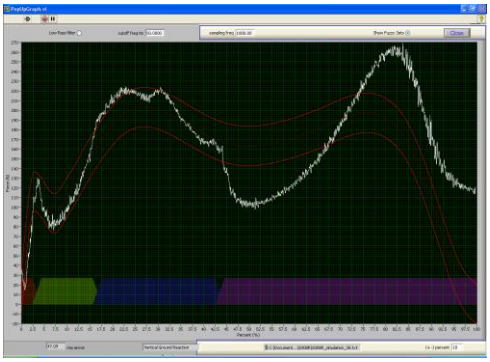

Sim39-Start IFLC set

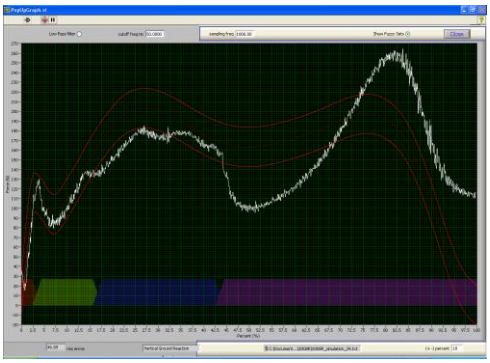

Sim40

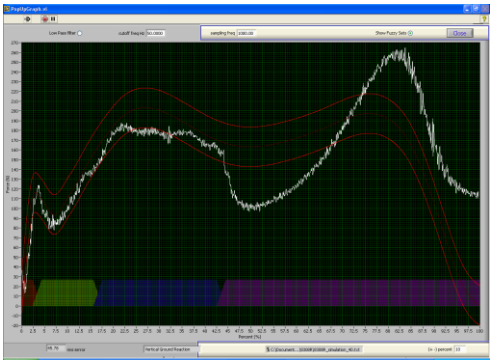

Sim41

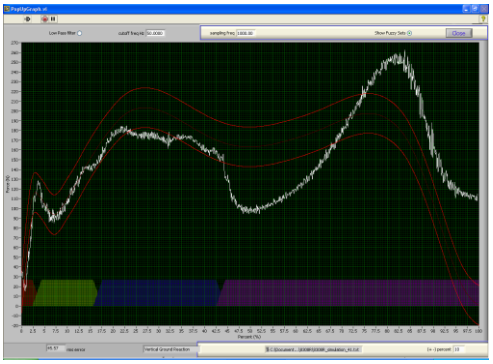

Sim42-result from 39.

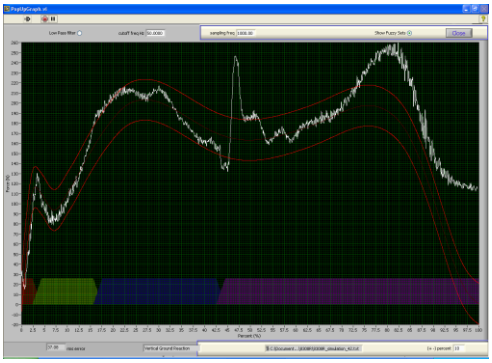

Notice discontinuity as Achilles controller turns on. Second peak is getting better though. Brought force plate away from foot, started another IFLC set next.

Sim43-Start IFLC set.

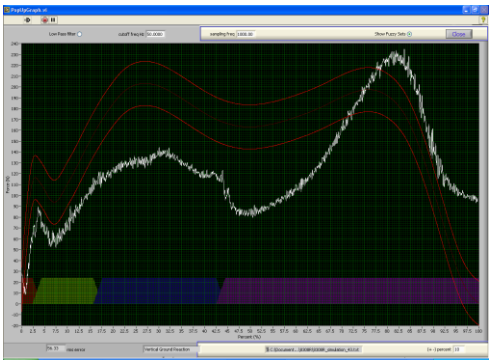

Sim44

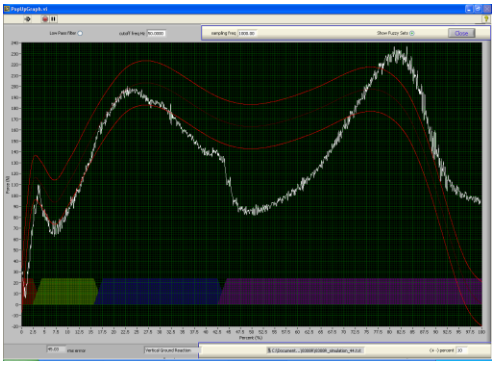

Sim45

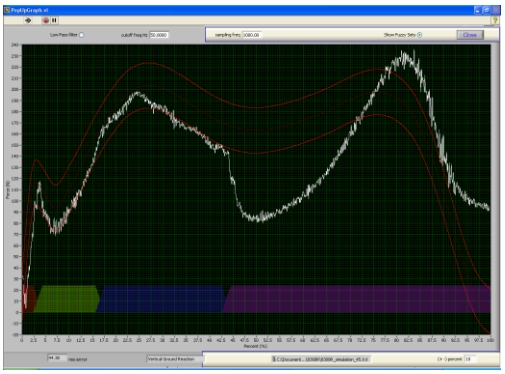

Sim46-Result from 43 (no Achilles fuzzy controller on).

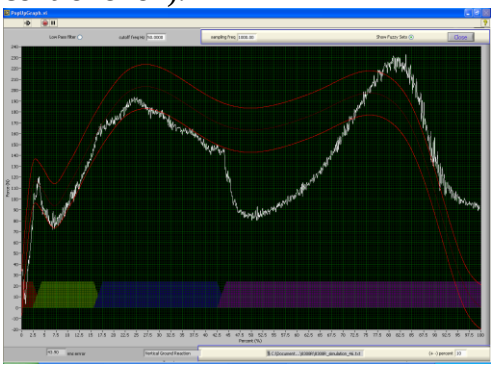

Too low at Achilles controller transition, iterate again next from this trajectory.

Sim47-start IFLC set.

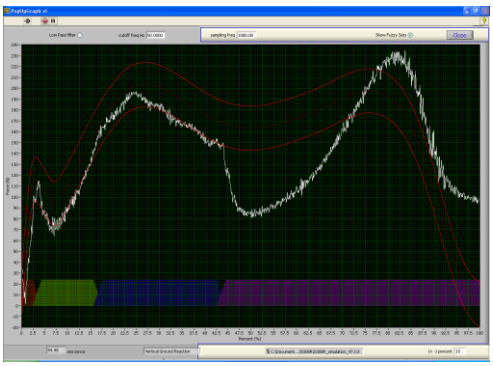

Sim48

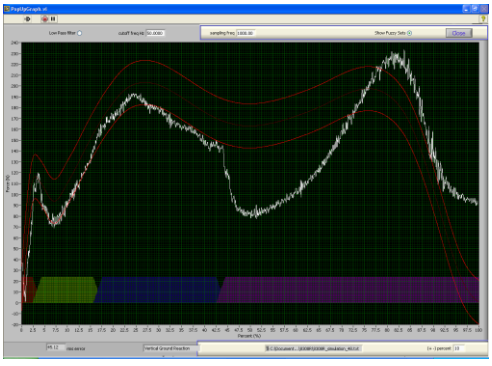

Sim49

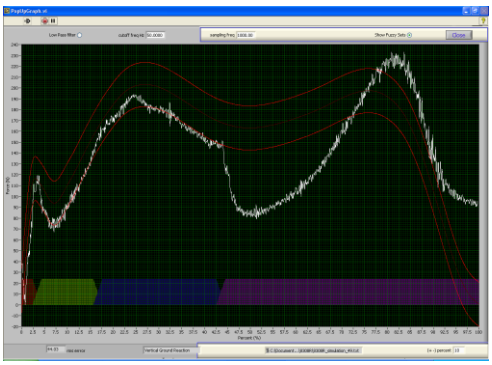

Sim50-result from 47.

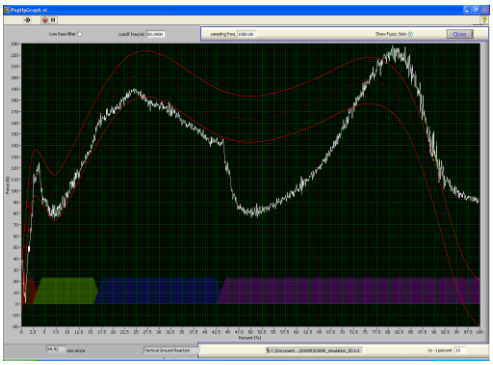

Not much change. Brought force plate closer to foot.

Sim51

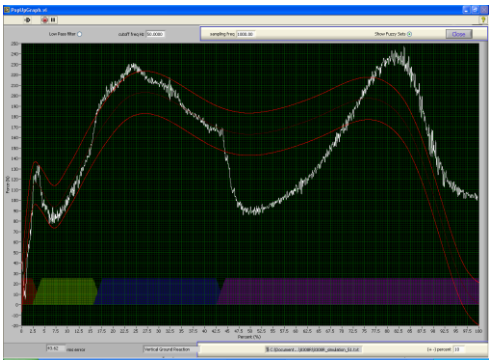

Sim52-start IFLC set (5 preconditioning).

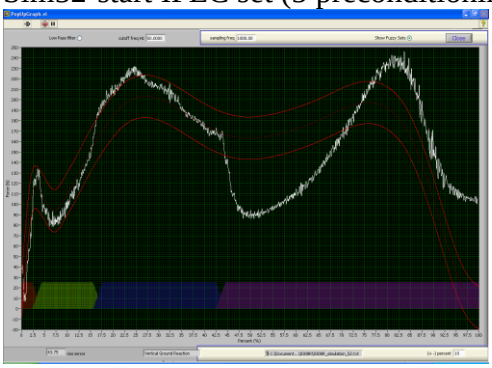

Sim53

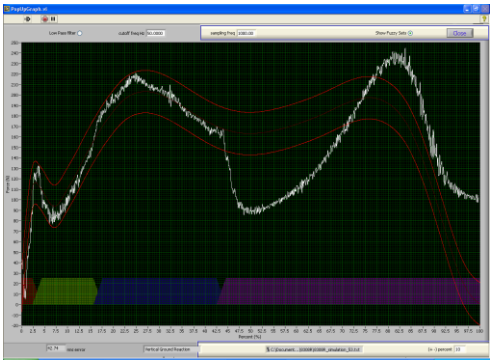

Sim54

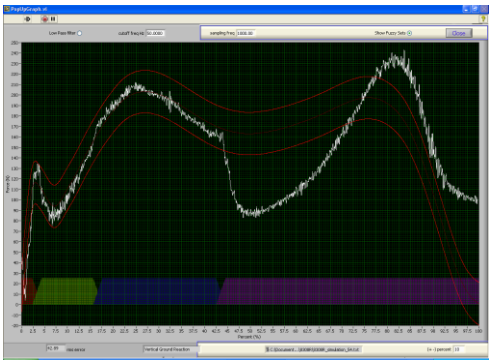

Sim55

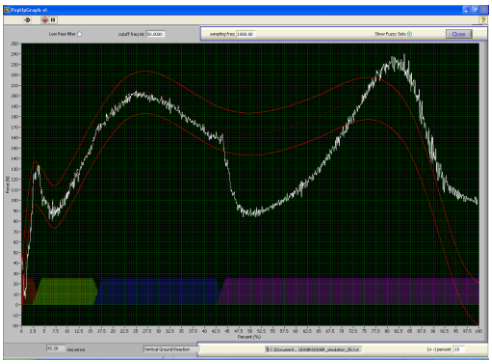

Sim56-Result from 52.

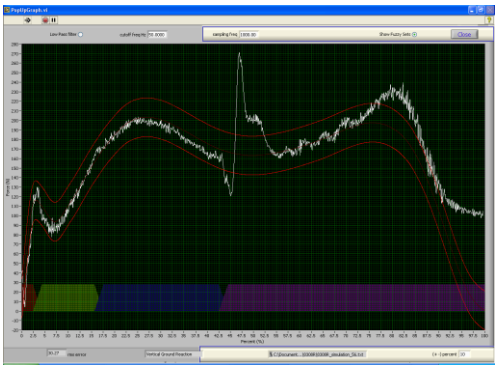

Still too low at transition to Achilles controller. Bring force plate closer to plate slightly next, again.

Sim57

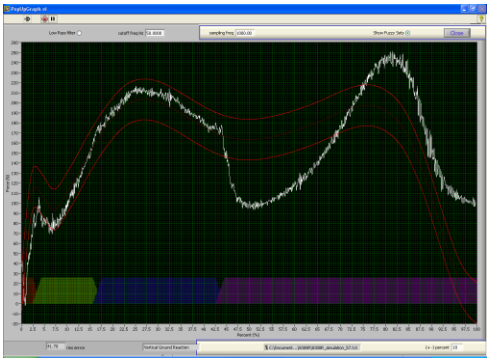

Sim58

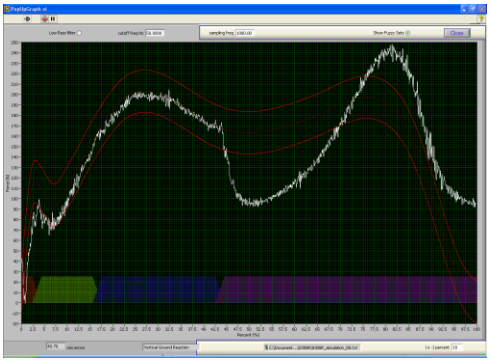

Sim59-Start IFLC set

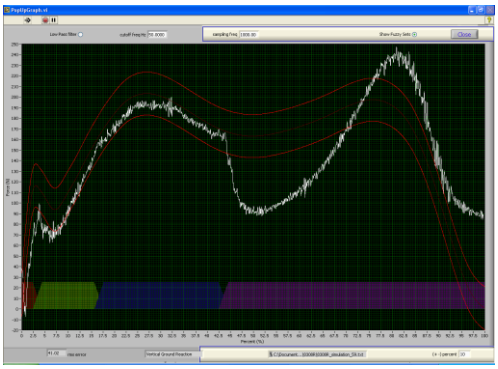

Sim60

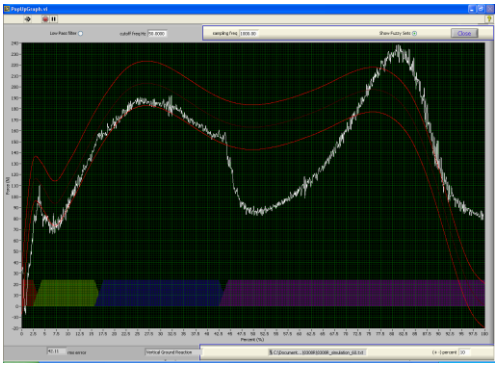

Sim61

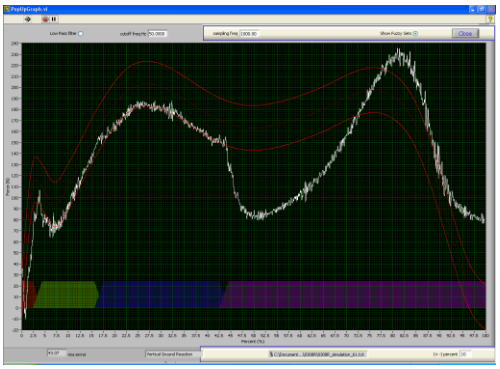

Sim62-Result from 59.

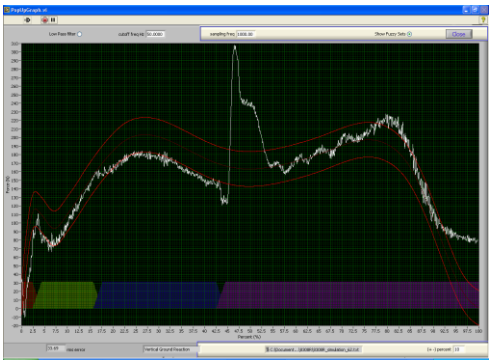

Sim63-Start IFLC set.

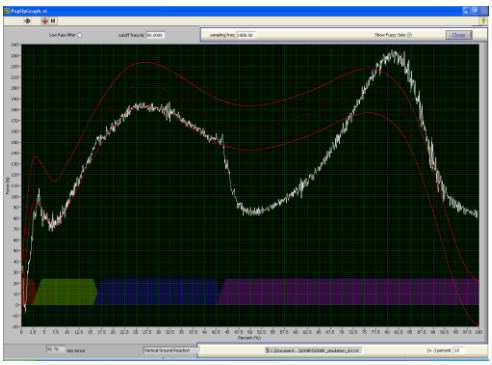

Sim64

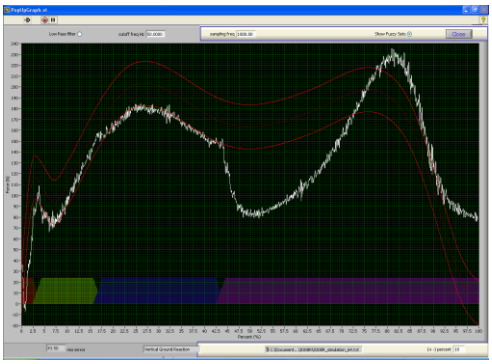

Sim65

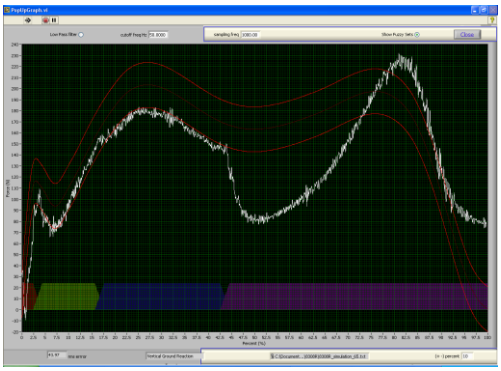

Sim66-Result from 63.

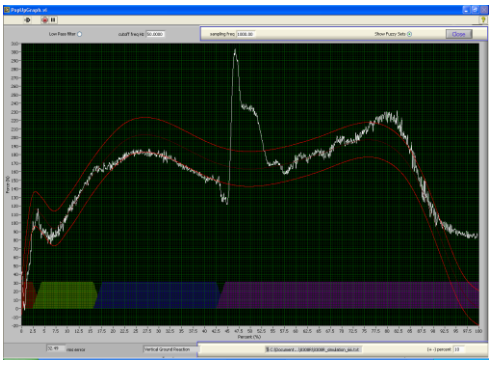

Sim67-Start IFLC set

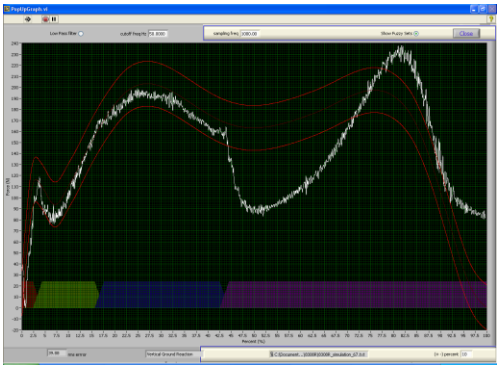

Sim68

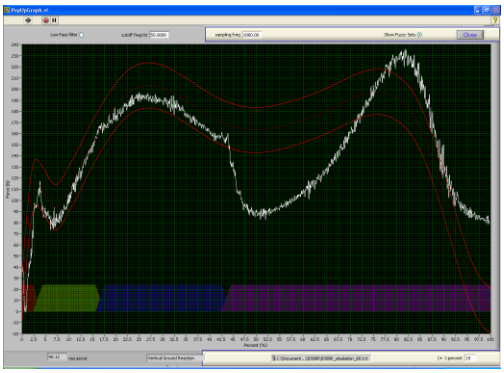

Sim69

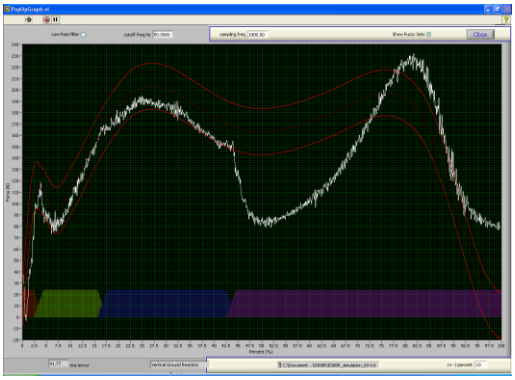

Sim70-Result from 67.

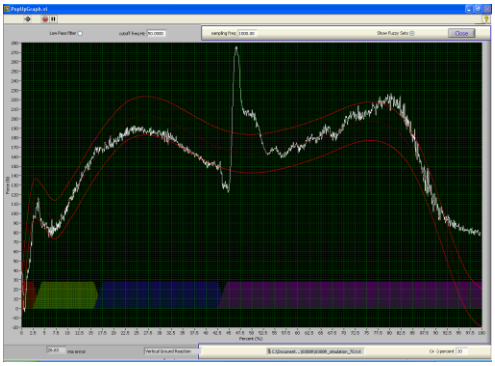

At this point we started changing Achilles gain. For all prior trials we had run the Achilles tendon at 0.02, in attempt to bring down the vGRF at the second peak. This very low force on the Achilles just before the fuzzy controller turned on made the discontinuity at the Achilles controller transition much larger. We changed the Achilles gain to 0.10, and it had very little effect on the second peak vGRF, but as you can see in the next few plots, the Achilles fuzzy controller was much more stable. Conclusion: try run the Achilles at 0.10 gain for fuzzy sets if there is a discontinuity in the vGRF at 40%.

Sim71

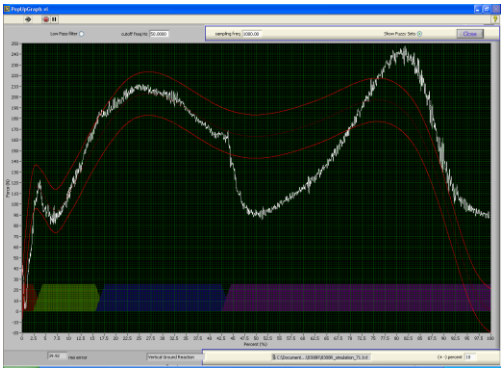

Notice how the second peak is not very much higher with the increase in Achilles gain. This means that the second peak force is being governed more by the plate motion than the Achilles tendon force plantar flexing the foot.

Sim72

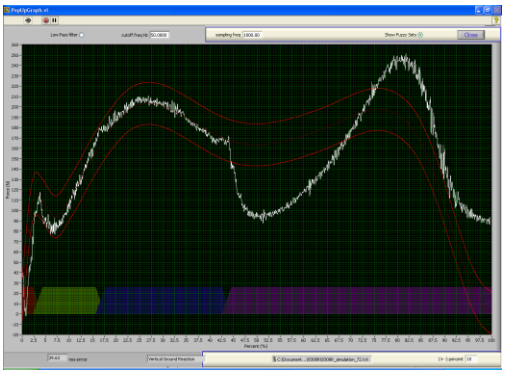

Sim75

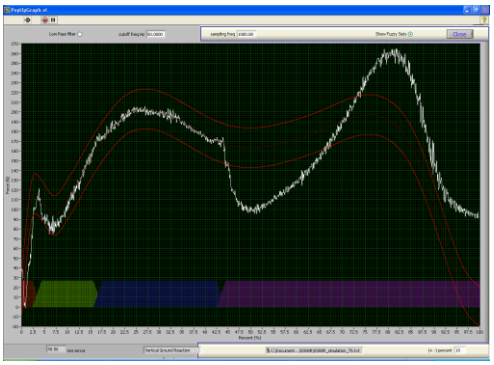

Sim73

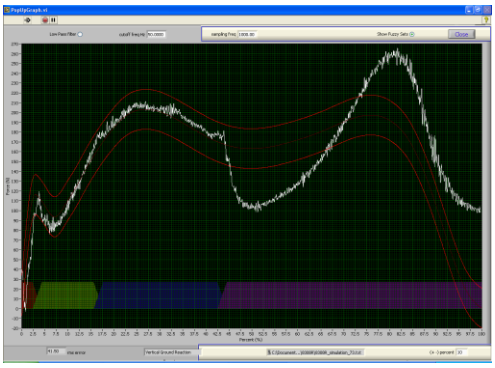

Sim76

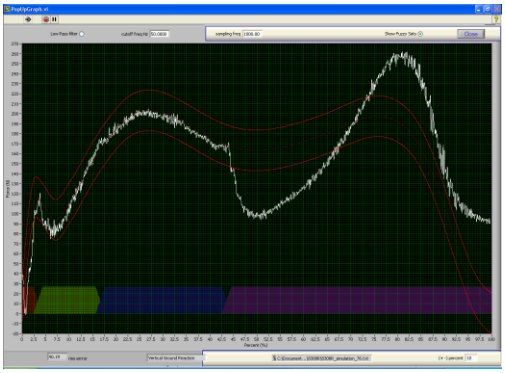

Sim74-Start IFLC set

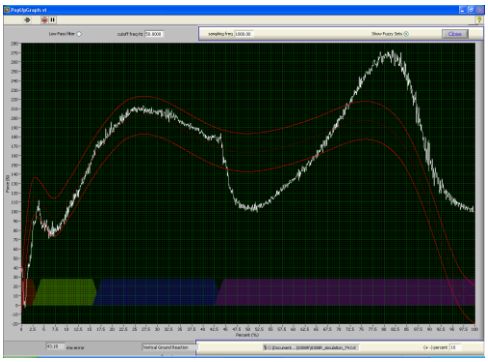

Sim77-Result from 74.

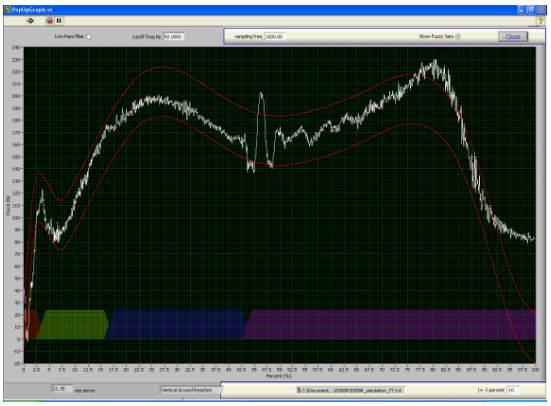

Kept data. This corresponds to 10.56% RMS error (N/25%BW). Even though this is beyond the desired threshold of error, the vGRF got slightly better as the day went on, and this single specimen being over 10% was balanced and averaged out by having better vGRF data on other specimens, resulting in a total RMS error below 10%, which is the only value we are reported in the paper for GRF that we are controlling.

B.9: Potential Future System Improvements

If the problem of major discontinuity at the transition from the delta-x to Achilles force fuzzy controller persists, one possible solution could be changing the membership values of the control systems to having a full overlap between the Achilles and delta-x controller. As seen in Figure B.15 (from page 90 of Patrick Aubin's Thesis), there is a transition where the midstance controller membership value decreases as the late stance controller's membership value increases (42-44%). Instead, the late stance controller could increase to a value of 1.0 before the midstance controller starts to decrease in value. This could cause issues for the fuzzy-controller functions in Labview, so another implementation would be to add a fifth membership function ("midlate stance") from around 38-42% where the delta-x and Achilles fuzzy controller are both on, to limit this discontinuity.

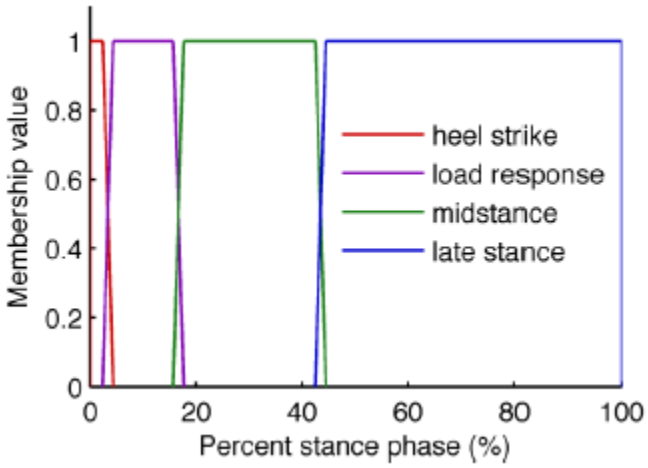

Figure B.15: Membership functions for the four control regions over stance phase. Heelstrike-TA Fuzzy only, Load Response-TA Fuzzy and delta-x iterative, Midstance-delta-x iterative only, Late Stance-Achilles Fuzzy only.

APPENDIX C: Pliance Data Analysis Program Manual

C.1 Introduction

This appendix will describe the custom Matlab program written to allow for the pliance data to be aligned with a fluoroscope image of the specimen, putting the center of pressure (COP) in an anatomically relevant coordinate system, and allowing for the maximum pressure in ten regions of interest to be determined, while also dramatically reducing post-processing time for the user, in comparison to the novel software.

C.2 Obtaining full foot radiograph.

The first thing needed for this analysis is a loaded fluoroscope image of the specimen. This image must be taken at an angle directly down the axis of the tibia (supeoinferior) with foot loaded to 25% body weight in a neutral or slightly dorsiflexed position, allowing the posterior portion of the calcaneus to be seen in the image clearly (Figure C.1). A scale-bar is added to the image as well, to determine the actual size of the foot. Distortion correction is applied to the image due to account for the distortion inherent with the fluoroscope. The image is distortion corrected before it is used with the code (Section C.3). Save the distortion-corrected image with the last 4 characters corresponding to the foot ID number and right/left designation (i.e. 0666L, 8315R).

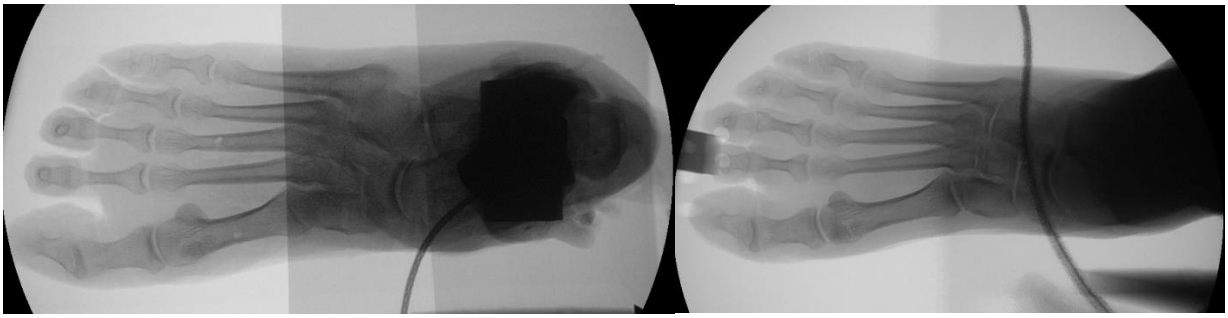

Figure C.1: (Left) A fluoroscope image down the axis of the tibia with the posterior calcaneus visible, (right) a standard AP foot fluoroscope image with no visible calcaneus.

C.3 Distortion Correction of Fluoroscope Image

Before the fluoroscope images are used in this program, a distortion correct is performed. Using a fluoroscope image of a plate with holes in known locations (Figure C.2), the images are corrected for both the pin cushion distortion from the lens of the C-arm and the "S" distortion caused by the effect magnetic fields on the II. Matt Kindig wrote a code to batch process these corrections that is outlined as follows.

1. Open *batch_crop_images.m*. Put the original images exported from the C-arm (including the calibration grid image) into a single file and copy the directory to *InDir* (line 1). Run the code. A cropped copy of the image should be created in the directory with the name appended with "_cropped".
2. Open *C_arm_calibration.m*. Change the directory and filename of the calibration grid in *im* (line 15) to the desired image of the calibration grid. For each image to be corrected, change the directory and filename in *realImage* (line 48) to the desired cropped image. The image will be corrected and another copy of the image will be created with the name appended with "_correctedCAL."

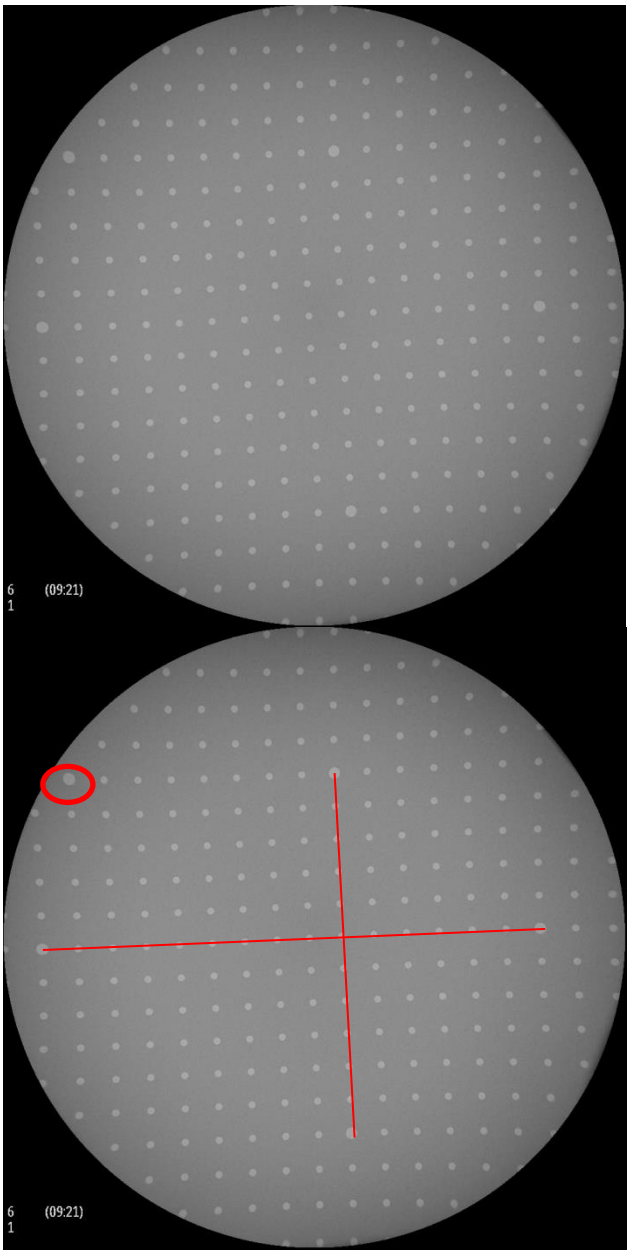

Figure C.2: Cropped distortion plate calibration image (left) and large holes identified that are used in the correction algorithm (right). Five large holes are needed to be seen in the image, including the four that make the cross pattern shown in the image.

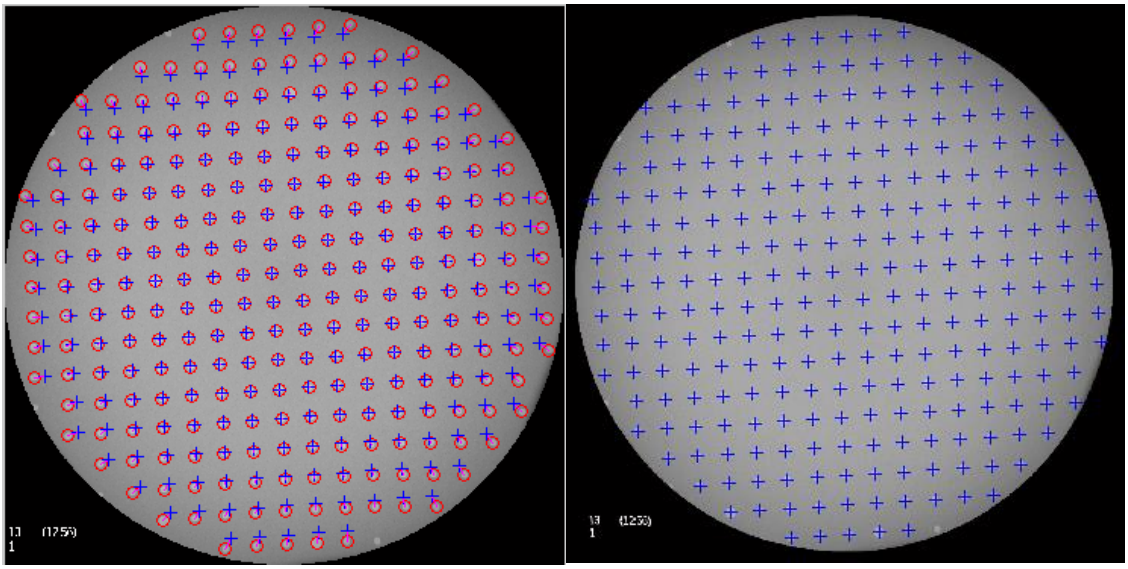

Figure C.3: Distortion correction of the calibration plate, with the circles showing there the holes are in the distorted image, and the blue crosses showing where the know locations of the holes are (left), and the distortion corrected image (right).

3. After the images are corrected, rename each corrected file with the four-digit foot number and letter (i.e. 0215R, 8300L) to use in the code.
4. Finally, if necessary rotate the image in Windows Photo Viewer or GIMP such that the toes pointed towards the top of the image (Figure C.4).

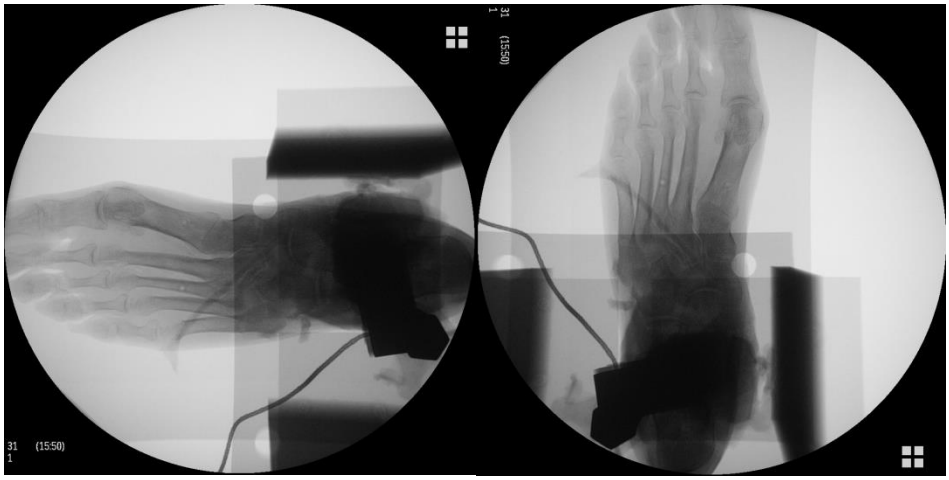

Figure C.4: The distortion corrected image, in its initial orientation (right) and after rotation in GIMP to have the anterior direction towards the top of the image (left).

C.4 Overview of Matlab Program

The data needed for this analysis is the pressure data file (for all sensors at all timesteps) saved as an .asc file. This data is stored on the pliance laptop by default at C:\novel\novfile\asciiout\pliance\ under the proper .mfg file made for that specimen.

The main Matlab program for this analysis is *Pliance_Analysis.m*. The code loads the fluoroscope image, and allows the user to align the second ray with the y-axis on a plot, move the origin of the plot to the most posterior point on the calcaneus, and change the size of the image to match either a scale-bar in the fluoroscope image, or to match the pliance max pressure plot itself. The user then identifies the ten regions of interest in the fluoroscope image, using a graphic user interface (GUI). The code reads in the .asc file of pressure data, calculates the COP, crops the trial to 4.092 seconds after the identified heelstrike (the time of a $1/6^{th}$ *in vivo* simulation), and plots the max pressure pattern over the fluoroscope image. The code allows the user to translate and rotate the pressure data to align it with the fluoroscope image of the foot. The transformed gaitline, and x and y center of pressure coordinates are saved to a text file named according to the specimen and simulation number, along with the transformations made to the fluoroscope image (rotation, origin, and size). The rotated gaitline results and changes to the image can be compared to other trials after the analysis is complete using *plot_COP_results.m*.

C.5 Step-by-Step Use of the Matlab Program

1. Open *Pliance_Analysis.m*. There are several parameters in the code that are changed in lines 30-60, before the analysis is started. First, under *imagefile* the full directory path and fluoroscope image name is copied (.bmp images are used, as exported from the C-arm/distortion correction software). For the first trial analyzed of a single specimen, set *run_number = 1*. If the pliance data are taken with the pliance mat in landscape orientation (the standard) in the novel software, set *orientation = 1*. Set *TxtFileNoAscii = 0*, unless the data are taken with an incorrectly calibrated mat, which a previous code to be run to convert the data from a 28x29 to a 32x32 mat (see *Convert_to32x32_novel_fixed_trials.m*). The variable *flipleft_to_right* flips the fluoroscope image. If the images are NOT flipped on the C-arm before export (i.e., they are mirrored), this variable = 1 for right feet, 0 for left feet. If the images are flipped on the C-arm before export, these values are switched. It does not make a difference, but keeping the method constant for each image in the study will make things easier for data processing. The code converts all data to appear as right feet in the images/pressure data. The variable *pliance_left_to_right* flips the pressure data in a similar way. This varyies based on the mat orientation, but is obvious if this parameter is incorrect, and once the correct orientation is determined, it is constant for the entire specimen. The variable *threshold_pressure* should be set to 1 if a data threshold is to be applied above the 40 kPa commonly used during pliance data collection/saving. If additional thresholding beyond the 40 kPa in the pliance software is to be applied, this value is assigned to variable *thresh_level* in the units kPa (all measurements below this value are set to zero). The

variable *input_Image_Sizex* does not need to be changed for the first run-through on a specimen, but is filled in with the desired image size as described later in the document. The variable *actual_scale* is filled in with the value of the scale being matched in cm (i.e., if a ruler 8.95 mm wide is being used as a scale bar, set this variable to 0.895).

There are several important sub-functions in the beginning of the code that are described here for future debugging or expanding of the program. The program first reads in the data and thresholds it, removing any measurements below the desired input (*threshold.m*). The code then calculates the x- and y-coordinates of the center of pressure at each timestep (*calc_COP_mat.m*), then crops both this calculated COP data and all of the rest of the pressure data to the length of the trial (*crop_trial.m,* called within *calc_COP_mat.m*) using the total force measured by the mat to determine heelstrike. A trial-length of 4.092 seconds is hard-coded into *crop_trial.m*, which must be changed if anything besides 6x slower testing is used. The code plots vGRF figure (Figure C.5), where the total force vs. time and the portion of the data determined to be the trial are shown. This should be visually confirmed to be correct for each trial (i.e., confirm the green portion of the graph is about 4 seconds, if the cropped trial is off by more than 0.02 seconds, a warning will be displayed in the command window). Based on the sampling rate of the pliance system being much lower than the force-plate, the cropped trial length for the pressure data is not necessarily be 4.092, but it should fall between 4.07 and 4.11 seconds if the system was working correctly during data collection. If the trial length is found to be outside this range, the trial must be examined individually to determine the problem. After the COP is calculated the code continues to image manipulation.

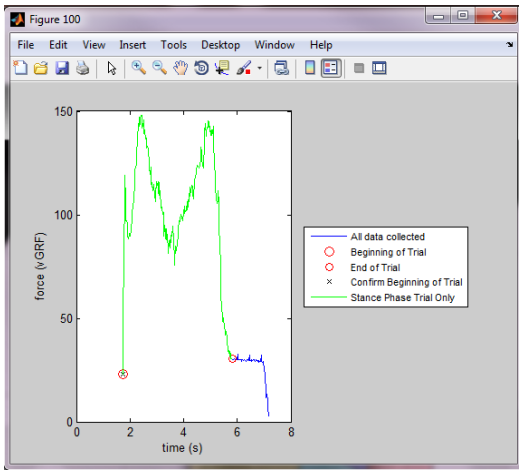

Figure C.5: The first output from the program plotting the calculated vGRF vs. time, with the trial cropped plotted in green.

2. Run the code *Pliance_Analysis.m*. Select the trial of interest (.asc file). Two figures pop up, and the code pauses. In the second ray alignment figure, a fluoroscope image is displayed along with a line (Figure C.6). The line is interactive and can be moved and rotated. Drag the line to align such that one end is on the posterior calcaneus and one end is at the head of the second metatarsal. Once the line is in position, right click and on the line and press copy position. Go back into the code and paste (CTRL+V) in the beginning of the code in variable "*line_input*". This is a 2x2 matrix with the values of the line in it. The initial pliance plot figure shows the pliance data. The user ensures that the calculated COP line is over the max pressure pattern of the foot. (Note: the transformation flipping the pliance data is not implemented in this figure, so whether or not the foot displays as right or left does not matter yet). Click in the command window and press any key to continue to the code.

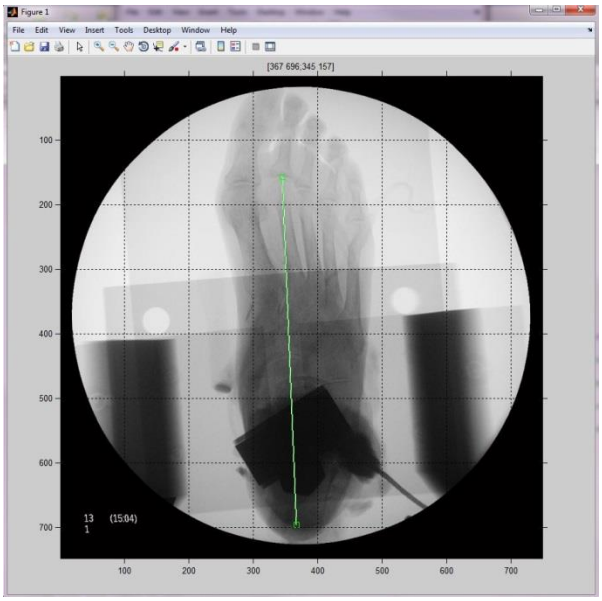

Figure C.6: The line in the second ray alignment figure is aligned with the posterior calcaneus to the head of the second metatarsal.

3. Next, the translational alignment figure will be plotted (Figure C.7). First, check to confirm the fluoroscope image is now oriented such that the line between the calcaneus and second metatarsal is parallel with the y-axis. There is also another line that can be moved in the image. Move the line such that the lower end of the line is at the calcaneus. Again, right-click and copy position, and paste the values in variable *"line_trans_input"*. This puts the origin of the figure at the posterior end of the calcaneus. Again, click in the command window and press any key to continue the code. Note for both of these interactive lines, if *run_number* = 1, the value is taken directly from the graph, if *run_number* = 0, the value is taken from the matrix pasted into the code, thus the line should not be moved after the values of the line are copied and pasted, for both figures.

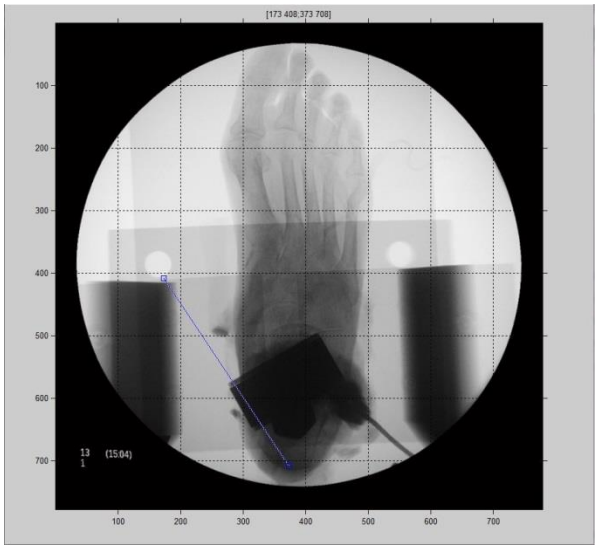

Figure C.7: The line in the translational alignment figure is moved to have one end over the most posterior point on the calcaneus.

4. The image rescale figure allows for the image size to be determined form a scale bar (Figure C.8). Again, an interactive line is used, and the line is be matched up with the scale bar of known length in the image. After the line is sufficiently "lined-up" with the scale bar, click in the command window and press any key to continue the code. A new value of *Isizex* is displayed in the command window. This value is copied and pasted in to the code, in variable *input_Image_Sizex*.

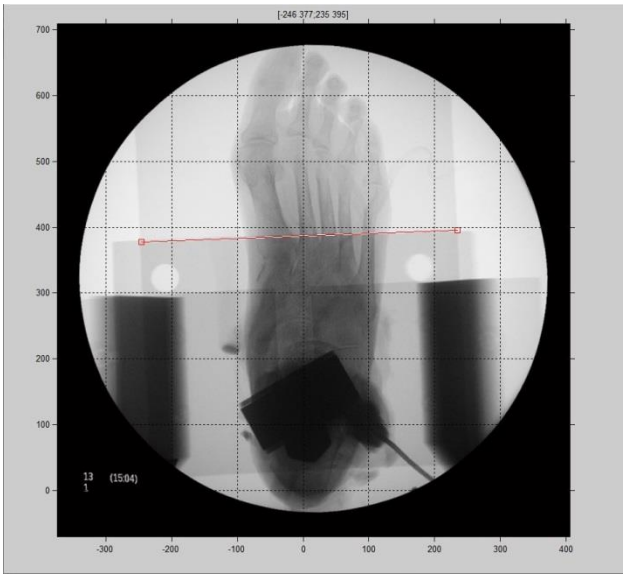

Figure C.8: The line in the image rescale figure is aligned with the scale-bar (in this example the width of the x-ray loading fixture was used, which, some would say this makes for a *less than ideal* scale bar).

5. The code plots two more figures. Ensure the origin of the figure is at the posterior end of the calcaneus (Figure C.9). In the following plot, make sure the pliance data and COP line are plotted in addition to the fluoroscope image (Figure C.10), and the pliance data shows up as a right foot (though the pliance data may be rotated 180 degrees).

Figure C.9: Check that the most posterior point on the calcaneus is at the origin (0,0).

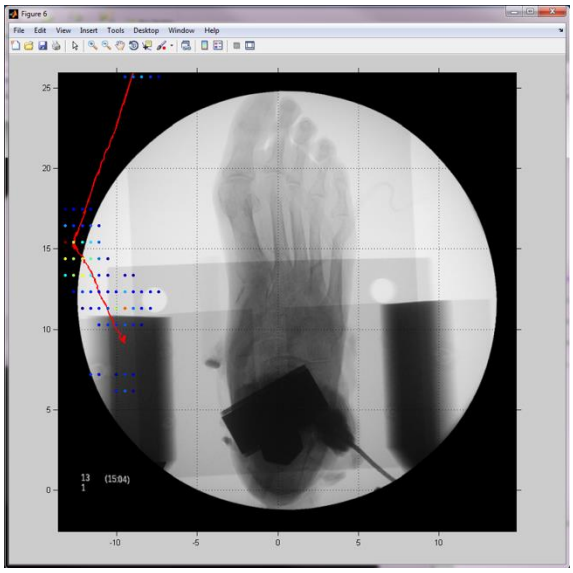

Figure C.10: A plot showing the pliance max pressure data and COP are aligned, and the pliance plotting as a right foot (although it is rotated 180 degrees in this image, that is alright).

6. The mask creation GUI will be plotted next. This GUI is used to identify the maximum pressure measured in ten regions on the foot. The plot should show a template of the foot regions over the top of the fluoroscope image. The template is manipulated to cover the exact region of interest.
    a. The regions of interest are as follows:
        i. Great Toe (hallux)
        ii. Lesser Toes
        iii. First metatarsal (Met1)
        iv. Second metatarsal (Met2)
        v. Third metatarsal (Met3)
        vi. Fourth metatarsal (Met4)
        vii. Fifth metatarsal (Met5)
        viii. Medial midfoot (cuneiforms/navicular)

ix. Lateral midfoot (cuboid)

x. Heel (entire calcaneus bone)

b. The regions are created using the *patch* function in Matlab, which creates a polygon out of vertices. To manipulate these shapes, the vertices can be moved, or additional vertices are added. To move vertices click the **Move Vertex** button, and start moving vertices to cover only the region of interest (Figure C.11). To add vertices, click the **Add Vertex** button, and click on the two vertices to have a vertex added between. The colored regions can be turned off and on to better visualize the fluoroscope image, by clicking the **Hide Masks** button. The Great Toe mask should be around the hallux and soft tissue. The Lesser Toes should incorporate phalanges 2 to 5, and the surrounding soft tissue. Each metatarsal mask should contain the bone of interest, and include the area out to the edge of the soft tissue for Met1 and Met5. The base of metatarsals 2 to 4 can be difficult to differentiate between, so estimating may be necessary (since most of the peak pressure will occur at the heads of the metatarsals, this is not a huge concern). The medial midfoot mask contains the area proximal to the metatarsal bases to the heel mask, and from the medial side of the foot to the lateral edge of the navicular. The lateral midfoot mask will contain the area distal to the calcaneocuboid joint up to the fourth and fifth metatarsals, and from the lateral edge of the navicular to the lateral side of the foot. The heel mask will incorporate the entire hindfoot posterior to the calcaneocuboid joint. The final mask will be used to determine the peak pressure in anatomically relevant regions (Figure C.12).

c. After the mask sufficiently matches the fluoroscope image, select **Save Masks**. This will write two .mat files with the foot name, *9999R_vertices_final.mat* and *9999R_faces_final.mat*. These file names should be added to the beginning of the code under variables *mask_vertices_file* and *mask_faces_file* to be re-used in subsequent analyses. Click in the command line and press any button to continue.

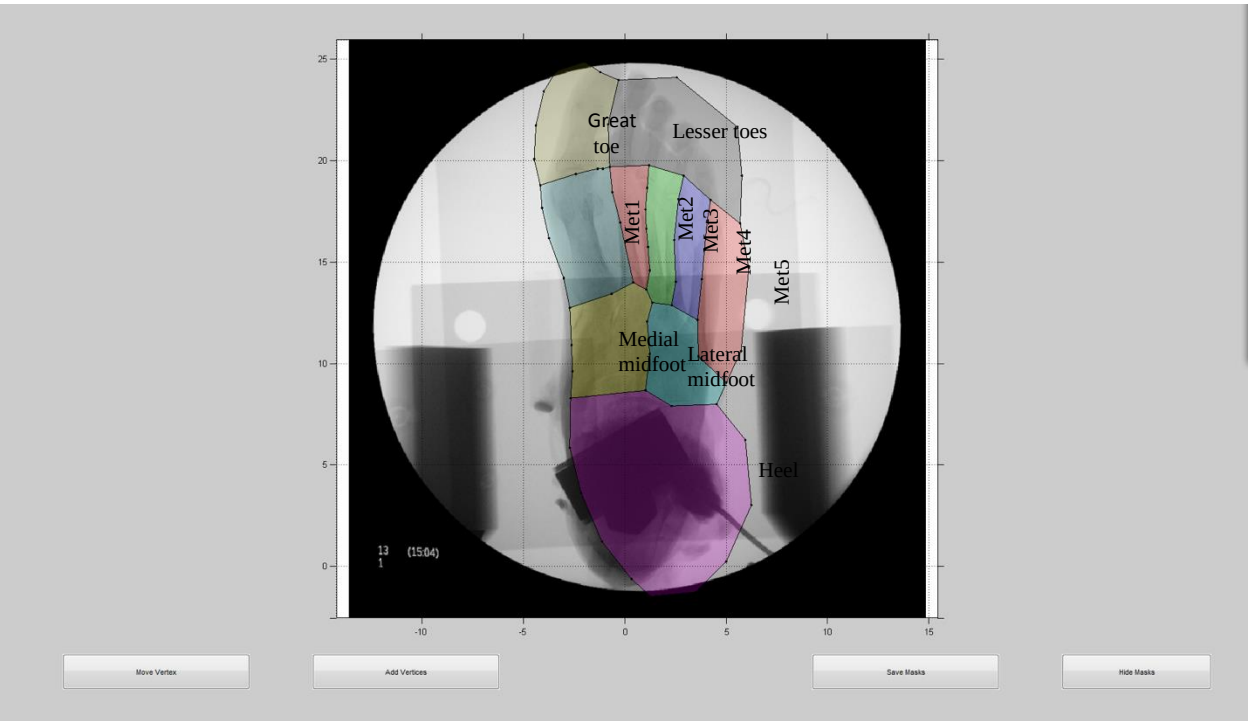

Figure C.11: Masking GUI with the template masks plotted over an example fluoroscope image, with the regions labelled.

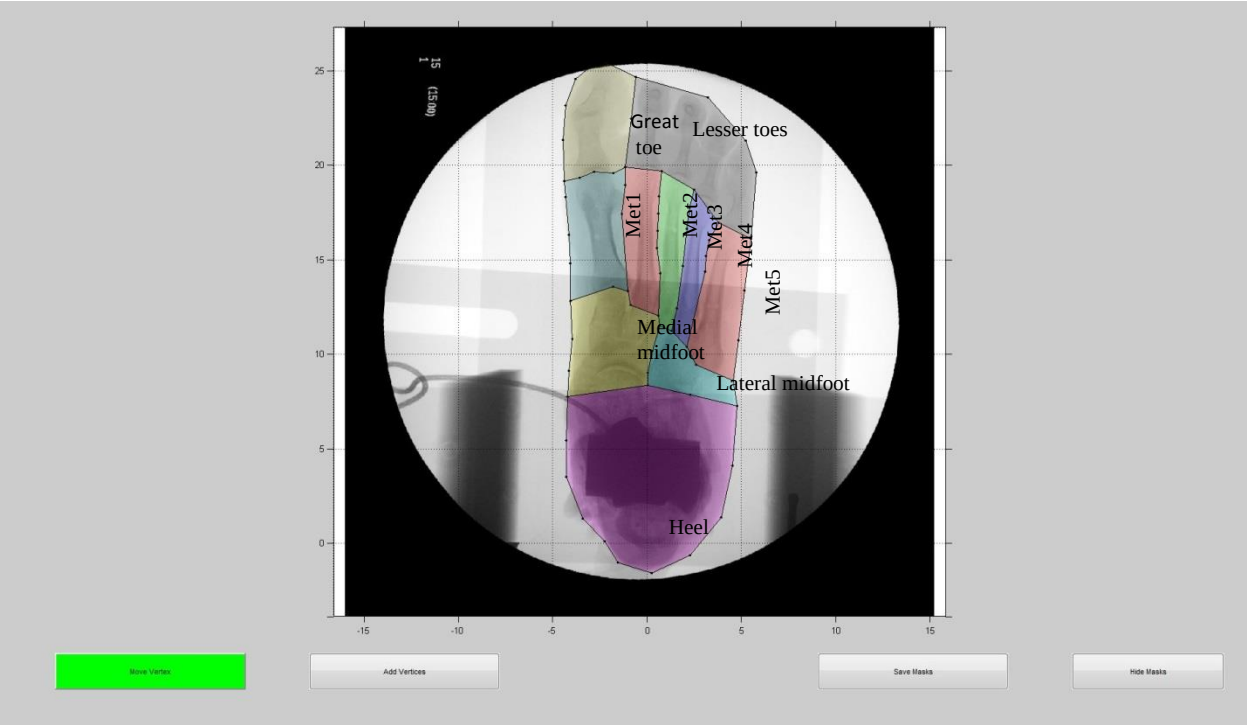

Figure C.12: Masking GUI after the masks are manipulated to cover the appropriate regions.

7. Next, the pliance registration GUI is plotted. This GUI allows for the pliance max pressure data/COP line to be translated and rotated to line up the data with the fluoroscope image. Operation of the GUI is as follows:
    a. To translate the data, click the **Translate Data** button. Then click on the gait line, and drag the gait line and pliance data to the desired position. If at first the gait line does not move when clicked, try clicking elsewhere on the line, as the click must be within a few pixels in order to initiate the motion. When the mouse is released, the GUI resets, and the Translate Data button must be clicked again to perform another translation.
    b. To rotate the data, click the **Rotate Data** button. This will display at red line and two circles in the data. Click on the red circle near the hallux and drag to rotate

the pliance data and gait line. Once the mouse is released, the GUI resets, and the Rotate Data button must be pressed again to do another rotation.

c. To rotate the foot 180 degrees, press the **Change Foot Orientation** button. This will move the first point of the gaitline to the origin and rotate the pattern 180 degrees (Figure C.13).

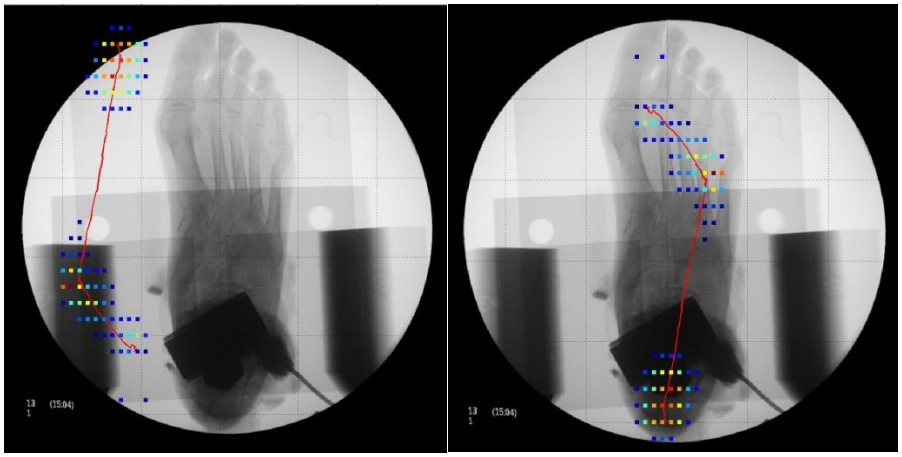

Figure C.13: Example of the functionality of the *Change Foot Orientation* button.

d. The size of the fluoroscope image can be changed, but should not be manipulated if a scale bar is used. If a scale bar is not available and the image size must be manually scaled, click the **Scale Image** button. Two red dots will appear in the image. Click on one or the other of these dots, and drag them horizontally to scale the image. When the mouse is released, the GUI resets and the Scale Image button must be pressed again to change the size of the image again.

e. These actions can be done in any order, and must be repeated until the position of the pliance data is sufficiently lined up with the fluoroscope image.

f. The pliance data visibility can be toggled on and off with the **Hide Pliance Data** button (Figure C.14).

g. The peak pressure region masks can be shown by pressing the **Show Masks** button. It is good practice to check that the masks are correctly implemented on the first few trials of each specimen (Figure C.15).

h.

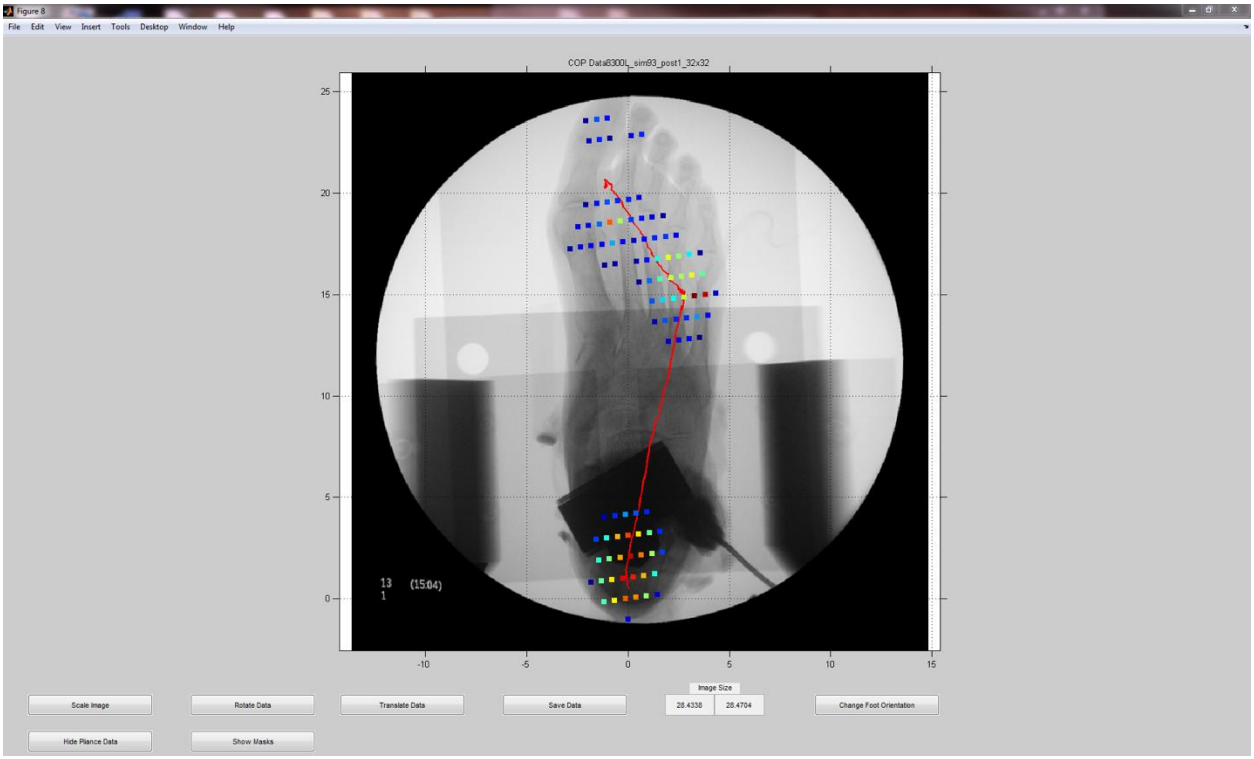

Figure C.14: An adequate registration of 25% bodyweight pliance data with the fluoroscope image.

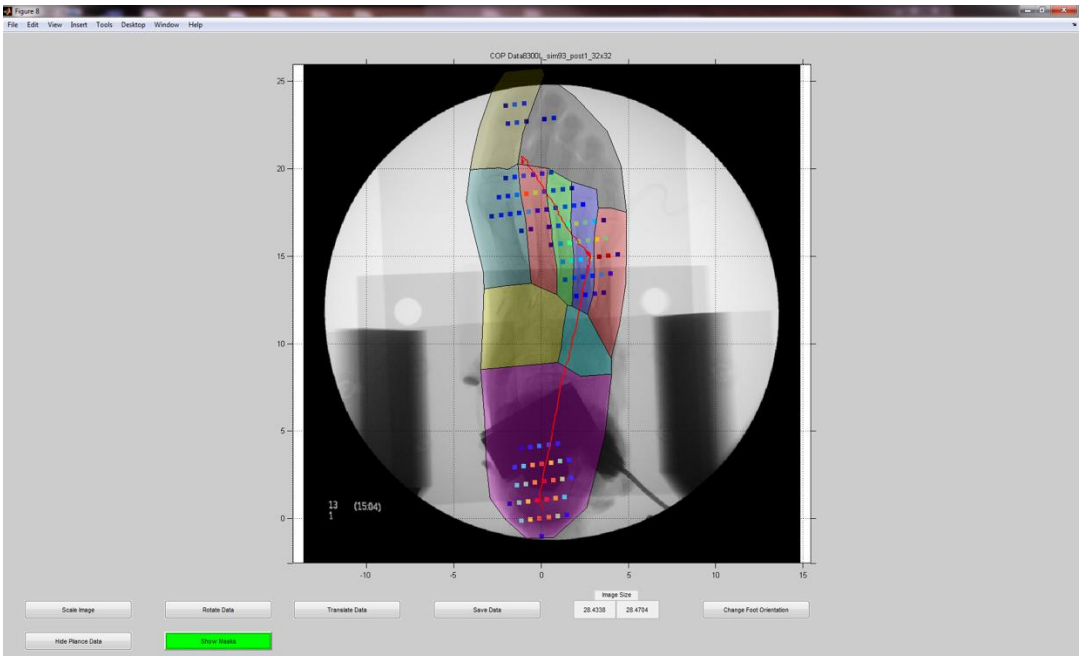

Figure C.15: The registered pliance data with the ten regions visible.

i. Once the data are aligned with the image satisfactorily, click the **Save Data Button**. This will write several text files into the same directory as the Matlab file, with each named based on the input .asc file name:

    i. *All_max_pressure_coordinates_9999L_sim11.txt*: the final position of the max pressure data after the registration is complete. This includes the final x- and y-coordinates of the point, and the pressure value at that point. These parameters will not be used for any statistical analysis, but does allow for the registration to be re-created if desired.

    ii. *COP_data_9999L_sim11*.txt*:* the x- and y-coordinates of the COP at 25%, 50%, 75%, and 90% stance phase, the old parameters analyzed for COP stats.

    iii. *Image_specs_9999L.txt*: changes made to the image for registration, include the size (x and y), and the inputs for *line_input* and

line_input_trans. This will allow for the image to be reproduced in a subsequent code where multiple trials of COP can be plotted on the same image. This file will be re-written each trial, but if the program is used correctly the parameters should not change.

iv. *Peak_Pressure_9999L_sim11.txt*: contains the peak pressure in each of the ten mask regions.

v. *Rotated_Gaitline_9999L_sim11.txt*: contains the x- and y-coordinates of COP at each measurement during the trial. (Note: no header on this output, but the data is listed x,y).

j. Once the data are saved, close the GUI, and return to the main matlab code.

8. After the first trial is processed, the image parameters are saved and kept constant for all remaining trials for the specimen. To keep these parameters constant, change the variable *run_number* = 0. The code will replot all the figures, but will skip right to the pliance registration GUI (Step 7). The pliance data must be manipulated again to overlay the max pressure pattern on the fluoroscope image. Again, once the pliance data is matched up, press Save Data. This process is then repeated for the rest of the trials for this specimen. Once the specimen is complete, steps 1-6 must be performed again for the first trial of subsequent specimens.

APPENDIX D: Ankle Arthroplasty Surgical Procedure for Misalignment Fixture

This procedure was developed with the assistance and clinical expertise of Dr. Cam Patthanacharoenphon and Dr. Bruce Sangeorzan.

D.1 Introduction

The following guide outlines the surgical procedure developed to perform surgery with the Salto Talaris total ankle replacement system using a custom misalignment fixture system. A precise amount of bone is removed from the tibia and talus to allow for the ankle replacement to be implanted into the specimen in a way that imitates the standard surgical protocol, but also allows for precise misalignment of the components after initial implantation. This protocol was used to evaluate misalignments of transverse plane rotation, anteroposterior translation, and coronal plane rotation.

D.2: Surgical Technique

1. An anterior incision is made between the tibialis anterior and extensor digitorum longus tendons (Figure D.1), in similar fashion to the standard Salto Talaris surgery. Two additional incisions are to be made on the posterior side, and the Achilles tendon is reflected at all points on the specimen above the level of the trigonal process on the talus. The soft tissue is removed on the posterior side and such that the posterior joint capsule is accessible.

Figure D.1: Anterior (right) and posterior (middle) incisions, and the Achilles tendon reflected (left).

2. A 9.6 or 11.1 mm aluminum rod (depending on specimen tibia size) is placed into the tibia. A pin is placed in the rod to serve as the pin normally in the tibial tuberosity. A second pin is placed in the distal tibia on the medial side, to anchor the alignment guide distally. This pin should be placed more proximal than the standard surgery, to allow for the larger tibial resection. The alignment guide is placed on the pins, and aligned parallel to the tibia (Figure D.2). During the initial installation, the mediolateral position, varus/valgus, and alignment to the tibia should be attempted to be placed in line with the correct anatomical structures, but the guide will be checked and re-aligned using fluoroscopy.

Figure D.2: The alignment guide attached to the specimen, with the proximal ("tibial tuberosity") and distal tibia pins.

3. Using fluoroscopy, the long axis of the alignment guide should be parallel to the tibia the sagittal plane and the coronal plane (Figure D.3, D.4). The mediolateral position of the cutting guide can be determined using fluoroscope images taken down the holes of the cutting guide. Once these alignment positions are determined, it is important to ensure all screws on the alignment guide are tight.

Figure D.3: The long axis of the alignment guide parallel to the long axis of the tibia in the sagittal plane.

Figure D.4: The cutting plane of the alignment guide aligned with the tibial plafond in the coronal plane.

4. The superoinferior level of the cutting guide, and subsequent determination of the resection cutting planes, is found by placing pins in the middle slot of the custom cutting guide. The bottom of the pins is aligned with the middle of the joint space just above the talar dome (Figure D.5). The cutting guide/fixture was designed such that once the cuts are made and the implant fixture is implanted, the apex of the talar dome of the implant will be at the level of the bottom edge of these pins, thus this edge is aligned with the middle of the native tibiotalar joint space. Once the proper alignment is achieved, all screws on the alignment guide should be tightened.

Figure D.5: Aligning the cutting guide: matching up the bottom of the pins in the middle holes with joint space above the apex of the talar dome.

5. After correct superoinferior alignment is achieved additional fluoroscope images should be taken to ensure the mediolateral alignment is still optimal (Figure D.6). After this is confirmed, the holes on the medial and lateral sides of the cutting guide are drilled out (Figure D.7). This will create the medial and lateral borders of the tibial resection, and the top holes will serve as pilot holes for the pins securing the cutting guide to the tibia. The pins are then placed in the tibia (Figure D.8).

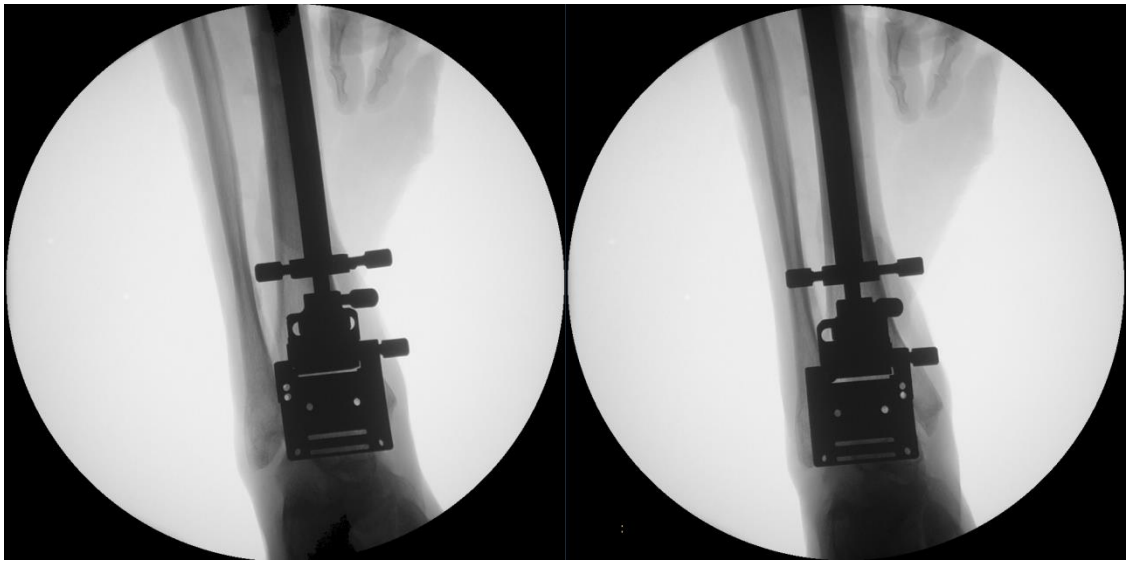

Figure D.6: Determining the mediolateral position using fluoroscope images down the lateral holes (left) and medial holes (right) of the cutting guide.

Figure D.7: Drilling holes through cutting guide, to set medial and lateral borders of tibial resection, (the talar pins are not inserted at this time, in this image, they are only in the cutting guide to observe alignment).

Figure D.8: Pins connecting cutting guide to tibia.

6. After the pins are placed in the tibia, the foot should be moved such that the tibiotalar joint is in neutral position (plantagrade). After a satisfactory neutral position of the tibiotalar joint is found, pins are placed into the talus using the bottom holes of the cutting guide (Figure D.9). Pilot holes can be used to start the pins, but going without pilot holes proved to be more efficient and just as effective. The talar pin holes in the cutting guide are designed to align the pins just below the talar cutting plane.

Figure D.9: The cutting guide secured with two pins in the distal tibia and two pins in the inferior talus. The talus pins are aligned obliquely such that the saw blade will pass over them (in this image the tibia cut is already complete, and the lateral talar pin deflected more superior than it was supposed to).

7. Following the placement of the pins in the talus, the cutting guide is securely connected to the talus and tibia. The Microaire sagittal saw is then used to cut the tibia and talus, with cuts in the tibial cut slot, proximal talus slot, and distal talus slot (Figure D.10). The rationale for the three cutting planes is shown below (Figure D.11), demonstrating how the cutting planes interface with the design. The posterior incisions and reflected Achilles tendon will allow for easier removal of the posterior bone from the posterior joint capsule.

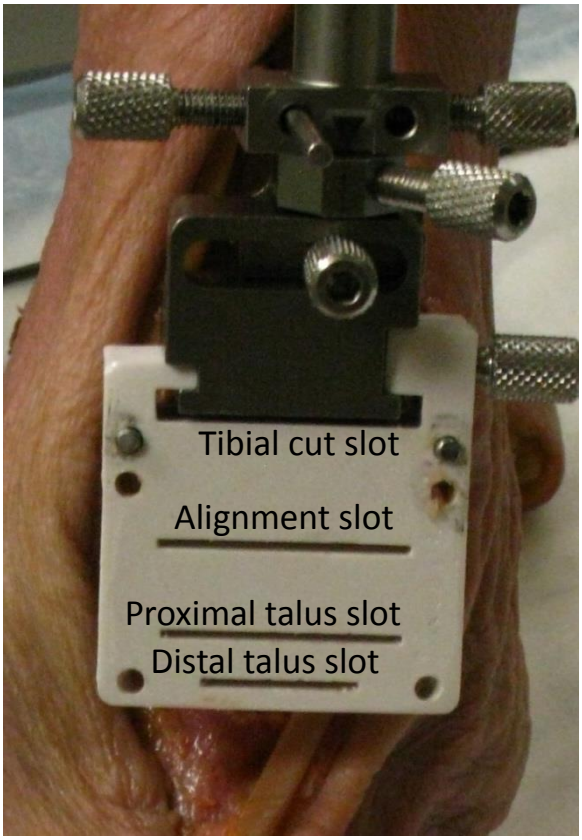

Figure D.10: The cutting guide with slots identified (Note: this image is with a 3D printed cutting guide, which was later machined in stainless steel).

8. The tibial cut slot (top) creates the cutting plane for the tibial resection. The alignment slot is used to determine the initial superoinferior alignment of the cutting guide, but is not cut through. The proximal talus slot is wider, and allows for the rotation of the talar component relative to the bone during misalignment. The distal talus slot is more narrow, and allows for less talus to be removed from this plane, as the distal rotation plate in the misalignment assembly is more narrow than the rest of the talar component.

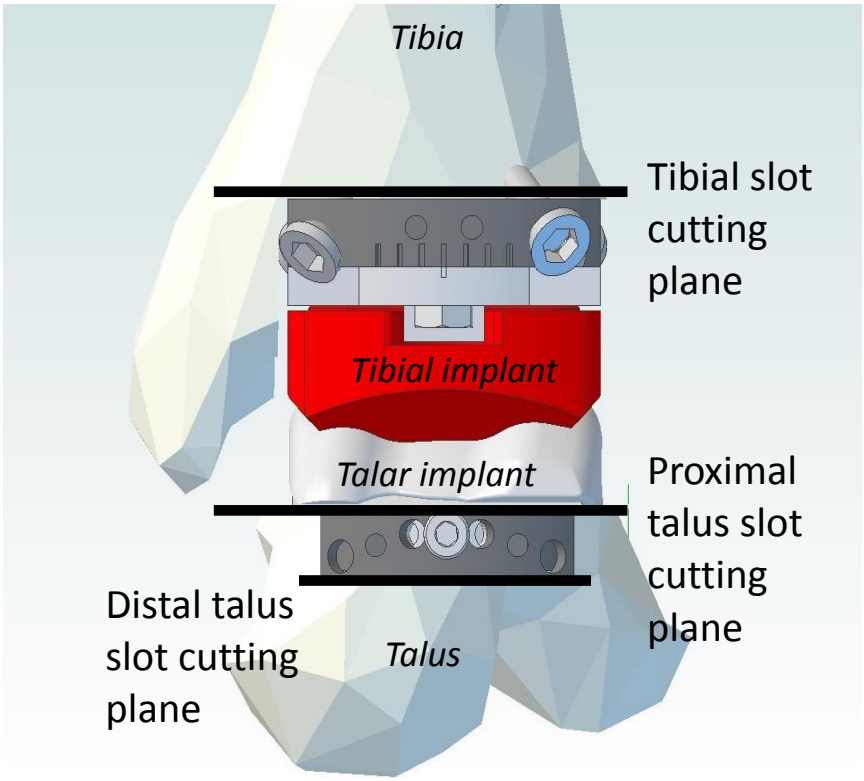

Figure D.11: CAD image showing how the cutting planes interface with the implant assembly.

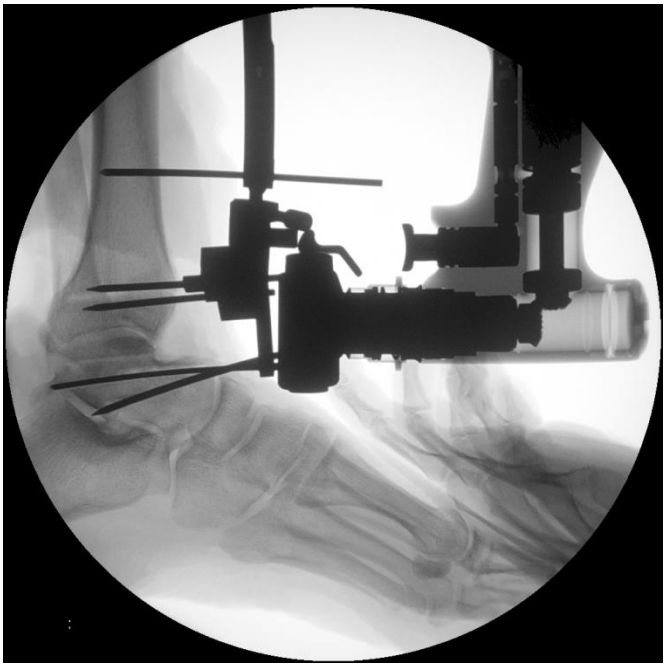

Figure D.12: After the three cuts are made, with the saw blade in the most inferior cut.

Figure D.13: Anterior view of the three cutting planes, before the bone is removed.

9. Removal of both the tibial and talar resection is aided by the posterior access to the ankle joint, however it remains a challenging part of the surgery. On the tibial side (Figure D.14-D.16), the drill holes set the mediolateral resection width. Using a combination of the small sagittal saw (*Stryker TPS*) and a narrow osteotome, allows for the borders of the resection to be started. Cutting through the middle of the tibial resection allows for the bone to be removed piece by piece. Using the posterior access to the joint, the bone can be hammered out using a punch through the anterior incision (the way the resection is tapered makes removal through the posterior side of the joint more difficult. The bone to be resected must be completely separated from the rest of the tibia, particularly on the medial side, as the medial malleolus can be broken by accident if the resection is not completely separated.

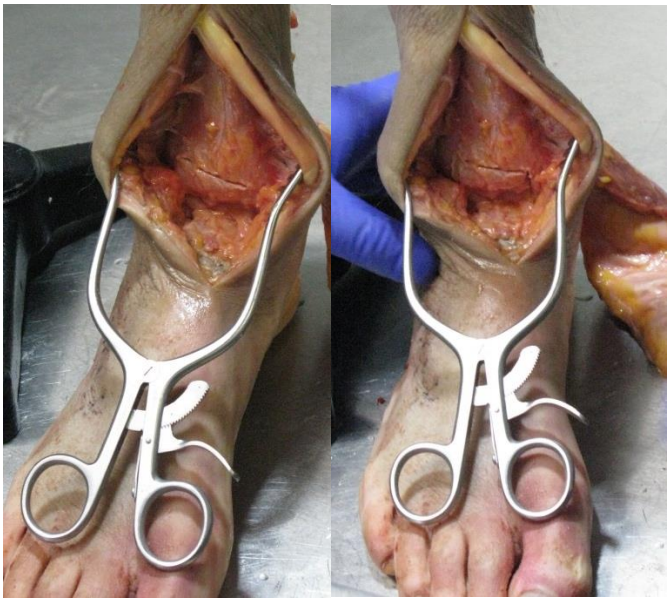

Figure D.14: The tibia after the main cut is made (right) and after the medial and lateral sides of the resection are started to be expanded with an osteotome.

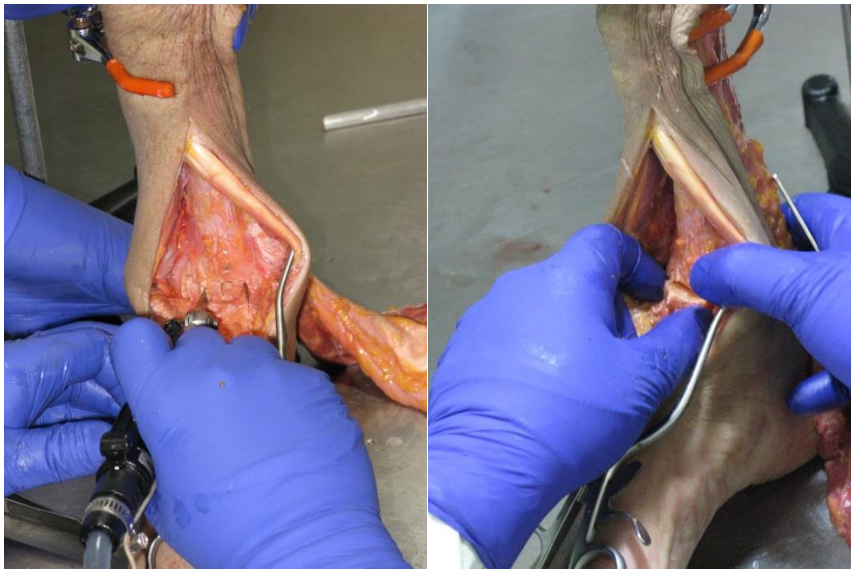

Figure D.15: Cutting the tibial resection to remove the bone in parts (right), and removal of the tibial resection from the anterior side.

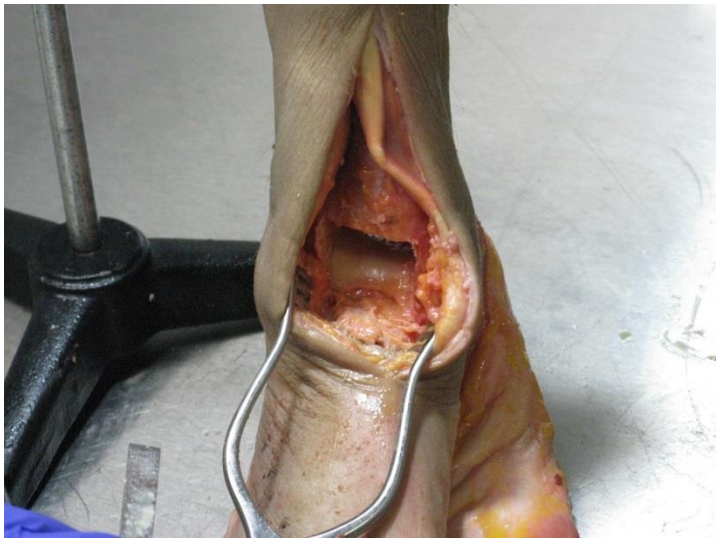

Figure D.16**:** A specimen after the tibial resection is complete.

10. Removal of the talar bone is even more challenging (Figure D.17-20). The most successful method we found was placing a thin osteotome through the cutting plane, to shield the mediolateral cuts from damaging bone below the plane of the cut.

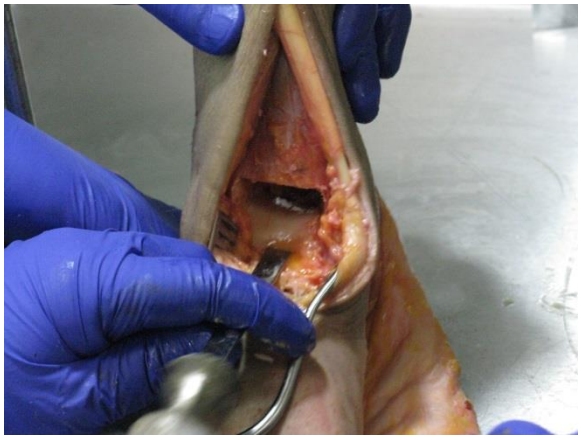

Figure D.17: Using an osteotome through the talar cut to shield the bone inferior to the cutting plane. An osteotome or the small sagittal saw can be used to cut above this osteotome to start the resection.

Figure D.18: After the center portion of the talar cut is removed, the medial and lateral sides are removed by again placing the osteotome on the cutting plane and removing the bone above it.

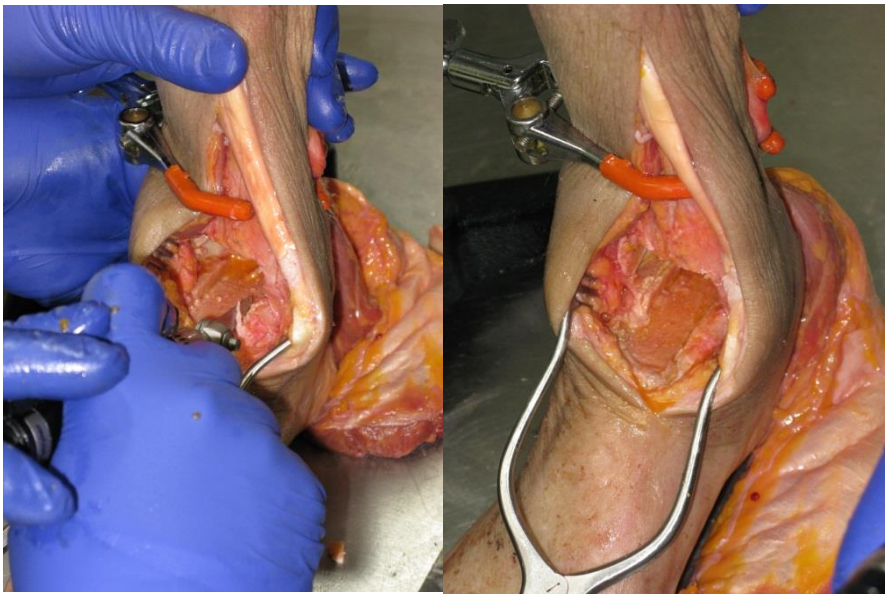

Figure D.19: The small sagittal saw can be used to expand the mediolateral width of the talar resection (right), and the talus after the central resection is complete.

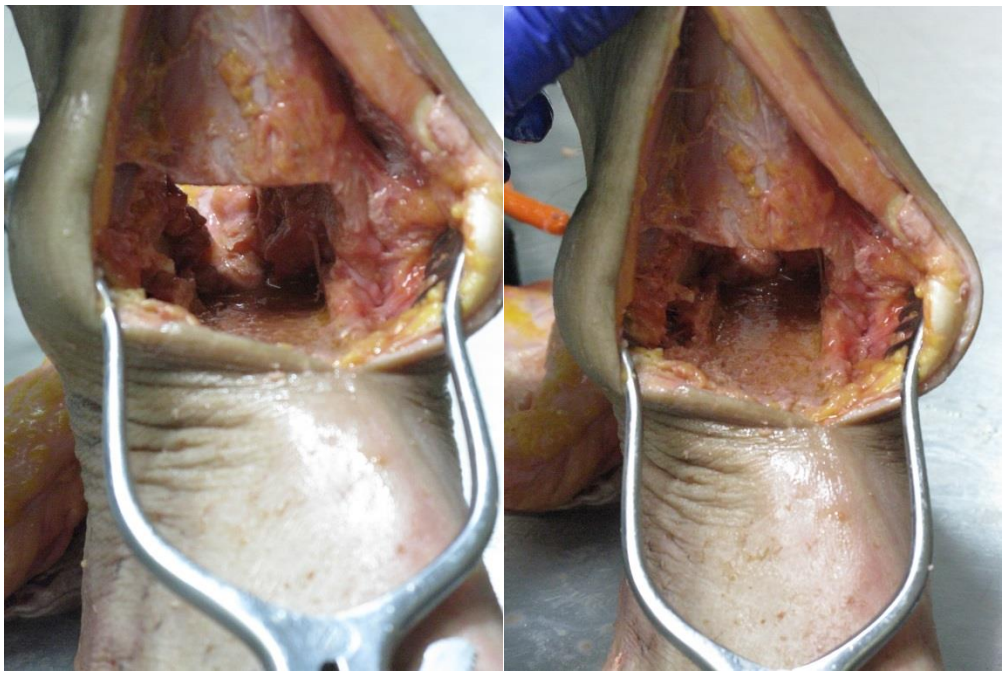

Figure D.20: The talus after all bone removal is complete. The recession/ledges on medial and lateral sides allows for the implant fixture to be bone cemented to the side of the talus, and reduces the chance of ligamentous damage on the medial and lateral sides of the talus.

Figure D.21: All bone removed from cuts. In this specimen all bone was removed from the talus such that only one plane remain.

Figure D.22: The implant and fixture assembly inserted into the specimen for alignment, but before fixation.

Section D.2: Implantation of ankle arthroplasty misalignment fixture.

The arthroplasty assembly is shown below (Figure D.23). The standard tibial component is not used in this design. Instead the trial tibial bearing was tapped and screwed into directly, and connected to the tibia rotation plate. The talar component is machined to remove the part of the post and lateral flange, and connected to the misalignment fixture using a shoulder bolt. Rotational misalignments are set by rotating the tibia rotation plate relative to the top tibia plate, and talar implant connetion relative to the distal talus plane.

The installation of the components is performed with the entire assembly inserted at once, with the angle between the implants fixed by the set initial position guide. This guide fixes the implant in a neutral position, as shown below.

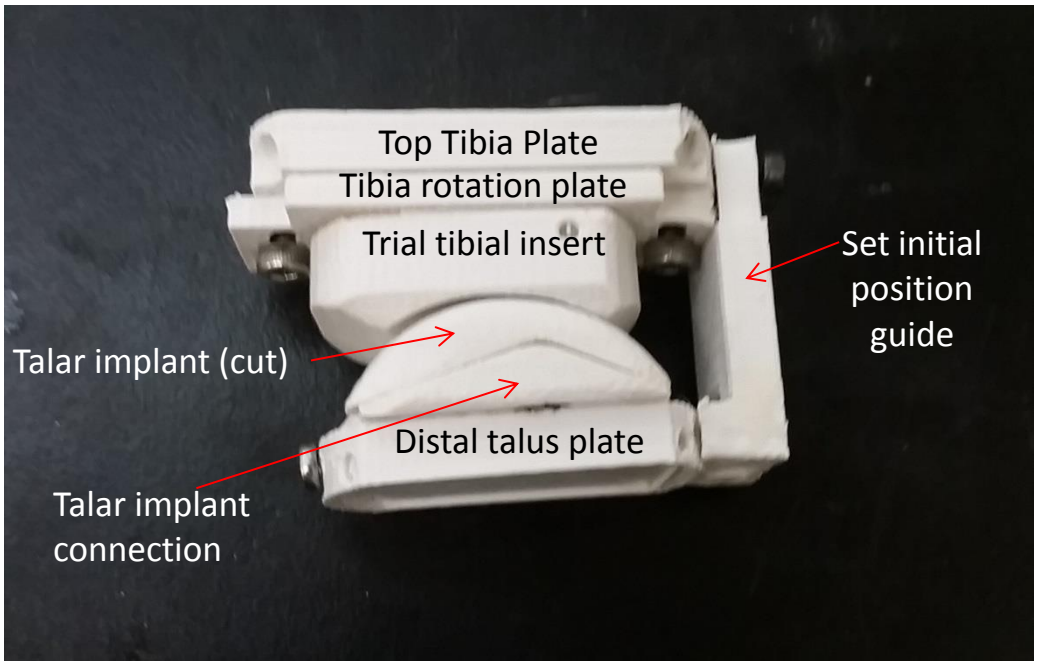

Figure D.23: The ABS plastic-3D printed prototype of the arthroplasty assembly.

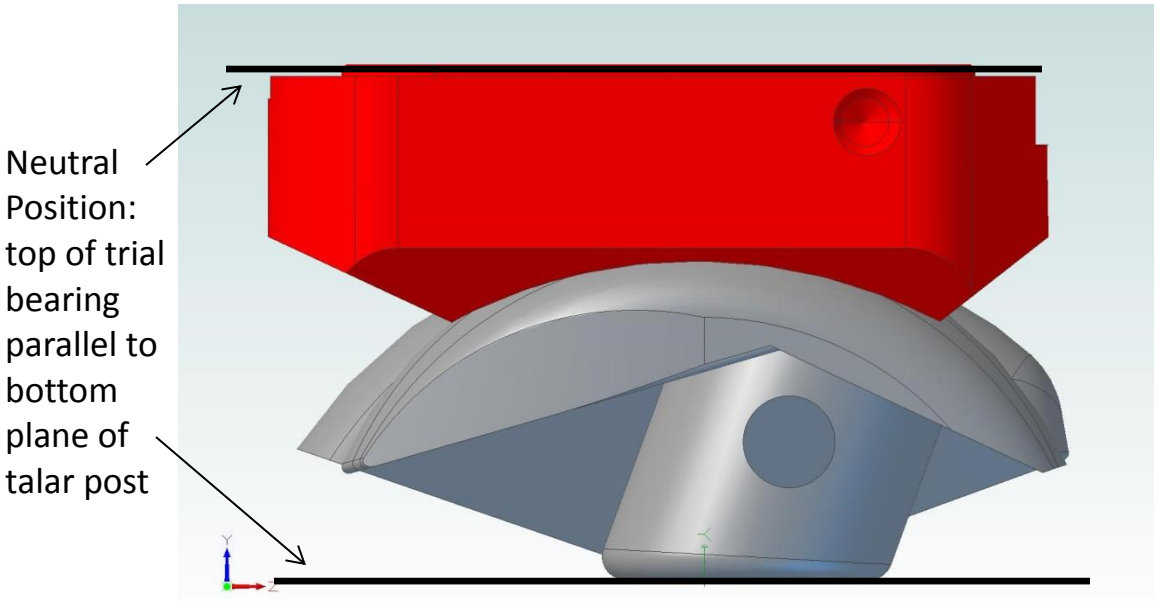

Figure D.24: Neutral position of implant

The correct initial anteroposterior, mediolateral and transverse plane rotational position of the implant assembly will be determined using fluoroscopy as described above. If the 10mm

tibial bearing seems too tight or loose in the joint, it can be swapped for the 9mm or 11mm tibial bearing. After the optimal position is determined, the distal talus plate is cemented to the talus by filling the cavity with bone cement (Figure D.25). Before finding the position, small holes are drilled in the talar cutting surface to aid in bone cement fixation (Figure D.26).The best ratio to create optimal viscosity of the bone cement mixture to fill the cavity is 25mL powder/15mL liquid. During fixation a weight is placed on the top of the tibia, to ensure the surface of the talar plate fixture is compressed against the bone. Once the bone cement is completely set (20-30 minutes), the top tibia plate is secured to the tibia bone using four obliquely directed 3.5mm bone screws (Figure D.27). The set initial position guide is then removed. All misalignments should be achieved first on the bench-top, and additional bone is removed after the fixture is implanted, if necessary.

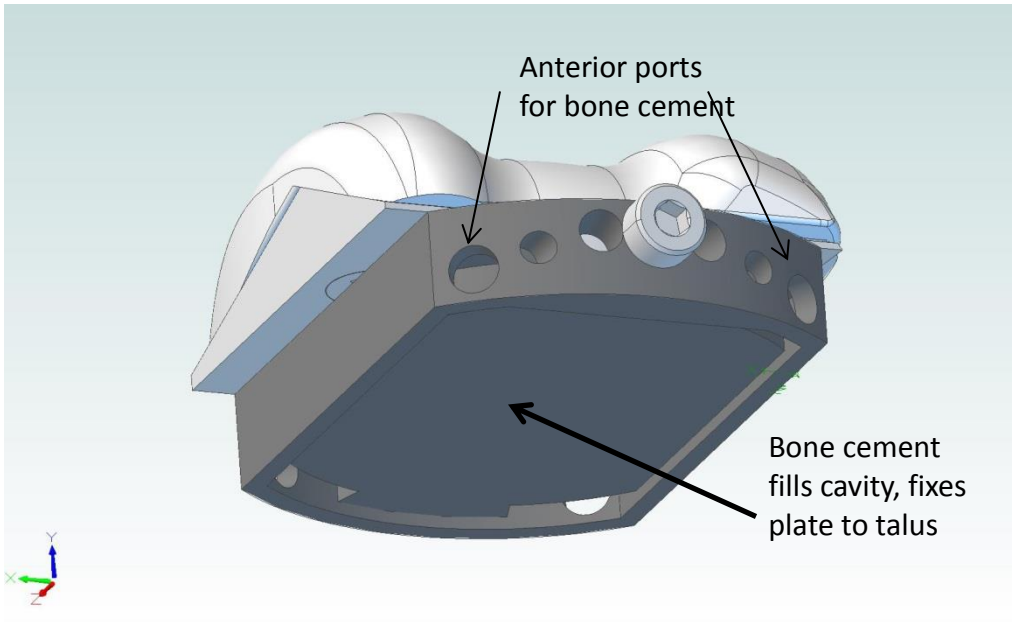

Figure D.25: Distal talus plate showing cavity for bone cement fixation.

Figure D.26: Holes drilled in talar cutting plane to allow improved bone cement fixation.

Figure D.27: Placement of the arthroplasty assembly. The apex of the talar bone is directly superior to the lateral process of the talus.